Conserved basal lamina proteins, laminin and nidogen, are repurposed to organize mechanosensory complexes responsible for touch sensation.

Alakananda Das[1,†], Joy A. Franco[2,†], Ben Mulcahy[4], Lingxin Wang[1,†], Dail Chapman[1,†], Chandni Jaisinghani[1], Beth L. Pruitt[3], Mei Zhen[4], Miriam B. Goodman[1*]

[1] Department of Molecular and Cellular Physiology, Stanford University, Stanford, CA 94305
[2] Department of Mechanical Engineering, Stanford University, Stanford, CA 94305
[3] Departments of Mechanical Engineering and Molecular, Cellular, & Developmental Biology, University of California Santa Barbara, Santa Barbara, CA 93106
[4] Lunenfeld-Tanenbaum Research Institute, Mount Sinai Hospital, Toronto, Ontario M5G 1X5, Canada
*Correspondence: mbgoodmn@stanford.edu

†Current addresses

Alakananda Das, Division of Biology and Biological Engineering, California Institute of Technology, Pasadena, CA, 91125
Joy A. Franco, Department of Neurobiology, Harvard Medical School, Boston, MA 02115
Dail Chapman, Department of Biology, Georgetown University, Washington, DC 20057
Lingxin Wang, Novel Human Genetics Research Unit, GSK, Collegeville, PA 19426

Summary

The sense of touch is conferred by the conjoint function of somatosensory neurons and skin cells. These cells meet across a gap filled by a basal lamina, an ancient structure found in metazoans. Using *Caenorhabditis elegans*, we show that membrane-matrix complexes containing laminin, nidogen, and the MEC-4 mechano-electrical transduction channel reside at this interface and are instrumental for proper touch sensation. These complexes fail to coalesce in touch-insensitive extracellular matrix mutants and in dissociated neurons. MEC-4, but not laminin or nidogen, is destabilized by point mutations in the C-terminal Kunitz domain of the extracellular matrix component, MEC-1. Thus, neuron-epithelial cell interfaces are instrumental in mechanosensory complex assembly and function. Loss of nidogen reduces the density of mechanoreceptor complexes and the amplitude of the touch-evoked currents they carry. These findings imply that somatosensory neurons secrete proteins that actively repurpose the basal lamina to generate special-purpose mechanosensory complexes responsible for vibrotactile sensing.

Keywords

Basal lamina; neuron; mechanoelectrical transduction channels; force-gated ion channels; mechanosensation; touch; somatosensation; extracellular matrix

Introduction

Touch is our most intimate sense. It is initiated by mechanical deformation of the skin generated by direct application of static force or mechanical vibration. Among other adaptive behaviors, vibrotactile sensation enables animal communication, mate-finding, and mating (Hill, 2008). Additionally, touch sensation is instrumental for the cognitive and emotional development of humans and other primates (Cascio et al., 2019). In most animals, vibrotactile sensing is made possible by somatosensory neurons that innervate and integrate into the animal's skin and these neurons all use mechanosensitive ion channels to convert physical deformation into electrical signals. This process of mechanotransduction is thought to occur via two, non-exclusive, biophysical mechanisms. Channels sensitive to membrane tension are thought to operate via a force-from-lipid mechanism in which sensory stimuli increase membrane tension. Other channels are proposed to operate via a force-from-filament mechanism in which physical deformation is conveyed to channels via extracellular or intracellular filaments (Goodman et al., 2023; Katta et al., 2015; Kung, 2005). Channels that use one or both mechanisms have been linked to somatosensation in vertebrates and invertebrates and osmotic sensing in microbes and plants (reviewed in Goodman et al., 2023).

Many vibrotactile sensory neurons are closely associated with epidermal cells or to specialized, epidermal-derived sensory cells, while some appear to weave paths among cells in the epidermis (Han et al., 2012; Jiang et al., 2019; Kim et al., 2012; O'Brien et al., 2012; Talagas et al., 2020; Yin et al., 2021). This association seems to emerge over time. For instance, in newly hatched *Caenorhabditis elegans* larvae, the lateral touch receptor neurons run alongside body wall muscles and these neurons become engulfed by epidermal cells during development. In adult *C. elegans* nematodes, these sensory neurons are displaced laterally such that their long, unbranched sensory neurites are positioned near the lateral midline in adults (Chalfie, 1993; Chalfie and Sulston, 1981). Lining the epidermis is a basement membrane or basal lamina (BL), a ubiquitous and conserved extracellular matrix (ECM) that surrounds tissues in all metazoans (Aumailley, 2021). Whereas the instructive role that the BL microenvironment plays in patterning somatosensory neurons within the skin is well-characterized (Yin et al., 2021), its contribution to the molecular events responsible for touch sensation remains to be fully elucidated.

Basal laminae are thin (ca. 100 nm) continuous sheets that surround several mammalian tissues (Jayadev and Sherwood, 2017; Laurie et al., 1982; Pozzi et al., 2017; Ruben and Yurchenco, 1994; Stern, 1965; Susi et al., 1967; Vracko and Strandness, 1967; Vracko, 1972, 1974; Vracko and Benditt, 1970, 1972; Younes et al., 1965). These structures are evolutionarily ancient and contain a core set of proteins conserved in all metazoans: laminin, collagen type IV, nidogen, and heparan sulfate proteoglycans or HSPS (Hynes, 2012). Laminin is a heterotrimeric protein composed of laminin-α, laminin-β, and laminin-γ subunits that typically self-assemble into continuous sheets anchored to the cell surface by a triple helical coiled-coil stalk and globular domains that bind membrane protein receptors (Cheng et al., 1997; Yurchenco and O'Rear, 1994a, 1994b; Yurchenco and Schittny, 1990; Yurchenco et al., 1986, 2002). Nidogen cross-links laminin, collagen, and the heparan sulfate proteoglycan, perlecan, in BL and other ECMs (Aumailley et al., 1993). Humans and other mammals have at least 16 distinct laminin heterotrimers (Aumailley, 2013). Conservation among vertebrate laminin isoforms and antibody cross-reactivity complicates efforts to determine which isoforms are present in specific tissues, including the skin and peripheral nervous system (Domogatskaya et al., 2012). *C. elegans*, by contrast, has only two laminin isoforms with distinct tissue localization and functions in organogenesis (Huang et al., 2003). They contain one of two laminin-α proteins (EPI-1or LAM-3), a single laminin-β (LAM-1) protein, and a single laminin-γ (LAM-2). Although the laminins associate with the nerve ring and ventral nerve cord as well as BL surrounding other tissues, genes encoding laminins are expressed primarily outside the nervous system (Huang et al., 2003). *C. elegans* also expresses conserved laminin-binding proteins such as nidogen (NID-1), perlecan (UNC-52), syndecan (SDN-1), dystroglycan (DGN-1), and fibulin (FBL-1) (Keeley et al., 2020). These BL proteins also contribute to the organization of presynaptic structures across animal taxa [reviewed in (Sanes and Lichtman, 1999)], but their role in somatosensory function is not understood.

Genetic approaches in *C. elegans* have identified more than a dozen proteins and six touch receptor neurons (TRNs) specifically required for touch sensation (Chalfie and Au, 1989; Chalfie and Sulston, 1981). Touch evokes similar calcium transients in all six TRNs (Chatzigeorgiou et al., 2010; Nekimken et al., 2020; Suzuki et al., 2003), indicating that they all function as mechanosensory neurons. Proteins required for touch sensation include MEC-4, which is an essential pore-forming subunit of the mechano-electrical transduction (MeT) channel

82 (O'Hagan et al., 2005), two tubulins, MEC-7 and MEC-12, and three ECM proteins, MEC-5,
83 MEC-1, and MEC-9 (Du et al., 1996; Emtage et al., 2004). The MEC-4 channels are organized
84 in a characteristic speckled or punctate distribution along the TRN neurites (Árnadóttir et al.,
85 2011; Chelur et al., 2002; Chen and Chalfie, 2015; Cueva et al., 2007; Emtage et al., 2004; Katta
86 et al., 2019; Petzold et al., 2013; Vásquez et al., 2014). The tubulins are required to form a
87 distinctive bundle of large-diameter microtubules and for proper behavioral responses to touch
88 (Savage et al., 1989) and to maintain proper expression of MEC-4 and several other *mec-3*-
89 dependent genes (Bounoutas et al., 2011). Although loss of MEC-7 or MEC-12 reduces the size
90 of touch-evoked currents, neither tubulin is required to activate MeT channels *in vivo* (Bounoutas
91 et al., 2011; O'Hagan et al., 2005). Loss of MEC-5, MEC-1, or MEC-9 disrupts the appearance
92 of MEC-4::YFP puncta (Emtage et al., 2004). MeT channel spacing is thought to regulate the
93 amplitude of touch-evoked currents carried by MEC-4-dependent channels, as stronger stimuli
94 recruit channels further away from the point of stimulus application (Katta et al., 2019). Many
95 other proteins affect mechanosensation either directly by contributing to force transfer from the
96 skin to the channels, or indirectly by modulating morphology, protein trafficking, and channel
97 positioning.

98 Since behavioral screening methods for assessing touch sensitivity in worms require
99 healthy, mobile animals (usually adults), mutations that are lethal or cause severe morphological
100 defects cannot be reliably tested for defects in touch sensation. Basal lamina genes and much of
101 the matrisome (Hynes and Naba, 2012) fall into this category. Behavioral screening methods
102 overlook mutations that have significant effects on the structure and organization of the ECM
103 and MeT channels and modest effects on touch response behavior. Here, we leverage new
104 molecular tools for visualizing the well-characterized MEC-4 channel (Katta et al., 2019) and BL
105 proteins (Keeley et al., 2020) to investigate the molecular basis of channel positioning in
106 vibrotactile sensory neurons. Our approach combines genetic dissection with static and dynamic
107 imaging in living animals and cultured sensory neurons, fluorescence recovery after
108 photobleaching (FRAP), and *in vivo* electrophysiology. We show that the MEC-4 channel
109 organizes into discrete stationary and stable clusters that co-localize with similarly stable and
110 discrete BL puncta containing laminin and nidogen. Loss of nidogen reduces laminin and MEC-4
111 puncta density as well as mechanoreceptor current amplitude, confirming that nidogen
112 contributes both the organization and function of channel-ECM complexes *in vivo*. Three ECM

113 genes previously linked to touch sensation, *mec-5*, *mec-1*, and *mec-9*, are required for the proper
114 organization of both the keystone MEC-4 ion channel (Du et al., 1996; Emtage et al., 2004), and
115 the nidogen and laminin-containing BL anchor (this study). The large MEC-1 protein, which is
116 expressed and secreted by the TRNs, is seen to play an additional role: its C-terminal Kunitz
117 domain being required to integrate MEC-4 channels into the membrane-ECM spanning
118 mechanosensory complex. We propose that somatosensory neurons actively repurpose conserved
119 BL proteins to form a mechanosensory complex that bridges the neuronal plasma membrane to
120 the extracellular matrix and is instrumental in converting touch-induced longitudinal strain into
121 electrical signals.

122

123 **Results**

124 The TRNs extend long (~0.5mm), thin (~200 nm diameter) sensory neurites that lie close
125 to the surface of the body ensuring optimal sensitivity to indentations and are embedded within
126 the epidermis (Figure 1A-B). A specialized extracellular matrix or 'mantle' (Chalfie and Sulston,
127 1981) fills the volume between the TRN plasma membranes and the basal membrane of the
128 epidermis (Figure 1B), and contains proteins secreted by both the TRN and the surrounding
129 epidermal cell. Based on overexpression of transgenes expressing fluorescent protein fusions or
130 antibody staining, prior work has identified the collagen, MEC-5, and two Kunitz domain
131 containing proteins, MEC-1 and MEC-9, as constituents of the ECM along TRNs (Cueva et al.,
132 2007; Du et al., 1996; Emtage et al., 2004). MEC-1::GFP and MEC-5::CFP generated both
133 periodic puncta and uniform fluorescence along the lateral TRNs and were proposed to co-
134 localize based on image superposition. Although Emtage, et al (Emtage et al., 2004) reported that
135 fluorescent protein-tagged MEC-1 and MEC-5 puncta co-localize with MEC-4 puncta , a later
136 study using antibodies against MEC-4 and MEC-5 showed that MEC-5 does not co-localize with
137 MEC-4 and has shorter inter-punctum intervals on average compared to MEC-4 (Cueva et al.,
138 2007).

139 Recent advances in genome editing using CRISPR/Cas9 enable engineering endogenous
140 genetic loci in *C. elegans* to encode fusions between the encoded protein and bright, stable
141 fluorescent proteins such as mNeonGreen (mNG) and wormScarlet (wSc) (Heppert et al., 2016;

142 Hostettler et al., 2017; El Mouridi et al., 2017). This approach minimizes disruption to genetic
143 regulatory elements compared to overexpression of transgenes and maximizes the ability to
144 determine the subcellular localization of the tagged proteins and to analyze their *in vivo*
145 dynamics compared to antibody staining. Building on a suite of transgenic *C. elegans* strains
146 expressing mNG fusions of the *C. elegans* matrisome (Keeley et al., 2020), we built a set of
147 dual-color transgenic strains that enabled us to visualize the BL structures at the interface
148 between the TRNs and the ensheathing epithelial cells and their alignment with MeT channels *in*
149 *vivo* and in dissociated, cultured neurons.

150

151 **ECM proteins laminin and nidogen are present in a punctate distribution along TRNs**

152 To better understand the extracellular matrix proteins affecting touch sensation and
153 influencing the distribution of MEC-4 channels along TRNs, we performed a visual screen to
154 identify ECM proteins that localize to TRN neurites. We analyzed 35 *C. elegans* strains
155 expressing fluorescent protein-labeled matrisome proteins under endogenous *cis* regulatory
156 control at their native locus (34 strains) or within a synthetic, single copy locus (1 strain), for
157 their localization along the TRNs. These transgenic alleles represent 27 conserved BL proteins
158 and their putative membrane receptors (Table S1). We focused this analysis on the ALM neurons
159 in adult worms for two main reasons: 1) no other neurons are nearby and 2) the ALM cell bodies
160 and axons are separated from the body wall muscles and gonad, two large tissues known to
161 express core basement membrane proteins. We found 11 proteins along the ALM neurites either
162 in a uniform or punctate distribution (Figure 1C-D). Nine appeared to be uniformly distributed
163 along ALM: SAX-7 L1CAM, LET-805 myotactin, MIG-6 papillin, PAT-2 α-integrin, SDN-1
164 syndecan, HIM-4 hemicentin, UNC-52 perlecan, FBL-1 fibulin, and EPI-1 laminin-α (Figure
165 1C). These observations identify three new constituents of the mechanosensory ECM (MIG-6
166 papillin, UNC-52 perlecan, and EPI-1 laminin-α) and reinforce prior work showing that
167 overexpressed fusions of GFP to HIM-4 hemicentin (Vogel and Hedgecock, 2001), FBL-1
168 fibulin (Muriel et al., 2005), SDN-1 syndecan (Rhiner et al., 2005), SAX-7 L1-CAM (Díaz-
169 Balzac et al., 2016) and endogenously-tagged LET-805 myotactin (Coakley et al., 2020)
170 associate with the TRNs. With the exception of mNG::FBL-1, the introduction of the fluorescent
171 protein encoding sequence at the endogenous locus did not significantly affect touch response

behavior (Table S2). Thus, many conserved ECM proteins decorate the TRNs, suggesting that proper touch sensation depends on conserved molecular constituents of the ECM skin-neuron interface.

Two ancient and core basal lamina proteins localized to puncta distributed along TRNs: LAM-2 laminin-γ and NID-1 nidogen (Figure 1D). Given that nidogen is a laminin-binding protein (Dziadek and Timpl, 1985), the present findings are consistent with the presence of nidogen-like immunoreactivity along the ventral TRNs (Ackley et al., 2005). Notably, discrete laminin and nidogen puncta were not associated with other tissues such as the pharynx and gonad, where these proteins appear to uniformly coat tissues in continuous sheets (Clay and Sherwood, 2015; Kramer, 2005), or the in the body wall muscles in which they appear as stripes (Huang et al., 2003; Keeley et al., 2020). The TRNs have long been known to associate with a diffuse, electron-dense ECM in transmission electron micrographs (TEM) in chemically-fixed samples (Chalfie and Sulston, 1981). However, samples prepared by high-pressure freezing by us and others reveal more fine structure in the ECM. Specifically, these images contain electron-dense structures that appear as a dashed line close to the TRN plasma membrane and localize to the apical side of the TRN close to the cuticle (Frédéric et al., 2013: Figure 5A right; Hsu et al., 2014: Figure 3A; Richardson et al., 2014: figure 5J; Topalidou et al., 2012: figure 3A second from left).

To learn more about these nanoscale structures, we reconstructed them from serial-section new and published (Krieg et al., 2017) TEM data sets and found that these features consisted of arrays of beam-like structures running for nearly 1 µm parallel to the TRN plasma membrane (Figure 1E, left). On average, individual beams are approximately 20 nm wide, 8 nm thick, and separated by 8 nm and are organized in lateral arrays of 10-15 beams. They are closer to the TRN plasma membrane than they are to the epidermal cell's basal membrane. To determine whether these structures run continuously along the length of the TRN neurite, we analyzed long serial-section datasets and found that beams were continuous in several successive sections (red segments in Figure 1E right, Figure S1A-D, Movie S1) and then disappeared (yellow segments in Figure 1E right, Figure S1A-D, Movie S1) before reappearing again. We have observed this in datasets covering at least 10 µm along the length of the three anterior TRNs from a wild-type larva (L3) and at least 8 µm stretches in the posterior TRNs from another

202 adult wild-type animal. Notably, the ECM beams appear next to the ventral TRN, AVM, but not
203 other adjacent neurons engulfed within the same epidermal lumen (Figure S1E). Thus, the ECM
204 along TRNs is non-uniform along its longitudinal axis with discontinuous segments of electron
205 dense structures and is reminiscent of the arrangement of MEC-4 channels in puncta along the
206 ALM.

207

208 **Laminin, Nidogen, and MEC-4 co-localize to puncta that decorate TRNs**

209 Laminin is an obligate heterotrimeric protein composed of laminin-αβγ subunits, which
210 associate through the long coiled coil domains in each subunit. Since the laminin-αβγ subunits
211 assemble in a 1:1:1 stoichiometry, and LAM-2 laminin-γ was detected in a punctate distribution
212 along TRNs, we expected LAM-1 laminin-β as well as one or both laminin-α subunits, LAM-3
213 and EPI-1, to also localize in a similar pattern along TRNs. Homozygous LAM-1::wSc animals
214 were sterile and showed basal lamina defects, but heterozygous animals with one tagged and one
215 untagged copy of *lam-1* were healthy and showed punctate distribution of LAM-1::wSc along
216 the TRNs (Figure 2A). While we detected faint EPI-1::mNG fluorescence uniformly along the
217 ALM (Figure 1D), we did not detect any LAM-3::mNG fluorescence along the ALM. Another
218 recent study using the same endogenously tagged LAM-3::mNG expressing strain did not detect
219 a signal at the nerve ring (Keeley et al., 2020), although a previous study using an antibody
220 against LAM-3 detected a strong signal at the nerve ring (Huang et al., 2003). Thus, the apparent
221 lack of LAM-3::mNG signal along the TRNs could be due to low expression of the protein or an
222 artifact of the position of the tag on the protein.

223 The appearance of laminin-β, laminin-γ and nidogen along the TRNs shown here
224 (Figures 1C, 2A) is similar to that reported previously for MEC-4 (Árnadóttir et al., 2011; Chelur
225 et al., 2002; Chen and Chalfie, 2015; Cueva et al., 2007; Emtage et al., 2004; Katta et al., 2019;
226 Petzold et al., 2013; Vásquez et al., 2014). To quantify the degree of similarity, we measured
227 inter-punctum intervals (IPIs) for ALM-associated laminin and nidogen puncta and compared
228 their distributions to those found for mNG::MEC-4, expressed from the single-copy *pgSi116*
229 transgene (Katta et al., 2019). The distributions of all four proteins were comparable (Figure 2A-
230 B), even though MEC-4 has slightly shorter IPIs on average and the distribution of IPIs of

231 LAM-1, LAM-2, and NID-1 were more similar to one another than to mNG::MEC-4. All four
232 proteins showed smaller IPIs closer to the cell body and larger IPIs further away (Figure 2B).
233 Additionally, the puncta not significantly different in size — median length (μm): LAM-
234 1::wSc=1.29, LAM-2::mNG=1.2, NID-1::wSc=1.10 and mNG::MEC-4 1.11 (Figure S2A).
235 Notably, these dimensions mirror the average length of the ECM beam arrays observed in
236 ssTEM datasets (Figure 1E, Figure S1), suggesting that the protein puncta observed in living
237 animals could be related to electron-dense structures seen in fixed samples.

238 Given their disparate positions within the skin-nerve complex, the MEC-4 ion channel
239 might be expected to have distinct dynamics from the extracellular BL proteins nidogen and
240 laminin. We tested this idea using time-lapse imaging and fluorescence recovery after
241 photobleaching (FRAP) to determine the mobility and stability of the channel and ECM puncta.
242 In time-lapse imaging sessions, represented as kymographs in Figure 2C, we observed that
243 MEC-4, LAM-2 and NID-1 puncta are immobile over a time course of several minutes. During a
244 5-minute recovery period, photobleached MEC-4 puncta recovered only about 25% of initial
245 fluorescence levels and photobleached LAM-2 and NID-1 puncta did not recover any detectable
246 fluorescence (Figure 2D, Figure S2D). The limited mobility of laminin and nidogen observed in
247 mechanosensory complexes is specific to this environment, since laminin and nidogen in the
248 basal lamina around pharynx recover nearly 10 and 20% of their fluorescence, respectively, 5
249 minutes after photobleaching (Keeley et al., 2020). Additionally, the modest recovery of MEC-4
250 fluorescence after photobleaching is not a general property of proteins associated with the ALM
251 plasma membrane. SDN-1 syndecan, a transmembrane heparan sulfate proteoglycan that
252 uniformly coats the ALM (Figure 1D), recovered ~75% of its baseline fluorescence in the same
253 time frame (Figure 2D). These findings cannot be due to a general lack of fluidity or mobility in
254 the TRN plasma membrane, since myristoylated-GFP expressed in the TRNs recovers more than
255 half of its fluorescence within only 1 minute after bleaching (Figure S2B,C,E). The greater
256 apparent mobility of MEC-4 relative to LAM-2 and NID-1 could reflect exchange of channel
257 proteins between punctate and diffuse pools (see below). Collectively, these findings show that
258 MEC-4, LAM-2, and NID-1 molecules form stable, largely immobile, micron-scale structures
259 along TRN neurites *in vivo* and the unexpected similarity in their dynamics provides additional
260 support for the idea that these proteins function together.

261 Based on the similar distribution and dynamics of laminin, nidogen, and MEC-4 in the
262 ALMs (Figure 2A-D), we hypothesized that they belong to the same discrete puncta. To test this
263 idea directly, we developed dual-color transgenic animals expressing wSc- and mNG-tagged
264 protein pairs (Figure 2E). We quantified co-localization of protein pairs using two methods:
265 intensity correlation quotient or ICQ (Figure 2F) and object co-localization (Figure S2F, S2G).
266 The ICQ represents co-variation in fluorescence intensity as a single value between -0.5 and 0.5
267 (Li et al., 2004), denoting perfect anticorrelation and correlation, respectively. We validated both
268 co-localization metrics by comparing the results for real and simulated image pairs, which we
269 generated by randomly selecting red and green channels from different cells within each dataset.
270 As expected, ICQ values (Figure 2F, boxplots) and the fraction of co-located red and green
271 puncta (Figure S2F-G, boxplots) were close to zero for the simulated pairs. Thus, two lines of
272 evidence indicate that laminin and nidogen puncta strongly co-localize with each other and with
273 MEC-4 puncta (Figures 2E-F, S2F-G).

274 To place these metrics in context, we also analyzed strains with red and green
275 fluorophores either on the same protein (NID-1::wSc/NID-1::mNG) or on two proteins known to
276 be a part of an obligate heterotrimer (LAM-1::wSc/LAM-2::mNG). The slightly lower ICQ for
277 LAM-1/LAM-2 pair reflects the high background laminin fluorescence from surrounding tissues.
278 Importantly, ICQ values for NID-1/MEC-4 were similar to those measured for the NID-1/NID-1
279 control (Figure 2F, Table S2). The ICQ for NID-1/LAM-2 and LAM-1/MEC-4 pairs were
280 similar to each other and to the LAM-1/LAM-2 control (Figure 2F, Table S2). To determine
281 whether the small size of TRN neurites (200-300 nm in diameter) might yield spurious intensity
282 correlation, we also determined ICQ values for a pair of proteins that differ in their distribution
283 with the ALM neurites. For this purpose, we chose PAT-2 α-integrin and MEC-4, because they
284 are both membrane proteins expressed by the TRNs (Chen and Chalfie, 2014; Driscoll and
285 Chalfie, 1991; Taylor et al., 2021) and because PAT-2 appears uniformly distributed along the
286 ALM while MEC-4 is punctate (Figure 1C, Figure 2E). As expected for proteins that do not
287 colocalize to common structures but are present in the same diffraction-limited volume, the PAT-
288 2/MEC-4 pair yields ICQ values close to zero. Unlike other protein pairs, this value was not
289 significantly different from the ICQ calculated for simulated pairs of images.

290 In summary, we observed that the ECM proteins laminin and nidogen assume a punctate
291 distribution similar to MEC-4 MeT channels along TRNs. The positions of these puncta are
292 stable over several minutes and the molecules comprising the puncta are much less mobile than
293 other proteins in the same environment (SDN-1::mNG, myr::GFP) or the same proteins in other
294 environments [NID-1 and LAM-2 in pharynx (Keeley et al., 2020)]. These findings imply that
295 BL molecules are anchored to immobile structures associated with the TRNs. Additionally, we
296 observed that the positions of nidogen, laminin and MEC-4 channel puncta strongly correlate
297 with each other and that the fluorescence associated with each pair of proteins is strongly
298 correlated. Based on the evidence of similar punctate distributions, mobility, and fluorescence
299 colocalization and intensity correlation, we propose that the matrix (laminin and nidogen) and
300 membrane (MEC-4) components function together as mechanosensory complexes.

301

302 **MEC-4 released from mechanosensory complexes redistributes into a diffuse membrane**
303 **pool**

304 Prior evidence that loss of *mec-5*, *mec-1*, or *mec-9* function disrupts MEC-4 puncta
305 (Emtage et al., 2004) suggested to us that laminin and nidogen puncta might also depend on *mec-*
306 *5*, *mec-1,* and *mec-9*. To test this idea, we analyzed NID-1::wSc in *mec-5(u444)*, *mec-1(e1738)*
307 and *mec-9(u437)* null mutants. NID-1::wSc puncta were not detected along any of the mutant
308 ALM neurons, which were visualized by expression of a cytoplasmic GFP marker (Figure 3A).
309 No defects in NID-1::wSc fluorescence were observed in the BL around the pharynx (Figure
310 3B), gonad and body wall muscle (Figure S3A), however. Similar results were obtained using
311 LAM-2::mNG (Figure S3A,B). Thus, in *mec-1*, *mec-5* and *mec-9* mutants, laminin and nidogen
312 are lost specifically along the TRNs while remaining intact in the other basement membranes.

313 Consistent with previous reports (Emtage et al, 2004), we observed that mNG::MEC-4
314 puncta were markedly reduced in *mec-5(u444)*, *mec-1(e1738)* and *mec-9(u437)* mutant animals
315 *in vivo*. We next asked if physically separating TRNs from the native ECM would phenocopy
316 this effect. To achieve this goal, we dissociated cells from mNG::MEC-4 transgenic embryos and
317 cultured them on coverslips that we engineered to be covered in thin strips of adhesive proteins
318 (STAR*Methods). This approach constrained TRNs to extend straight neurites reminiscent of

319 their *in vivo* morphology. Even though dissociated embryonic TRNs are known to express *mec-1*
320 and *mec-9* (Zhang et al., 2002), mNG::MEC-4 puncta were reduced *in vitro* (Figure 3C,D). The
321 few bright punctate structures seen in mutants *in vivo* and in TRNs *in vitro* often co-localized
322 with the vesicle marker mCherry::RAB-3 (Figure 3C,D). In contrast to stationary MEC-4 puncta
323 in control animals, mobile MEC-4 puncta often exhibited bidirectional movement with frequent
324 pauses and reversals, reminiscent of vesicles transporting cargo (Figure S3C-E) and were distinct
325 from stationary MEC-4 aligned with stationary NID-1 puncta *in vivo* (Figure S3E). This suggests
326 that punctate MEC-4 structures seen in *mec-5*, *mec-1*, *mec-9* animals *in vivo* and in cultured
327 TRNs *in vitro* represent MEC-4 in vesicles. The average number of RAB-3 labeled puncta and
328 the average number of MEC-4 puncta that co-localize with RAB-3 puncta does not vary
329 significantly between control and ECM mutant genotypes *in vivo* (Figure S3F). In TRNs cultured
330 *in vitro*, the occurrence of punctate MEC-4 and RAB-3 varied among cells, but most MEC-4
331 puncta co-localized with RAB-3 puncta. The vesicular MEC-4 comprises a relatively minor
332 fraction of the total MEC-4 in ALM neurites on average (less than 10%), and this fraction also
333 does not change appreciably between control and ECM mutants *in vivo* (Figure 3D). For
334 simplicity, we discount the contribution of vesicular MEC-4 fluorescence in future
335 measurements.

336 ECM mutants exhibit a significant increase in the fraction of mNG::MEC-4 that appears
337 uniformly distributed along the TRN (Figure 3D). To understand whether these diffuse MEC-4
338 molecules are more mobile than those in discrete puncta, we performed FRAP studies of diffuse
339 mNG::MEC-4 in mutants and compared these results to FRAP studies of discrete puncta in
340 control animals (Figure 3E-F). This analysis focused on the *mec-1* and *mec-9* genes because they
341 are co-expressed in the TRNs (Du et al., 1996; Emtage et al., 2004). The *mec-5* gene is not
342 expressed in the TRNs (Du et al., 1996). As is evident from Figure 3F, FRAP profiles were more
343 variable in *mec-1* and *mec-9* mutants than in control animals. The mutant dataset includes
344 profiles in which the fractional recovery approached >50% after 5 minutes as well as those in
345 which the fractional recovery was less than 20% in the same time frame. On average, both
346 mutants had an increased fractional fluorescence recovery (*mec-1(e1738)*: 0.39±0.23 and
347 *mec-9(u437)*: 0.34±0.17 (mean±sd)) relative to control (0.25±0.13, mean±sd). Although the
348 difference is modest, it was statistically significant (One-way ANOVA). Post-hoc testing (Tukey
349 HSD) revealed a statistically significant increase in the fractional fluorescence recovery at 300 s

350 between in *mec-1(e1738)* mutants relative to control, but not between *mec-9(u437)* mutants vs.
351 controls (Figure S3G). Notably, the MEC-4 molecules present in *mec-1* and *mec-9* mutants are
352 much less mobile than other membrane proteins such as SDN-1 (Figure 2D), a finding which
353 implies that other factors act in parallel to limit MEC-4 mobility. Taken together, these findings
354 imply that the neuronal factors, *mec-1* and *mec-9*, are required to properly structure the
355 mechanosensory BL and that, in their absence, MEC-4 is redirected into a diffuse membrane
356 pool. This analysis also provides new insight into the role RAB-3 positive vesicles might play in
357 the subcellular distribution of mechanosensory channels in sensory neurons *in vitro* and *in vitro*.

358

359 **Neither MeT channels nor TRN microtubules are required to assemble the matrix**
360 **components of the mechanosensory complexes**

361 Having established that MEC-4, laminin, and nidogen co-localize to stable, stationary
362 complexes in the ALM neurons, we next used genetic dissection to learn more about how these
363 complexes are assembled. We first measured laminin and nidogen puncta in *mec-4* null mutants.
364 LAM-2 and NID-1 puncta were unaffected by loss of *mec-4* (Figure 4A-C, Table S2), indicating
365 that although MEC-4 is an essential pore-forming subunit of the MeT channel in the TRNs
366 (O'Hagan et al., 2005), it is not needed to form ECM puncta along TRN neurons. Since MEC-4
367 is proposed to form heterotrimers with MEC-10, DEGT-1, or both channel proteins (Árnadóttir
368 et al., 2011; Chatzigeorgiou et al., 2010; O'Hagan et al., 2005), we asked if these other
369 DEG/ENaC/ASIC channel subunits were required for ECM puncta formation. As found for
370 *mec-4* single mutants, laminin puncta were unaffected in *degt-1;mec-4mec-10* triple mutants
371 (Figure S4A-C). This finding, along with previous studies reporting that the distribution of ECM
372 proteins MEC-1 and MEC-5 along the TRN are also not affected by loss of MEC-4 (Emtage et
373 al., 2004), suggests that MeT channels are not sufficient by themselves to nucleate
374 mechanosensory complexes in TRNs.

375 We also found that NID-1::wSc puncta distribution along the ALM neurite was
376 minimally affected in animals carrying a null allele of the TRN-specific β-tubulin *mec-7* gene. In
377 the *mec-7(ok2152)* mutant background, both NID-1 and MEC-4 puncta were clearly visible in
378 the proximal neurite (Figure 4D). Consistent with data reported earlier using *mec-7(u440)* allele

379 (Emtage et al., 2004), MEC-4 puncta were dimmer and harder to identify in *mec-7(ok2152)*
380 mutants, especially in the distal ALM. Although fewer MEC-4 molecules were present in the
381 *mec-7(ok2152)* animals, the distribution between the punctate and diffuse pool was similar to
382 that seen in control animals (Figure S4D). In contrast, NID-1 puncta were clearly visible along
383 the entire ALM (Figure 4D). These effects are likely to account for the lower ICQ values for
384 NID-1 and MEC-4 (Figure S4E) observed in this mutant. At the same time, the MEC-4 and
385 NID-1 puncta that remained co-localized one another (Figure S4F-G). Thus, loss of MEC-7
386 β-tubulin reduces MEC-4 expression, as reported (Bounoutas et al., 2011), but does not appear to
387 prevent formation of mechanosensory complexes.

388

389 **Mechanosensory complex formation depends on nidogen and laminin**

390 Next, we sought to determine whether laminin and nidogen were essential to form
391 mechanosensory complexes and to position MEC-4 channels. We could not analyze
392 mechanosensory puncta in laminin null mutant adults because loss of any of the four laminin
393 genes, *epi-1, lam-3, lam-1,* and *lam-2,* causes lethality in *C. elegans* embryos or larvae (Kao et
394 al., 2006). We could, however, analyze the laminin-α *lam-3(ok2030)* mutant animals that do not
395 develop past L1 stage and small number of *epi-1(gm57)* mutants that survive to adulthood
396 (Forrester et al., 1998). Given that laminin-α is essential for laminin trimer assembly (Kao et al.,
397 2006; Yurchenco et al., 1997), investigating MEC-4 channel position in *epi-1* and *lam-3* laminin-
398 α mutants provides insight on the role that laminin trimers play in organizing mechanosensory
399 puncta.

400 We analyzed and compared MEC-4 puncta in control, *epi-1(gm57)*, and *lam-3(ok2030)*
401 mutant L1 larvae. As in adults, MEC-4 localized to discrete puncta in control L1 larvae (Figure
402 5A). *epi-1(gm57)* L1 animals had MEC-4 puncta similar to control animals, with IPIs that are
403 only marginally higher on average from control (Figure 5A-C). In the few *epi-1(gm57)* mutant
404 animals that survive to adulthood, the ALM cell bodies and sensory neurites displayed ectopic
405 branching and multiple segments were seen adjacent to the body wall muscle, displaced from
406 their control position (Figure S5A). TRN neurite segments that were adjacent to the body wall
407 muscle in *epi-1(gm57)* mutants displayed only diffuse mNG::MEC-4 fluorescence. By contrast,

408 segments that retained their wild-type position retained discrete MEC-4 puncta with IPIs
409 indistinguishable from control animals (Figure S5B-C, Table S2). Thus, wild-type EPI-1
410 laminin-α is required to position the ALM neurons in the worm's body, but dispensable for
411 positioning mechanosensory complexes along properly attached ALM neurons. In
412 *lam-3(ok2030)* larvae, MEC-4 puncta were either undetectable or when visible (Figure 5A), they
413 were fewer in number and more widely separated. The increase in the reported mean and median
414 IPI values in *lam-3(ok2030)* larvae compared to control (Figure 5B-C, Table S2) underestimates
415 the effect of *lam-3* loss-of-function, since in 50% (17/34) of the *lam-3(ok2030)* L1 larva we
416 imaged mNG::MEC-4 signal in the ALM could not be visualized distinctly and were thus not
417 analyzed. Thus, while EPI-1 adheres to TRNs (Figure 1D) and is needed to maintain proper
418 ensheathment within epidermal cells, LAM-3 is needed for mechanosensory complex assembly.
419 The two *C. elegans* laminins proteins play distinct, but overlapping roles in mechanosensation,
420 as they do in embryonic development (Huang et al., 2003).

421 Like laminin, nidogen is a core BL protein that is conserved in all vertebrates and
422 invertebrates (Mayer et al., 1998). Unlike laminin, nidogen is not needed for BL assembly
423 (Ackley et al., 2003; Bader et al., 2005; Böse et al., 2006; Dai et al., 2018; Dong et al., 2002;
424 Kang and Kramer, 2000; Kim and Wadsworth, 2000; Murshed et al., 2000; Schymeinsky et al.,
425 2002; Wolfstetter et al., 2019) and nidogen null mutants develop into grossly normal adult
426 worms (Kang and Kramer, 2000). Both MEC-4 channel puncta and LAM-1 puncta were dimmer
427 and spaced further apart in *nid-1* mutants compared to control animals (Figure 5D-F). The
428 decrease in mechanosensory complex density was accompanied by an increase in the proportion
429 of MEC-4 protein present in the diffuse membrane pool (Figure S5D), resulting in a low LAM-
430 1/MEC-4 ICQ value in the *nid-1* mutant (Figure S5E). However, a majority of the remaining
431 MEC-4 and laminin puncta were still co-localized (Figure 5G, Figure S5F-G). Collectively, these
432 findings reinforce the idea that MEC-4 channels redistribute to a diffuse membrane pool
433 following perturbations of mechanosensory complexes and that BL play an instructive role in the
434 assembly or stability of sensory complexes.

435 Despite the significantly lower density of mechanosensory complexes along the TRNs,
436 *nid-1* animals were not significantly less touch sensitive. In the standard touch response assay,
437 where the animals were stroked with an eyebrow hair, the *nid-1* animals scored only slightly

438 lower than control animals and significantly more than the *mec-4(u253)* and *mec-5(u444)*
439 animals (Figure 5H). Given that the force delivered during these assays far exceeds saturation
440 (Nekimken et al., 2017), this assay is not able to detect small changes in touch sensitivity or in
441 activation of MeT channels. Accordingly, we used *in vivo* whole-cell patch recording to directly
442 determine how loss of *nid-1* affects the response to body indentation. To optimize our ability to
443 detect a partial loss-of-function, we then used an ultrafast mechanical stimulator that evokes
444 currents that are approximately five-fold larger than those evoked by slower stimuli (Katta et al.,
445 2019). Using this approach, we found that mechanoreceptor currents or MRCs were qualitatively
446 similar in *nid-1* mutants and wild-type controls (Figure 5I), but that MRC amplitude was
447 decreased in *nid-1* mutants (Figure 5J). The effect of *nid-1* is specific to MRCs, since voltage-
448 gated currents were similar to wild-type controls in all respects (Figure S5H-I). Thus, we
449 conclude that the lower MRCs found in *nid-1* mutants arise from the decreased density of
450 sensory complexes. This finding is consistent with computational studies indicating that stimulus
451 intensity, speed, and channel density govern MRC amplitude (Katta et al., 2019).

452

453 **Nidogen and laminin inclusion in mechanosensory complexes is independent of direct**
454 **interaction between nidogen and laminin**

455 Wild-type, NID-1 protein contains three conserved globular domains, G1, G2 and G3
456 (Figure 6A). The N-terminal G1 and G2 domains are connected by a flexible linker, whereas the
457 G2 and G3 domains are connected by a more rigid rod-like domain consisting of a series of EGF
458 motifs (Fox et al., 1991; Patel et al., 2014). Multiple studies with recombinant mouse nidogen
459 fragments show that perlecan binds exclusively to the G2 domain, laminin-γ1 binds exclusively
460 to the G3 domain, collagen IV and fibulin-1C bind to the G2 and G3 domains, and fibulin-2
461 binds to all three globular domains (Fox et al., 1991; Kvansakul et al., 2001; Reinhardt et al.,
462 1993; Ries et al., 2001). To understand which of the globular domains are important for the
463 formation of mechanosensory complexes in worms, we first looked at the *nid-1(cg118)* allele,
464 which encodes a large in-frame deletion of G1, G2 and part of the first EGF motif of the rod
465 domain (Figure 6A). In *nid-1(cg118)* mutants, MEC-4 puncta distributions were similar to wild-
466 type (Figure 6C-E top, Table S2). Thus, neither the G1 nor the G2 domains of nidogen are
467 required to assemble or position mechanosensory complexes. The G1 and G2 domains of

468 nidogen are likewise dispensable for expression of NID-1 protein during embryonic development
469 and in BL associated with muscles, the somatic gonad, and neuronal tracts (Kang and Kramer,
470 2000).

471 Next, we examined the role of the nidogen G3 domain thought to bind to laminin-ɣ,
472 collagen IV and fibulin (Aumailley et al., 1993; Fox et al., 1991; Mann et al., 1988, 1989; Mayer
473 et al., 1998; Patel et al., 2014; Ries et al., 2001; Takagi et al., 2003). We used CRISPR mediated
474 genome editing to create a NID-1[ΔG3] mutant (*pg146)* deleting the amino acids 1294-1546.
475 Like *nid-1(cg119)* null mutants (Ackley et al., 2003; Kang and Kramer, 2000), the NID-1[ΔG3]
476 mutants developed into grossly wild-type adult animals. Also similar to *nid-1(cg119)*, MEC-4
477 puncta were dimmer and spaced further apart in NID-1[ΔG3] mutants (Figure 6C-E middle,
478 Table S2), with a corresponding increase in the fraction of MEC-4 in the diffuse pool (Figure
479 S6A), and a slightly reduced touch response behavior compared to control animals (Figure S6B).
480 Thus, the NID-1 G3 domain is required for MEC-4 puncta distribution. Given that the NID-
481 1[ΔG3] mutant phenocopies the *nid-1(cg119)* null allele with respect to MEC-4 puncta
482 distribution, we asked whether this is due to the inability of the truncated NID-1[ΔG3] protein to
483 incorporate into mechanosensory complexes by visualizing a wSc-tagged NID-1[ΔG3] isoform.
484 Consistent with the idea that the G3 domain is required to incorporate NID-1 into BL, NID-
485 1[ΔG3]::wSc fluorescence was severely reduced in the BL around the pharynx, body wall
486 muscle and gonad. However, NID-1[ΔG3]::wSc was visible in neuronal-associated BL,
487 including the nerve ring and in puncta along ALM neurons (Figure S6C-E). These findings
488 imply that although the nidogen G3 domain is required to incorporate nidogen into conventional
489 BL and is required for wild type mechanosensory puncta distribution, it is dispensable for
490 inclusion into neuronal BL and into the residual mechanosensory puncta along TRNs.

491 Since the nidogen G3 domain has been shown to bind laminin-ɣ, collagen IV and fibulin
492 (Aumailley et al., 1993; Fox et al., 1991; Mann et al., 1988, 1989; Mayer et al., 1998; Patel et al.,
493 2014; Reinhardt et al., 1993; Ries et al., 2001; Takagi et al., 2003), we then asked which of these
494 interactions are important for mechanosensory complex formation. Structural and biochemical
495 evidence mapped the nidogen binding site on mouse laminin-ɣ1 to three critical amino acids
496 (D800, N802, V804) on a unique loop in the 8th EGF motif (Pöschl et al., 1994; Pöschl et al.,
497 1996; Takagi et al., 2003) (Figure 6B). Each of these residues when individually mutated

498 reduced the binding affinity between nidogen and laminin by several orders of magnitude
499 (Pöschl et al., 1994). In a proteome-wide search for a similar motif in *C. elegans*, we found that
500 the 8th EGF motif on both laminin-ɣ LAM-2 and laminin-α LAM-3 contained this loop with
501 partially conserved residues as shown in Figure 6A-B. We predicted that the EPI-1 containing
502 laminin has only one binding site for nidogen (on LAM-2) while the LAM-3 containing laminin
503 has two binding sites for nidogen (on both LAM-2 and LAM-3). We sought to disrupt the
504 nidogen-laminin binding interface by engineering mutations in the putative nidogen binding
505 residues in both LAM-2 (LAM-2[D842N, N844S, I846S]) and LAM-3 (LAM-3[D896N, M898S,
506 I900S]). We refer to these triple amino acid substituted alleles as LAM-2[NSS] and
507 LAM-3[NSS], respectively. We chose these amino acid substitutions because they had the
508 largest fold-change in binding affinity between mammalian nidogen and laminin-γ1 fragments *in*
509 *vitro* (Mayer et al., 1998; Pöschl et al., 1996).

510 Unlike *lam-2* and *lam-3* null mutants, LAM-2[NSS], LAM-3[NSS] as well as the
511 LAM-2[NSS];LAM-3[NSS] double mutant animals were viable with no apparent defects in
512 gross morphology or development. LAM-2[NSS]::mNG showed a similar distribution as WT
513 LAM-2::mNG in all tissues (Figure S6C-E). As expected for loss of nidogen-laminin binding,
514 NID-1::wSc fluorescence was absent in the BL lining the pharynx and body wall muscle in
515 LAM-2[NSS];LAM-3[NSS] double mutants (Figure S6C-E). NID-1::wSc fluorescence was
516 reduced but not completely lost around the same tissues in the LAM-2[NSS] single mutant
517 (Figure S6C-E), indicating that the nidogen binding site on LAM-3 was sufficient for recruiting
518 nidogen to BL with LAM-3 containing laminin. Conversely, NID-1::wSc fluorescence was
519 similar to the wild-type control in the LAM-3[NSS] single mutant (Figure S6C-E), indicating
520 that the nidogen binding site on LAM-2 which is present in both types of laminin is also
521 sufficient for recruiting nidogen. Despite these dramatic effects in conventional basal lamina,
522 LAM-2[NSS];LAM-3[NSS] double mutants appeared to retain NID-1 in the nerve ring (Figure
523 S6D) and also retained a near wild-type puncta distribution of MEC-4, NID-1 and LAM-2 along
524 the ALM (Figure 6C-E bottom, Table S2, Figure S6E). Collectively, these findings suggest that
525 1) nidogen redundantly binds to LAM-2 and LAM-3 using similar binding interfaces, 2) laminin-
526 nidogen binding is not essential for the recruitment of either laminin, nidogen or MEC-4 into
527 mechanosensory complexes, 3) the nidogen G3 domain likely interacts with another factor that
528 regulates the spacing of the mechanosensory complexes along TRNs.

529 The other likely nidogen G3-binding factors are collagen IV or fibulin. Cross-linking of
530 laminin and collagen networks via nidogen have been shown to be important for the integrity of
531 many types of BL (Hamill et al., 2009). *C. elegans* expresses two canonical collagen IV proteins,
532 EMB-9 and LET-2, neither of which have been detected along TRNs in our screen (Table S1) or
533 in previous studies (Graham et al., 1997). The only known collagen-like protein known to be
534 present around TRNs is MEC-5, which is significantly smaller in length than the canonical
535 collagen IV proteins. It is well-known that loss of MEC-5 disrupts touch sensation (Du et al.,
536 1996; Gu et al., 1996) and we have shown in Figure 3 that mNG::MEC-4 and NID-1::wSc
537 puncta along the ALM are lost in the *mec-5* mutant animals. However, since the specific binding
538 sites between collagen IV and nidogen are unknown and we have not been able to fluorescently
539 label MEC-5 without affecting its function, we have not been able to test whether NID-1's
540 collagen IV binding activity is necessary for mechanosensory complex formation. *C. elegans* has
541 one fibulin encoding gene, *fbl-1*, and fibulin protein is present along the ALMs (Figure 1C, and
542 (Muriel et al., 2005)). The mNG::FBL-1 strain was touch insensitive (Table S2), but *fbl-1* loss of
543 function mutants retained an essentially wild-type distribution of MEC-4 puncta along the ALM
544 neuron (Table S2). Further experiments are necessary to fully understand the role of nidogen
545 binding to collagen and fibulin in mechanosensory complex formation and function.

546

547 **MEC-1 connects the MEC-4 channel to ECM components of the sensory complex**

548 The *mec-1* gene is predicted to encode a large protein containing fifteen Kunitz (Ku)
549 domains [Figure 7Aand (Emtage et al., 2004)] and similar motifs are found in peptide toxins that
550 bind to ion channels including ASIC channels (Mishra, 2020; Cristofori-Armstrong and Rash,
551 2017). This raises the possibility that these toxins mimic endogenous Ku domain proteins that
552 bind to the extracellular domains of DEG/ENaC/ASIC channels. Consistent with this idea,
553 MEC-1 Ku15 shares 33% sequence identity with the snake neurotoxin MitTx-α (Bohlen et al.,
554 2011) (Figure 7B). We investigated this idea *in vivo*, leveraging known and new missense
555 mutations affecting MEC-1 Ku15. The existing *mec-1(e1526)* and *mec-1(u811)* alleles lead to
556 the expression of full-length MEC-1[R1804C] and MEC-1[C1808Y], respectively. Unlike the
557 residue affected in *e1526* allele, the one affected in *u811* is conserved and predicted to form a
558 disulfide bond likely to be integral to folding Ku15 (Figure 7B). *mec-1(e1526)* and *mec-1(u811)*

559 animals are known to be touch insensitive (Emtage et al., 2004), but how these mutations affect
560 all elements of mechanosensory complexes is not known. Using CRISPR/Cas9 genome editing,
561 we mutated C1808 of Ku15 tyrosine (encoded by the *pg164* allele), to recreate the *u811*
562 mutation. Using dual-color transgenic animals expressing NID-1::wSc and mNG::MEC-4, we
563 found that both *e1526* and *pg164* alleles retained nidogen puncta but very few mNG::MEC-4
564 puncta (Figure 7C-F). NID-1 puncta were distributed in a manner nearly indistinguishable from
565 control animals in MEC-1[R1804C] mutants (Figure 7C-E, top row), while NID-1 puncta were
566 denser in the MEC-1[C1808Y] animals (Figure 7C-E, bottom row, Figure 7F, Table S2).
567 Laminin puncta were also retained in the MEC-1[R1804C] mutant animals and co-localized with
568 nidogen (Figure S7). Collectively, these results demonstrate that an intact Ku15 is needed to link
569 MEC-4 to BL structures. Additional support for this conclusion comes from the findings that, in
570 these *mec-1* missense alleles, the bulk of mNG::MEC-4 fluorescence shifts to the diffuse pool
571 (Figure 7G, Table S2), ICQ values for MEC-4/NID-1 are reduced (Figure 7H, Table S2), and
572 animals are strongly touch-insensitive (Figure 7I). The findings from perturbations in Ku15 and
573 their distinct effects on MEC-4, laminin, and nidogen puncta, are consistent with the hypothesis
574 that MEC-1 physically binds to MEC-4 through Ku15.

575

576 **Discussion**

577 Across animal taxa (Yin et al., 2021), the endings of vibrotactile sensory neurons are
578 intimately associated with epidermal cells and basal laminae. Leveraging a suite of transgenic *C.*
579 *elegans* expressing fluorescent-protein fusions from the endogenous loci of BL-encoding genes
580 in the genome, we show that 12 conserved BL proteins are associated with TRNs in living
581 animals. Among these, only laminin-β (LAM-1), laminin-γ (LAM-2) and nidogen (NID-1),
582 display a punctate distribution along the TRNs but not in other tissues. Drawing upon still and
583 time-lapse imaging of BL proteins and the MEC-4 ion channel subunit tagged alone and in pairs,
584 FRAP studies, and genetic dissection, we provide evidence that laminin and nidogen co-localize
585 with the MEC-4 channels responsible for touch sensation. These mechanosensory complexes are
586 stationary and remarkably stable and we propose that they link the neuronal membrane to the
587 extracellular matrix. At just over 1 µm long (Figure S2A) and separated by ~4-5 µm (Table S2),
588 on average, their dimensions are on par with the size and spacing of arrays of beam-like

589 structures seen in ECM in serial-section TEM data stacks. These similarities prompt us to
590 speculate that mechanosensory complexes associate with these structures (Figure 7J) and that the
591 structures contribute to the immobility of the laminin, nidogen and MEC-4 puncta.

592 Consistent with this idea, MEC-4 redistributes to a less stable and more diffuse
593 membrane pool in *mec-1* and *mec-9* mutants lacking discernable organized BL structures (Figure
594 3). Given that these mutants are completely touch insensitive (Du et al., 1996; Emtage et al.,
595 2004), the MEC-4 proteins present in the diffuse membrane pool are not capable of supporting
596 mechanosensation. A similar situation is evident in cultured TRNs physically separated from
597 epidermal cells and their native BL structures. The few MEC-4 puncta that are present in these
598 conditions seem to represent MEC-4 molecules that are sequestered in RAB-3-positive vesicles
599 (Figure 3). Since cultured TRNs appear to maintain their cell-autonomous gene expression
600 profiles (Zhang et al., 2002), their voltage-activated currents (Christensen and Strange, 2001),
601 and their shape [this study and (Christensen and Strange, 2001; Christensen et al., 2002;
602 Lockhead et al., 2016; Zhang et al., 2002), the failure to form mechanosensory puncta most
603 likely arises from the physical separation from epidermal tissues and the subsequent disruption in
604 the organization of laminin and nidogen along TRNs. The failure to maintain or recapitulate the
605 *in vivo* organization of mechano-electrical transduction channels *in vitro* may have broad
606 implications for studies of dissociated and cultured sensory neurons.

607 Loss of nidogen causes mild defects in behavioral and electrophysiological responses to
608 touch (Figure 5H-J) and a substantial reduction in the density of MEC-4 and laminin puncta as
609 well as the strength of their colocalization. This implies that the mechanosensory complexes
610 retained in *nid-1* mutants (~half of all MEC-4 puncta co-localize with LAM-1 and *vice versa*,
611 Table S2, Figure S5) are fully functional and that nidogen plays a central role in their assembly
612 or stability, but a minor role in their activation. It also implies that tactile sensing in *C. elegans* is
613 robust, since nearly normal behavior is retained even though half of the MEC-4 channels are not
614 properly aligned with their BL partners. By contrast, loss of MEC-7 β-tubulin causes severe
615 defects behavioral and electrical responses to touch (Savage, et al., 1981; O'Hagan, et al., 2005),
616 but modest decreases in the density of MEC-4 and nidogen puncta (Figure 4D-F) and their
617 colocalization. Indeed, we found that more than two-thirds of MEC-4 puncta co-localized with
618 NID-1 in *mec-7* mutants and *vice versa* (Table S2, Figure S4). Because MeT currents can be

619 activated in *mec-7* mutants (O'Hagan, et al., 2005), however, the mechanosensory dysfunction in
620 these mutants cannot be due to a complete loss of force transfer arising from disruptions to
621 microtubules that also occurs in *mec-7* mutants (Chalfie and Sulston, 1981). Thus, more complex
622 mechanisms or a combination of effects are needed to account for touch-insensitivity in this
623 background, and any model would also need to consider the fact that *mec-7* decreases expression
624 of the *mec-3* transcription factor and genes that require *mec-3* for their expression (Bounoutas et
625 al., 2011). Thus, while *nid-1* mutants display essentially normal touch sensitivity with only half
626 the channels aligned to BL puncta, *mec-7* mutants are effectively numb to touch despite retaining
627 a significantly larger fraction of aligned channels. From these cases, we infer that proper
628 organization of membrane-matrix complexes is necessary but that their proper placement is not
629 sufficient by itself to support full vibrotactile sensation.

630 Laminin is a heterotrimeric molecule containing alpha, beta and gamma subunits
631 (Aumailley, 2013), implying that one or both of the *C. elegans* alpha laminins also localize to the
632 TRN-epidermal cell interface. Our experimental results are consistent with a model in which there
633 are two distinct laminin networks bridging the gap between epidermal cells and the TRNs (Figure
634 7J). For instance, we found that EPI-1 uniformly coats the ALM (Figure 1) and that loss of *epi-1*
635 function disrupts TRN attachment, but not the organization of MEC-4 puncta (Figure S5A-C).
636 These findings suggest that an EPI-1/LAM-1/LAM-2 network coats the ALM uniformly at its
637 interface with the ALM and is necessary for proper ALM ensheathment. They imply the presence
638 of a uniformly distributed component of LAM-1 and LAM-2, in addition to the punctate
639 component that we already described. This uniform component may be obscured in wild-type
640 animals by the intense puncta and fluorescence from adjoining tissues. Indeed, LAM-2::mNG and
641 NID-1::wSc were detected as a faint, but uniform fluorescence adhered to the ALM (Figure 3A,
642 Figure S3B) in *mec-1(e1738)* and *mec-9(u437)* mutants lacking discrete laminin and nidogen
643 puncta. Further, we posit that LAM-3/LAM-1/LAM-2 trimers form puncta along TRNs and that
644 these laminin networks are necessary for MEC-4 puncta distribution. This model also predicts the
645 presence of LAM-3 in a punctate distribution along the ALM, which we did not detect with
646 fluorescently labeled LAM-3. New tools will be needed to test these predictions in detail and to
647 discover other protein partners present in these networks. The proposed arrangement of two types
648 of laminin networks would help to firmly link the ALM sensory ending to the surrounding
649 epidermal cell.

650 We propose that sensory neurons instruct the assembly of mechanosensory complexes
651 and discontinuous arrays of ECM beams seen in TEM data stacks. Two lines of evidence favor
652 this idea. First, two genes expressed by the TRNs, *mec-1* and *mec-9,* are required to form
653 aligned, stable complexes containing MEC-4, laminin, and nidogen. Both genes are predicted to
654 encode secreted extracellular matrix proteins (Du et al., 1996; Emtage et al., 2004). Collectively,
655 these observations suggest that these proteins could activate the assembly of discrete ECM
656 structures. Second, ECM beams are formed adjacent to the AVM neuron in the ventral nerve
657 cord at its interface with epidermal cells, but not neighboring neurons that share an interface with
658 the same epidermal cell (Figure S1E). The MEC-1 protein plays additional roles. Prior work
659 showed that it is required to attach the TRN to the epidermis and helps to ensure the proper
660 positioning of its sensory neurite in the body (Emtage et al., 2004), but it is dispensable for force
661 transfer from the skin to the TRN (Nekimken et al., 2020). Here, we establish that MEC-1
662 harbors specific domains required for co-assembly and alignment of MEC-4, laminin and
663 nidogen. In particular, mutations predicted to disrupt folding of the C-terminal Kunitz domain in
664 MEC-1 leave laminin and nidogen ECM structures intact but disrupt MEC-4 localization (Figure
665 7). Further experiments will test whether MEC-1 physically bridges the MeT channels with the
666 ECM beams, as illustrated in Figure 7J, and whether these structures help transmit force to MeT
667 channels.

668 Wherever neurons meet skin or muscle cells, the gap between them may well be occupied
669 by BL proteins like laminin and nidogen. The BL is an active molecular medium, as evidenced
670 by the fact that laminin plays an instructive role in organizing ion channels at the neuromuscular
671 junction (Rogers and Nishimune, 2017) and instructing the formation of dendritic arbors (Yang
672 and Chien, 2019). Laminin also governs the mechanosensitivity of cultured mouse dorsal root
673 ganglion neurons (Chiang et al., 2011; Hu et al., 2010). In this study, we identified laminin and
674 its binding partner, nidogen, as pivotal partners for organizing and immobilizing the mechano-
675 electrical transduction channel, MEC-4, along *C. elegans* TRNs. Two other sensory mechano-
676 electrical transduction channels also localize to discrete subcellular positions in fixed samples:
677 NOMPC (Lee et al., 2010; Liang et al., 2011) and Piezo2 (Handler et al., 2023). These channels
678 also appear to localize at the interface between sensory nerve endings and skin cells, although
679 their stability, dynamics, and positioning relative to the BL is not yet known. Our findings extend

680 the role of the BL from structure to function and defines a mechanosensory apparatus as a
681 multiprotein complex linking the neuronal membrane to the BL matrix.

682

683 **Limitations of the study**

684 This study characterizes electron-dense structures and mechanosensory protein
685 complexes at the sensory neuron-epidermal cell interface. The complexes are essential for touch
686 sensation and contain both neuronal MeT channels and extracellular assemblies of laminin and
687 nidogen; they depend on secreted neuronal factors proposed to transform continuous basal
688 lamina into discrete, stable, and stationary complexes. However, there are limitations that require
689 further investigation or new tools. Despite conducting a comprehensive visual screen of more
690 than two dozen ECM proteins, it is likely that additional proteins are present at the sensory
691 neuron-epidermal cell interface. Of the proteins we analyzed, one tagged protein was not visible
692 in any tissue in adult animals (LAM-3 α-laminin) and another tagged protein caused defects in
693 touch sensation (FBL-1). Tagging MEC-1 and MEC-5 at their endogenous loci disrupted touch
694 sensation, limiting our ability to re-examine the location of these proteins and to investigate their
695 interaction with *mec-4* and *nid-1* mutants. The widespread distribution of the visible laminin
696 subunits (LAM-1, LAM-2, EPI-1) contributed to background fluorescence that affected our
697 analyses of their distribution and colocalization with the MEC-4 ion channel. Additionally, we
698 could not systematically study how loss of laminin affects mechanosensory complex assembly,
699 stability, or function since loss-of-function mutations in all four laminin genes cause embryonic
700 or larval lethality. Biochemical studies and purification of this ion channel-ECM complex from
701 *C. elegans* are hampered by the scarcity of channel proteins relative to ECM proteins. Identifying
702 the protein partners that comprise nanostructures such as the ECM beams visible in serial-section
703 TEM structures is notoriously difficult and may require new technical approaches. The anatomy
704 and molecular physiology of the *C. elegans* TRNs differs from other somatosensory neurons
705 with respect to their position within the skin and the ion channels responsible for
706 mechanotransduction. Therefore, it may be challenging to immediately apply these results to
707 other sensory neurons and organisms, including those already known to share an intimate
708 association with epidermal cells. Despite these limitations, this study is a first step toward
709 deciphering the active nature of the interaction between sensory neurons and skin.

710 **Acknowledgements**

711 We thank Tom Clandinin, Ellen Kuhl, and Lucy Wang for comments and advice; the
712 entire WormsenseLab for feedback on experimental and analytical design; Zhiwen Liao for
713 technical support and worm injections; Juan Cueva for pilot studies, quantification of ECM
714 beams in ssTEM datasets, and 3-D visualization of ECM beams; and Richard Fetter for
715 contributing independently generated ssTEM datasets. Martin Chalfie, Kang Shen, David
716 Sherwood, and the Caenorhabditis Genetics Center (supported by the NIH Office of Research
717 Infrastructure, P40 OD010440) provided *C. elegans* strains. We are especially grateful to David
718 Sherwood for sharing key transgenic strains prior to publication. Confocal fluorescence imaging
719 and legacy ssTEM datasets used instruments in the Stanford University Cell Sciences Imaging
720 Core Facility (RRID:SCR_017787) and protein micropatterning used instruments in the Stanford
721 Nanofabrication Facility (supported by NSF Award ECCS-2026822). Additional ssTEM images
722 were acquired at the Nanoscale Biomedical Imaging Facility, Toronto. Research funded by an
723 NIH grant R35NS105092 to MBG, CIHR foundation scheme 154274 to MZ, F99NS115219
724 fellowship to JAF, and a F32NS116193 fellowship to DC.

725

Author contributions

Conceptualization, A.D., J.F., B.M., D.C., M.B.G.;
Methodology, A.D., J.F., B.M., L.W., C.J.;
Software, A.D., J.F., L.W.;
Validation, A.D., J.F., L.W.;
Formal analysis, A.D., J.F., B.M., L.W.;
Investigation, A.D., J.F., B.M., L.W., D.C., C.J.;
Resources, A.D., J.F., L.W., B.P., E.K., M.Z., M.B.G.;
Data Curation, A.D., J.F., B.M., L.W.;
Writing - Original draft, A.D., J.F., L.W., D.C.;
Writing - Review and editing, A.D., J.F., L.W., D.C., B.M, M.Z., M.B.G.;
Visualization, A.D., J.F., L.W.;
Supervision, A.D., M.Z., M.B.G.;
Project administration, A.D., M.Z., M.B.G.;
Funding acquisition, M.Z., M.B.G.

Declaration of Interests

The authors declare no competing interests.

744 **Figure Legends**

745

746 ***Figure 1. Conserved basal lamina (BL) proteins and arrays of beam-like nanostructures***
747 ***associate with TRNs in vivo***

748 **A.** Schematic diagram of an adult *C. elegans* nematode, showing the positions of the
749 TRN cell bodies and neurites relative to the body wall muscles (purple). Only the left ALM and
750 PLM are shown.

751 **B.** Schematic diagram of a cross-section of an adult worm, showing the body wall
752 muscles (purple), epidermis (beige) and basal lamina (green). Enlarged view of the ALM
753 neurons (yellow) embedded within the epidermis are shown in the middle and right panels.

754 **C.** Nine BL proteins uniformly coat TRN neurites *in vivo.* (Top left) Schematic diagram
755 of an enlarged view of the boxed area in panel A, showing the lateral view of an ALM cell body
756 and part of the ALM neurite relative to the body wall muscle (purple). Representative confocal
757 fluorescence micrographs of adult TRNs in transgenic animals expressing BL proteins visualized
758 using CRISPR/Cas9 to insert mNG or GFP (SAX-7, LET-805) into native loci. Panels show
759 ALM neurons coated with BL proteins, oriented as shown in the upper left panel: (left column)
760 SAX-7 L1CAM, LET-805 myotactin, MIG-6 papillin, PAT-2 α-integrin, (right column) SDN-1
761 syndecan, HIM-4 hemicentin, UNC-52 perlecan, FBL-1 fibulin, and EPI-1 laminin-α. Scale bars:
762 10 µm. Table S1 lists the strains screened and shown in this figure.

763 **D.** Two BL proteins localize to discrete puncta along TRN neurites. Fluorescence
764 confocal micrographs showing LAM-2::mNG laminin-ɣ and NID-1::mNG nidogen localizing to
765 discrete puncta distributed along the ALM neurons. Scale bar: 10 µm.

766 **E.** (Left) A reconstruction from serial section TEM images (total length = 3 µm) of
767 ALML in control animals [TU2769 *uIs31*[*mec-17p::GFP*] III], showing the ALM (yellow),
768 ECM beams (red) and the plasma membrane of the engulfing epidermis (translucent blue).
769 (Right, top) TEM micrographs of a *C. elegans* nematode (wild-type, N2) selected from a serial
770 section stack, spanning approximately 10 µm. Red arrows point towards the electron dense ECM
771 beams in the extracellular space between the ALM and the epidermis. (Right, bottom) A map of
772 the entire serial section stack of TEM images used for the top panel, showing the relative
773 position of the segments with (red) or without (yellow) visible ECM beams. Red numbers

774 indicate the length (in microns) of segments with visible ECM beam arrays. Black numbers
775 indicate the distance (in microns) between the mid-points of successive red segments. Additional
776 examples shown in Figure S1.
777

778 ***Figure 2. Laminin, nidogen, and MEC-4 co-localize to stationary, stable mechanosensory***
779 ***complexes.***
780 **A.** Representative widefield fluorescence images of puncta along ALM neurons for LAM-
781 1::wSc, LAM-2::mNG, NID-1::wSc and mNG::MEC-4 (from left to right).
782 **B.** Probability density distributions plot of inter-punctum intervals (IPIs) (left) and plot of IPIs
783 vs. normalized distance from the cell body (right; 0=closest to cell body, 1=distal tip of ALM)
784 for each of the punctate proteins shown in panel A. White circles denote mean, horizontal black
785 lines denote median and vertical thick black lines denote the interquartile range of the respective
786 distributions. Mean values are collected in Table S2. One-way ANOVA comparing the IPIs of
787 laminin, nidogen and MEC-4 showed a significant difference between the IPIs of the different
788 proteins [$F(3,11628) = 35.05$, $p = 1.52e\text{-}22$]. Tukey HSD post hoc analysis revealed that LAM-1
789 IPIs were not significantly different from those of LAM-2 ($p = 0.15$) or NID-1 ($p = 0.26$) and
790 that MEC-4 IPIs differed from all the ECM protein IPIs ($p = 0.001$).
791 **C.** Representative, *in vivo* live imaging of (top to bottom) MEC-4, LAM-2, NID-1, and SDN-1
792 puncta. Top two panels show puncta before and after bleaching, respectively; the bottom panel
793 shows kymographs (distance-time images) of a 10 s pre-bleach period and 300 s (5 minute)
794 observation period. See also Figure S2B-E.
795 **D.** Fluorescence recovery after photobleaching (FRAP) for MEC-4, LAM-2, NID-1, and SDN-1
796 puncta. Recovery was minimal for MEC-4, LAM-2, and NID-1 and substantial for SDN-1 during
797 the observation period. Dark traces show the average trajectory of fluorescence recovery; shaded
798 periods show the standard deviations for 23, 10, 11, and 8 neurons analyzed for MEC-4, LAM-2,
799 NID-1, and SDN-1, respectively. One-way ANOVA comparing the fractional fluorescence
800 recovery at 300 s showed a significant effect of the protein analyzed [$F(3,48) = 68.73$, $p = 2.15e\text{-}$
801 17). Tukey HSD post hoc analysis revealed that the fluorescence recovery of LAM-2::mNG were
802 not significantly different from those of NID-1::mNG ($p = 0.9$), while all other pairs were
803 significantly different from each other. See also Figure S2B-E.
804 **E.** Pairwise colocalization of NID-1, LAM-2, LAM-1, and MEC-4 tagged with wSc (magenta)

805 and mNG (green). Fluorescence micrographs show ALM neurites in double-labeled strains. The
806 dataset includes reference conditions for pairs expected to demonstrate high and low
807 colocalization: High: A single protein, NID-1, is tagged with two fluorophores (NID-1::wSc,
808 NID-1::mNG), or two subunits of an obligate heterotrimeric protein (LAM-1::wSc, LAM-
809 2::mNG); Low: Two TRN-expressed membrane with qualitatively distinct labeling — Uniform
810 (PAT-2::wSc) and punctate (MEC-4::mNG).
811 **F.** Intensity correlation quotient (ICQ) for protein pairs in panel E. Each circle (open circles:
812 high or low reference conditions, filled circles: test strains) represents a measurement from a
813 single ALM neurite in a dual-color strain. Black squares show the mean of the circles, and the
814 horizontal black bars show standard deviation. Except for the PAT-2::wSc; mNG::MEC-4 pair,
815 ICQ values computed from the same cell (circles) are significantly higher (Student's t-test, $p <$
816 0.05) than that measured from simulated pairs (box plots, showing the interquartile (box) and full
817 ranges (whiskers), excluding outliers). One-way ANOVA comparing the ICQ values across
818 genotypes, showed significant differences in ICQ among sets of real protein pairs
819 [$F(5,79) = 256.73$, $p = 2.52e-47$]. Horizontal dashed lines organize the strains into groups (top,
820 middle, bottom) within which ICQs are not significantly different by Tukey post hoc analysis.
821 Post hoc testing shows that ICQ values in both pairs in the top group differ from those for all
822 pairs in the middle group ($p = 0.001$) and the bottom group ($p = 0.001$). Similarly, ICQ values in
823 all pairs in the middle group differ from the pair in the bottom group ($p = 0.001$). Summary data
824 are collected in Table S2.
825

826 ***Figure 3. The TRN-associated extracellular matrix is essential to stabilize mechanosensory***
827 ***complexes in vivo and in vitro, but not for sequestering MEC-4 into RAB-3-positive vesicles.***
828 **A.** NID-1 puncta are absent in *mec-5*, *mec-1*, and *mec-9* null mutants. Representative fluorescent
829 micrographs of animals co-expressing NID-1::wSc and a cytoplasmic GFP marker in the *mec-*
830 *5(u444)*, *mec-1(e1738)* and *mec-9(u437)* mutant TRNs lack discrete NID-1 puncta in the ALM
831 but retain fluorescence in the adjoining body wall muscle (white arrows). See also Figure S3.
832 Scale bars are 10 µm.
833 **B.** NID-1::wSc fluorescence in BL around the pharynx and nerve ring are not affected in *mec-*
834 *5(u444)*, *mec-1(e1738)* and *mec-9(u437)* mutant animals. Scale bars are 10 µm.

835 **C.** Representative fluorescent micrographs of TRNs co-expressing mNG::MEC-4 and
836 mCherry::RAB-3 showing puncta co-localization. MEC-4 puncta are markedly reduced in
837 *mec-5(u444)*, *mec-1(e1738)* and *mec-9(u437)* mutant animals and in TRNs cultured *in vitro*
838 compared to control animals. Residual MEC-4 punctate structures often co-localize with RAB-3
839 (white arrows). Scale bars are 10 µm.
840 **D.** MEC-4 puncta are significantly reduced in *mec-5*, *mec-1* and *mec-9* null mutants compared to
841 control ALM neurons *in vivo* and dissociated, cultured TRNs *in vitro*. (Top) Plot showing the
842 density of all detected mNG::MEC-4 puncta (green) and vesicular mNG::MEC-4 puncta (defined
843 as puncta co-localizing with mCherry::RAB-3 puncta, white) in each cell. Pairs of data points
844 from individual cells are connected by green lines. Circles denote mean and thick vertical lines
845 show the standard deviation. One-way ANOVA shows significant differences in total MEC-4
846 puncta density [$F(3,80) = 426.44$, $p = 4.32e-49$] but no significant difference in the vesicular
847 MEC-4 puncta density [$F(3,80) = 1.77$, $p = 0.16$] between different groups. Tukey-HSD post hoc
848 analysis shows that total MEC-4 puncta density is significantly higher in control animals
849 compared to other groups. See also Figure S3F. (Bottom) Stacked bar plots representing the
850 fraction of MEC-4 in mechanosensory complexes (dark green), in RAB-3 positive vesicles
851 (medium green) and in the diffuse pool (light green) show that MEC-4 is mostly redistributed
852 from the mechanosensory complexes to the diffuse pool in the ECM mutants. One-way ANOVA
853 statistics of diffuse MEC-4 vs. genotype: F(3,80)=273.57, p=6.00e-42; One-way ANOVA
854 statistics of MEC-4 in mechanosensory complexes vs. genotype: F(3,80)=304.05, p=1.26e-43.
855 Tukey-HSD post hoc analyses show that control animals have significantly lower percentage of
856 MEC-4 in diffuse pool and significantly higher percentage of MEC-4 in mechanosensory
857 complexes compared to other groups) while the vesicle pool remains relatively unaffected (One-
858 way ANOVA statistics of vesicular MEC-4 vs. genotype: F(3,80)=2.87, p=0.04; Tukey-HSD
859 post hoc analysis shows no significant difference between all pairs except control and *mec-*
860 *1(e1738)*). The same dataset was used for analysis in both the top and bottom panels. For ALMs
861 *in vivo*, analysis was limited to the region 0-200 µm from the cell body due to a red co-injection
862 marker expressed in head neurons obscuring the mCherry::RAB-3 signal in TRNs. For TRNs
863 cultured *in vitro* the entire neurite was analyzed. Note: The MEC-4 distribution in TRNs cultured
864 *in vitro* was excluded from statistical analysis since the sample preparation, image acquisition
865 and analysis conditions were distinct. Summarized data are collected in Table S2.

866 **E.** Representative kymographs of MEC-4 puncta *in vivo* (left to right): control, *mec-1(e1738),*
867 and *mec-9(u437)*. Top two panels in each column show puncta before and after bleaching,
868 respectively; the bottom panel shows kymographs (distance-time images) of a 10 s pre-bleach
869 period and 300s (5 minute) observation period. Control data is replicated from Figure 2C,
870 mNG::MEC-4. Scale bars are 10 µm.
871 **F.** Fluorescence recovery after photobleaching (FRAP) for MEC-4::mNG in wild-type, *mec-*
872 *1(e1738),* and *mec-9(u437)*. Dark traces show the average trajectory of fluorescence recovery of
873 MEC-4 fluorescence; light traces show the results for individual trials for 23, 22, and 25 ALMs
874 in the indicated genotypes. Recovery is accelerated for diffuse MEC-4 fluorescence in *mec-*
875 *1(e1738)* and *mec-9(u437)* relative to discrete puncta in control. To facilitate comparisons,
876 control data is reprinted from Figure 2D, mNG::MEC-4. One-way ANOVA comparing the
877 maximum fractional fluorescence recovery at 300 s of mNG::MEC-4 in control, *mec-1(e1738)*
878 and *mec-9(u437)* animals showed a significant difference effect of genotype [$F(2,67) = 3.35$,
879 $p = 0.04$]. Tukey-HSD post hoc analysis revealed that the fluorescence recovery between control
880 and *mec-1(1738)* groups were significantly different, while there was no significant difference
881 between other pairs of groups. See also Figure S3G.
882

883 ***Figure 4*. ECM mechanosensory complexes can form in the absence of MEC-4 and**
884 ***TRN microtubules***
885 **A.** Representative images showing NID-1::wSc and LAM-2::mNG localize to discrete
886 puncta distributed along the ALM neurons in *mec-4(u253)* null background. Scale bars are 10
887 µm.
888 **B.** Probability density distributions plot of IPIs (top) and the individual IPIs (bottom) for
889 NID-1 and LAM-2 in *mec-4(u253)* animals. White circles denote mean, thin vertical lines denote
890 the median and thick horizontal lines denote the interquartile ranges of the population.
891 Summarized data are collected in Table S2.
892 **C.** Cumulative probability distribution of NID-1 and LAM-2 IPIs in *mec-4(u253)* animals
893 (green lines) compared to control animals (gray lines). The results of two-sample Kolmogorov-
894 Smirnov tests are indicated in each plot and suggest that control and mutant distributions differ
895 for NID-1 ($p < 0.001$, top), but not LAM-2 ($p = 0.219$, bottom). See also Figure S4A-C.
896 **D.** Representative images showing NID-1::wSc and mNG::MEC-4 puncta obtained from

897 dual-color transgenic animals in a *mec-7(ok2152)* β-tubulin mutant. Scale bars are 10 µm.
898 **E.** Probability density distributions plot of IPIs (top) and the individual IPIs (bottom) for
899 NID-1 (magenta) and MEC-4 (green) puncta in *mec-7(ok2152)* animals. White circles denote
900 mean, thin vertical lines denote the median and thick horizontal lines denote the interquartile
901 ranges of the population. Summarized data are collected in Table S2.
902 **F.** Cumulative distribution functions (CDF) of NID-1 and MEC-4 IPIs in *mec-7(ok2152)*
903 animals (magenta and green lines) compared to control animals (gray lines). The results of two-
904 sample Kolmogorov-Smirnov tests are indicated in each plot. See also Figure S4D-G.
905
906 ***Figure 5. Loss of lam-3 and nid-1, but not epi-1 decreases the density of mechanosensory***
907 ***complexes.***
908 **A.** Representative micrographs showing mNG::MEC-4 puncta distributed along the ALM
909 neurons in control and *epi-1(gm57)* L1 larvae, but disorganized or absent in *lam-3(ok2030)* L1
910 larvae. Scale bars are 10 µm. See Figure S5A for images of TRN attachment defects in
911 *epi-1(gm57)* adult animals.
912 **B.** Probability density distributions plot of IPIs (top) and the individual IPIs (bottom) for
913 mNG::MEC-4 in *epi-1(gm57)* and *lam-3(ok2030)* L1 larva animals. Due to the disrupted or lack
914 of MEC-4::mNG signal in many *lam-3(ok2030)* L1 larva animals, IPIs could be computed for
915 only 17 out of 34 images collected. White circles denote mean, thin vertical lines denote the
916 median and thick horizontal lines denote the interquartile ranges of the population. Summarized
917 data are collected in Table S2.
918 **C.** Cumulative distribution functions (CDFs) for mNG::MEC-4 IPIs in *epi-1(gm57)* and
919 *lam-3(ok2030)* (green lines) L1 larvae compared to control L1 larvae (gray lines). The results of
920 two-sample Kolmogorov-Smirnov tests are indicated in each plot.
921 **D.** Representative images of mNG::MEC-4 and LAM-1::wSc obtained from dual-color
922 transgenic animals in a *nid-1* mutant background showing dim and sparse puncta in both
923 channels. Scale bars are 10 µm.
924 **E.** Probability density distributions plot of IPIs (top) and the individual IPIs (bottom) for
925 mNG::MEC-4 (green) and LAM-1::wSc (magenta) in *nid-1(cg119)* mutant animals. White
926 circles denote mean, thin vertical lines denote the median and thick horizontal lines denote the
927 interquartile ranges of the population. Summarized data are collected in Table S2.

928 **F.** Cumulative distribution functions (CDFs) of MEC-4 (top) and LAM-1 (bottom) IPIs in ALM
929 neurites. Larger intervals dominate the distribution in *nid-1* mutants (magenta and green)
930 compared to control (gray). The results of two-sample Kolmogorov-Smirnov tests comparing
931 CDFs are indicated in each plot.
932 **G.** Intensity line scans derived from images in panel D showing the spatial coincidence of peak
933 intensities in each channel. See also Figure S5D-G.
934 **H-J.** *nid-1* loss of function decreases behavioral and neural responses to touch. (H) Touch
935 response as a function of genotype, using wild-type (gray) and *mec-4(u253)* (blue) null animals
936 as references show very small touch defects in *nid-1(cg119)* (teal) animals but severe touch
937 defects in *mec-5(u444)* (magenta) animals. For each genotype, strains with or without the TRN
938 marker *uIs31* are represented by light and dark colors respectively. Bars are the average (± SEM)
939 response to 10 touches of *n=75* animals tested blind to genotype in 3 independent cohorts. 2-way
940 ANOVA shows significant differences in touch-response between genotypes [$F(3,594)=1135.12$,
941 p=1.9e-245] as well as presence or absence of the *uIs31* reporter [$F(1,594)=6.59$, p=1.05e-02].
942 Tukey-HSD post hoc analysis shows significant differences between all mutant genotypes
943 compared to control (gray bars). Summarized data are collected in Table S2. (I)
944 Mechanoreceptor currents (MRCs) evoked by indentation pulses of the indicated amplitude.
945 Traces for control (dark gray), *nid-1(cg119)* (green) and *mec-5(u444)* (magenta) mutants are
946 shown for a small (1 µm), medium (5 µm) or large (11 µm) indentations. Similar results obtained
947 in 11, 6 and 2 recordings for control, *nid-1* and *mec-5* animals, respectively. (J) Peak MRC
948 amplitude at the onset of stimulation as a function of stimulus displacement. Dark thick lines are
949 the average of the lighter thin lines for control (dark gray), *nid-1(cg119)* (green) and *mec-*
950 *5(u444)* (magenta) animals. One-way ANOVA shows significant differences in the peak current
951 amplitude at 11 µm indentation between genotypes ($F(2,16)=19.39$, p=5.3e-05). Tukey-HSD
952 post hoc analysis shows significant differences between all groups. See also Figure S5H-I.
953

954 ***Figure 6. NID-1 G3 domain, but not its binding to LAM-2 or LAM-3 EGF domains is***
955 ***necessary for MEC-4 puncta distribution.***
956 **A.** (Left) Schematic diagram of NID-1, LAM-2 and LAM-3 proteins mapping the ΔG1-G2
957 (*cg118)* and ΔG3 (*pg146)* in-frame deletions in NID-1 and the point mutations in the 8th EGF
958 domains of LAM-2 (*pg153*) and LAM-3 (*pg169*). Large boxes show the indicated globular

959 domains. Small gray boxes show EGF domains. (Right) Homology model of *C. elegans* NID-1
960 G3 domain bound to LAM-2 EGF8, based on crystal structure of mouse nidogen G3 domain
961 bound to mouse laminin-γ1 (PDB ID: 1NPE).
962 **B.** Sequence of the LAM-2 and LAM-3 EGF8 domains predicted to bind NID-1, and its
963 sequence alignment with its counterpart in mouse laminin-γ1. The residues mutated in the *pg153*
964 LAM-2[NSS] and *pg169* LAM-3[NSS] alleles are highlighted in pink.
965 **C**. Representative images of mNG::MEC-4 puncta present in *nid-1* mutant ALM neurons (top to
966 bottom): NID-1[ΔG1-G2] (*cg118*), NID-1[ΔG3] (*pg146*), and LAM-2[NSS];LAM-3[NSS]
967 (*pg153;pg169*). Anterior is to the left; scale bars are 10 µm. See also Figure S6.
968 **D.** Probability density distribution plots of IPIs (top) and the individual IPIs (bottom) for
969 mNG::MEC-4 (green) in NID-1[ΔG1-G2], NID-1[ΔG3], and LAM-2[NSS];LAM-3[NSS]
970 mutant animals. White circles denote mean, thin vertical lines denote the median and thick
971 horizontal lines denote the interquartile ranges of the population. Summarized data are collected
972 in Table S2.
973 **E.** Cumulative distribution functions (CDFs) of mNG::MEC-4 IPIs in the indicated alleles
974 (green) vs control worms (gray, replotted from Figure 2B). The results of two-sample
975 Kolmogorov-Smirnov tests are indicated in each plot.
976

977 ***Figure 7. Disrupting Ku15 in MEC-1 causes misassembly of mechanosensory complexes and***
978 ***touch-insensitivity.***
979 **A.** Schematic diagram of the longest MEC-1 isoform showing fifteen predicted Kunitz domains
980 (red) and EGF repeats (gray).
981 **B.** Amino acid sequence of MEC-1 Ku15 compared to that of MitTx, a Kunitz domain-
982 containing ion channel toxin (Baconguis et al., 2014) (left) and a homology model (right) of
983 MEC-1 Ku15 based on MitTx structures (PDB ID: 4NTX). Conserved amino acids are
984 highlighted in orange. Asterisks denote the two mutated residues in MEC-1 Ku15, R1804 and
985 C1808.
986 **C.** Mechanosensory complexes visualized in dual-color transgenic animals expressing
987 mNG::MEC-4 and NID-1::wSc in *mec-1* missense alleles affecting Ku15. Anterior is to the left,
988 scale bar is 10µm. Boxed area in the MEC-1[C1808Y] image is enlarged in Panel F to show
989 closely spaced NID-1::wSc puncta.

990 **D**. Probability density distribution plots of IPIs (top) and the individual IPIs (bottom) for
991 NID-1::wSc puncta in MEC-1[R1804C] (*e1526*) and MEC-1[C1808Y] (*pg164*) mutant animals.
992 White circles denote mean, thin vertical lines denote the median and thick horizontal lines denote
993 the interquartile ranges of the population. Summarized data are collected in Table S2.
994 **E**. Cumulative distribution function (CDFs) of NID-1::wSc IPIs in the indicated *mec-1* alleles
995 (magenta) vs control worms (gray). The results of two-sample Kolmogorov-Smirnov tests are
996 indicated in each plot. See also Figure S7.
997 **F.** Magnified view of the boxed area in C, showing NID-1 puncta and uniform MEC-4
998 fluorescence in a MEC-1[C1808Y] (*pg164*) mutant animal.
999 **G.** MEC-4 distribution as a function of genotype for *mec-1* missense alleles. Stacked bars show
1000 the average relative fractions of mNG::MEC-4 fluorescence in the punctate (dark green) and
1001 diffuse (light green) pools. For each genotype, we analyzed 14, 19, and 13 independent
1002 replicates. One-way ANOVA shows significant differences in the MEC-4 diffuse fraction
1003 between genotypes [$F(2,43) = 394.73$, $p = 2.15e-28$]. Tukey-HSD post hoc analysis shows
1004 significant differences between all groups. Summarized data are collected in Table S2.
1005 **H.** Plot of ICQ values calculating MEC-4 and NID-1 colocalization as a function of genotype.
1006 Each circle (open circles: control data replicated from Figure 2F, filled circles: *mec-1* mutants)
1007 shows a measurement from a single ALM neurite. Black squares show the mean of the filled
1008 circles or open circles respectively, and the black bars show standard deviation. For every
1009 genotype except MEC-1[C1808Y], the ICQ of two fluorescence channels from the same cell
1010 (circles) are significantly higher (Student's t-test, $p<0.05$) than that measured for simulated pairs
1011 (boxplots, showing the interquartile (box) and full ranges (whiskers), excluding outliers). One-
1012 way ANOVA shows significant differences in ICQ between genotypes [$F(2,43) = 390.04$,
1013 $p = 2.74e-28$]. Tukey-HSD post hoc analysis shows significant differences between control and
1014 both *mec-1* mutants but not between *mec-1(e1526)* and *mec-1(pg164)*. Summary data are in
1015 Table S2.
1016 **I.** Touch sensitivity as a function of genotype, assessed in a 10-touch assay. Bars represent the
1017 average (±SEM) of 75 animals tested in 3 independent cohorts blinded to genotype. One-way
1018 ANOVA shows significant differences between genotypes [$F(2,222) = 280.68$, $p = 1.64e-61$].
1019 Tukey-HSD post hoc analysis shows significant differences between control and both *mec-1*
1020 mutants but not between *mec-1(e1526)* and *mec-1(pg164)*. Summary data are in Table S2.

1021 **J.** Proposed model of the relationship between MeT channels and ECM beam structures. (i)
1022 Schematic diagram of a TRN (yellow) embedded within the epidermis (blue), showing ECM
1023 puncta (red) as seen in fluorescence micrographs of NID-1, LAM-2 and LAM-2. Indentation is
1024 applied on the worm by a small bead (black) (ii) Expanded view of the indented region showing
1025 strain on the neurite (black arrows) and displacement of ECM beams (red). (iii) Schematic
1026 representation of a cross section of a TRN (yellow) and surrounding ECM (transparent gray)
1027 showing ECM beams (dark pink). (iv) Expanded view of the boxed area in (iii) showing spatial
1028 arrangement of the different proteins discussed in this manuscript. The EPI-1/LAM-1/LAM-2
1029 laminin is shown as a loose hexagonal lattice filling most of the space between the epidermis
1030 (blue) and TRN (yellow). The LAM-3/LAM-1/LAM-2 laminin is shown as a tight and highly
1031 structured hexagonal lattice within the ECM beams (pink). NID-1 (purple circles) is also present
1032 in the ECM beam region. MEC-1 (cyan) connects the ECM beams to the MEC-4 channels
1033 (green) embedded in the TRN plasma membrane.

1034 **STAR Methods**

1035

1036 RESOURCE AVAILABILITY

1037 *Lead contact*

1038 Further information and requests for resources and reagents should be directed to and will be
1039 fulfilled by the lead contact, Miriam B. Goodman (mbgoodmn@stanford.edu).

1040 *Material availability*

1041 *C. elegans* strains newly generated for this paper are available from the lead contact upon
1042 request. Interested parties should submit requests to the lead contact indicating the strain and
1043 genotype of each of the required *C. elegans* strains.

1044 *Data and code availability*

1045 This paper did not generate new data conforming to standardized data types, including nucleotide
1046 sequences, proteomics, metabolomics, or structures of biological macromolecules. This paper did
1047 generate new *C. elegans* genotype-phenotype relationships, fluorescence images,
1048 electrophysiological recordings, and behavior testing results.

1049 - Genotypic and phenotypic information about new *C. elegans* alleles created in this study
1050 will be deposited to www.wormbase.org.
1051 - All original code has been deposited at GitHub and is publicly available as of the date of
1052 publication. DOIs are listed in the key resources table.

1053

1054 EXPERIMENTAL MODEL AND SUBJECT DETAILS

1055 *C. elegans*

1056 This study uses wild-type, mutant and transgenic *C. elegans* nematodes. Only
1057 hermaphrodites were analyzed in this study, although males were used to perform genetic
1058 crosses. A complete list of all *C. elegans* strains used in this study with their genotypes and
1059 provenance is available in the Key Resources Table. The list includes transgenic and mutant
1060 lines generated specifically for this study, obtained from prior work, or from the Caenorhabditis

1061 Genetic Center. Animals were maintained at 20°C on NGM agar plates seeded with *E. coli*
1062 OP50, unless otherwise mentioned.

1063 All animals studied by light microscopy, tested in behavioral assays, or subjected to *in*
1064 *vivo* electrophysiology were age-synchronized adopting standard methods (Stiernagle, 2006). In
1065 brief, we harvested gravid adults in ~1 mL of water and obtained eggs from these animals by
1066 treating them with household bleach (100µL) and KOH (20µL, 5M solution). Eggs were
1067 transferred to NGM agar plates seeded with bacterial food and allowed to grow into young adults
1068 (~3 days at 20°C).

1069 *Primary cells (nematodes)*

1070 As detailed below, we generated cultures of primary cells from transgenic *C. elegans*
1071 nematodes expressing fluorescent proteins. Cells were plated on coverslips coated uniformly by
1072 peanut lectin or bearing thin stripes of peanut lectin fabricated in-house as described below
1073 (protein patterning coverslips) and maintained in a benchtop chamber at room atmosphere and
1074 temperature (22-24°C) for 1-7 days.

1075

1076 METHOD DETAILS

1077 *Gene editing via CRISPR/Cas9 techniques*

1078 Tagging endogenous proteins

1079 Unless indicated otherwise, we relied on homologous recombination via the self-excising
1080 cassette (SEC) method (Dickinson et al., 2015) to insert fluorescent protein-encoding DNA at
1081 four endogenous loci: *lam-1, lam-3, epi-1* and *nid-1*. We created a template repair plasmid
1082 (mg682) with wormScarlet (wSc) based on the SEC repair plasmid designs described in
1083 Dickinson et al., 2015. We cloned in left and right homology arms corresponding to the insertion
1084 sites at the *lam-1, lam-3, epi-1* or *nid-1* loci into this template plasmid by Gibson assembly.
1085 Repair plasmids and small-guide RNA (sgRNA) targets were designed based on data curated by
1086 WormBase (Davis et al., 2022). To generate each strain, we injected a plasmid mixture into the
1087 gonads of 40-60 young adult animals. The mixture contained plasmids encoding the following
1088 elements: Cas9-sgRNA (50 ng/µL), repair template (50 ng/µL), visible markers [pCFJ104

1089 (myo-3p::mCherry), 5 ng/µL; pCFJ90 (myo-2p::mCherry), 2.5 ng/µL]. Each injected animal was
1090 allowed to lay eggs for 2-3 days at 25°C, in the absence of selection. To select for progeny
1091 carrying edits, we added hygromycin (500 µL, 5 mg/mL) to each plate and allowed animals to
1092 grow at 25°C for an additional 4-5 days. Candidate transgenic animals survived hygromycin
1093 treatment, lacked red fluorescent extrachromosomal array markers, and displayed a Rol
1094 phenotype conferred by the insertion of the SEC carrying the *sqt-1(e1350)* mutation (Dickinson
1095 et al., 2015). To remove the SEC, we heat-shocked plates containing ~6 L4 rollers (37°C, 75
1096 minutes) and allowed the resulting progeny to grow at 20°C for 3-4 days. Single, adult NonRol
1097 animals (worms that lost both copies of the SEC) were transferred to growth plates and allowed
1098 to generate progeny. These candidate transgenic animals were evaluated by visualizing
1099 fluorescence, PCR genotyping, and sequencing. Homozygous wSc-tagged *lam-1* animals were
1100 sterile and exhibited several morphological defects, similar to those previously reported for a
1101 mNeonGreen(mNG)-tagged *lam-1* (Keeley et al., 2020). Consequently, we maintained and
1102 imaged these animals as viable heterozygotes.

1103 We used a slightly modified approach from above for creating the PAT-2::wSc strain. In
1104 this approach we used a template repair plasmid in which the Lox2272-site flanked selection
1105 cassette contained the Hygromycin resistance gene, but lacked the *sqt-1(e1350)* reporter and the
1106 heat-shock inducible Cre genes (mg546). The repair plasmid was designed such that presence of
1107 the selection cassette will prevent translational fusion of the wSc tag at the PAT-2 C-terminus.
1108 After confirming insertion of the wSc tag and the selection cassette at the *pat-2* locus by PCR,
1109 we injected the worms with a plasmid encoding *eft-3* promoter driven Cre, alongwith a co-
1110 injection marker (pCFJ90 (myo-2p::mCherry), 2.5 ng/µL). We then screened for the loss of the
1111 selection cassette among the progeny of the injected worms, by looking for expression of wSc
1112 tagged PAT-2 in all body wall muscle cells as well as a loss of the *myo-2p*::mCherry red pharynx
1113 marker.

1114 Mutating endogenous gene loci

1115 To generate *C. elegans* strains carrying genetic deletions or point mutations in *nid-1*, *lam-*
1116 *2* or *mec-1* loci, we applied the co-CRISPR method (Arribere et al., 2014; Paix et al., 2015),
1117 using *dpy-10(cn64)* as the co-CRISPR target. This work relied on genetic and genomic data
1118 curated and maintained by WormBase (Davis et al., 2022). All reagents for this purpose were

1119 purchased from IDT Technologies: Cas9 protein (Alt-R® S.p. Cas9 Nuclease V3, 100 µg,
1120 Catalog # 1081058), tracrRNA (Alt-R® CRISPR-Cas9 tracrRNA, 5 nmol, Catalog # 1072532),
1121 crRNA for each loci (Alt-R® CRISPR-Cas9 crRNA, 2 nmol), single stranded oligomeric DNA
1122 repair templates (Ultramer™ DNA Oligonucleotides). We prepared injection mixes with
1123 equimolar amounts of tracrRNA, crRNA and Cas9 nuclease, such that the final concentration of
1124 each was 1.5 µM. If multiple crRNAs were used for a single target site, the amounts were
1125 adjusted such that the total crRNA concentration was 1.5 µM. The *dpy-10* crRNA was used at a
1126 ratio 1:14 to the target crRNAs. In the first step, we allowed the tracrRNA and crRNAs to anneal
1127 at 95°C for 5 min, followed by incubation at room temperature for 5 min. Next, we added the
1128 annealed RNA mixture to Cas9 and incubated this solution at 37 °C for 10 min. Finally, ssDNA
1129 repair template was added to generate a final concentration of 0.5 µM and the total volume was
1130 adjusted to 20 µL using sterile water. For each gene editing round, we injected 15-20 young
1131 adult animals and transferred individual animals to growth plates for 3-4 days at room
1132 temperature. Plates that contained many Rol progeny as evidence of successful editing were
1133 selected for further analysis. Specifically, we isolated single Rol animals and allowed them to lay
1134 eggs for 2 days (room temperature), after which the roller animals were screened for the desired
1135 mutation using PCR. Non-roller progeny animals from the positive plates were then isolated and
1136 screened in the same way. The target loci were sequenced in candidate lines to confirm the
1137 presence of the desired mutation and validate the gene-edited line.

1138 Primary nematode cell culture

1139 We generated cultures of mixed embryonic *C. elegans* cells following previous methods
1140 (Bianchi and Driscoll, 2006; Sangaletti and Bianchi, 2013; Strange et al., 2007) and introduced
1141 modifications that improved yield. In brief, the procedure involves treating suspensions of
1142 isolated embryos with chitinase to soften the egg shell, mechanical trituration and filtration to
1143 dissociate cells and remove debris, followed by plating onto treated glass coverslips and
1144 culturing at room temperature and atmosphere for 1-7 days.

1145 To improve yield, we first sought to improve age-synchronization and to increase the
1146 number of embryos available for cell isolation. In particular, we grew animals in three cycles on
1147 10-cm plates. During the first cycle, we used standard hypochlorite bleaching methods (6%
1148 bleach, 150 mM NaOH: Stiernagle, 2006) to harvest embryos from animals grown on standard

1149 NGM plates seeded with OP50 *E. coli.* These embryos were transferred to 10-cm enriched
1150 peptone plates seeded with NA22 *E. coli* and allowed to grow into gravid adults. This process
1151 was repeated for two additional cycles. Following these steps, we harvested embryos after
1152 separating gravid adults from bacteria through several centrifugation and washing cycles and
1153 sodium hypochlorite treatment to harvest embryos. The resulting embryos were rinsed three
1154 times with 1x egg buffer (25 mM HEPES, 118 mM NaCl, 48 mM KCl, 2 mM $CaCl_2$, 2 mM
1155 $MgCl_2$, adjusted to a pH of 7.3 with NaOH). For quality control purposes, we measured the
1156 osmolality of the egg buffer with a freezing-point depression osmometer (AdvancedInstruments)
1157 and used batches that had an osmolality of 340 ± 5 mOsm.

1158 Next, we separated eggs from lytic fragments of older worms by resuspending the pellet
1159 in a sucrose solution (60% w/v sucrose in deionized water) and centrifugation at 350g for 5
1160 minutes. Following these steps, we incubated embryos in chitinase (25 U/mL) while rocking
1161 until ~80% of eggshells had been digested (~50 min), an endpoint that we confirmed visually.
1162 Finally, we rinsed dissociated embryos and dissociated them mechanically by trituration first
1163 through a sterile 21-gauge needle and then through a sterile 25-gauge needle. We used a 5-µm
1164 filter to remove debris from the resulting cell suspension, rinsed and resuspended the cell
1165 suspension in sterile L-15 cell culture media without HEPES or phenol red (Gibco™, Catalog#
1166 21083027), and seeded the cells onto glass coverslips either coated uniformly with peanut lectin
1167 or bearing micropatterns of peanut lectin. These procedures were performed on a standard
1168 benchtop using aseptic technique.

1169 Protein micropatterning glass coverslips

1170 To generate thin stripes of adhesive proteins, which constrained the shape of *C. elegans*
1171 neurons in culture, we used a light-activated molecular adsorption technique and a commercial
1172 instrument (Primo, Alvéole USA, Fairfax, VA, USA) to generate protein micropatterns on glass
1173 coverslips. We used open-source graphic design software (Inkscape) to design custom patterns
1174 consisting of thin (8-pixels or 2.2 µm) stripes on 1824x1140 pixel canvas size. Stripe width and
1175 spacing was optimized to enable touch receptor neurons to elaborate straight neurites that were
1176 confined to lateral strips and did not traverse areas lacking peanut lectin (PNA), as described
1177 (Franco, 2021). We used both unlabelled peanut lectin and Alexa Fluor™ 594-conjugated lectin
1178 PNA.

1179 We adapted a protein micropatterning approach (Strale et al., 2016), as follows. For
1180 convenience and simplicity, we used glass-bottom six-well tissue culture-grade microtiter plates
1181 (6 Micro-well glass bottom plate with 20 mm micro-well #1.5 cover glass, Cellvis ™, Catalog#
1182 P06-20-1.5-N) for cell culture experiments involving patterned coverslips. First, we plasma-
1183 treated the plates with ionized atmospheric gas for 1 minute (25 forward, zero reflected power,
1184 Plasmatech P-50). Next, we positioned a PDMS reagent basin in each well, added poly-l-lysine
1185 or PLL (0.01% in sterile PBS, ~35 µl) to each well, and allowed the PLL solution to incubate for
1186 1 hour. Following this step, we added mPEG-SVA (100 µg/mL, Laysan Bio Inc.) freshly
1187 prepared in pH-adjusted 100 mM HEPES, pH 8.0 buffer and incubated the coverslips for an
1188 additional 1 hour. We fabricated reagent basins from PDMS sheets in-house using a consumer-
1189 grade, computerized die-cutting machine (Silhouette, Cameo, Lindon, Utah, USA). Lastly, we
1190 rinsed the coverslips with distilled water and allowed them to air dry prior to the application of
1191 proprietary photoactivatable reagent, PLPP gel (Alvéole, diluted in pure ethanol at 1:6
1192 volumetric ratio).

1193 We allowed coverslips to air dry prior to patterning with the Primo instrument (25 ms
1194 exposure, 100% laser power, 50 mJ/mm^2 dosage), which uses light to degrade the PLPP gel
1195 according to the user-defined pattern. We transferred peanut lectin protein (PNA) to patterned
1196 coverslips in two incubation steps: 1) PBS for >5 minutes; 2) PNA (500 µg/mL) for 20 minutes.
1197 which enabled us to visualize the patterns. We fabricated patterns one day prior to plating
1198 dissociated embryonic *C. elegans* cells and kept them hydrated with sterile PBS until use.

1199 *C. elegans* touch assay

1200 We measured touch responses using a ten-touch assay (Chalfie et al., 2014; Vasquez et
1201 al., 2014). Specifically, we delivered mechanical stimuli to age-synchronized, well-fed young
1202 adult animals with an eyebrow hair glued to a toothpick touching animals alternately in anterior
1203 and posterior regions of the body for a total of 10 times. Animals were scored as responding if
1204 they reversed direction following each stimulation. This method delivers supra-threshold stimuli,
1205 independent of experimenter or the specific eye-brow hair used (Nekimken et al., 2017). We
1206 analyzed touch sensitivity of groups of 4-5 strains and used wild-type (N2) and TU253 *mec-*
1207 *4(u253)* null mutants as touch-sensitive and touch-insensitive (Mec) references, respectively.
1208 Animals were tested blind to genotype in cohorts of 25 animals. At least three independent

1209 cohorts were tested for each genotype or condition. For strains containing *lam-1(pg136)* allele
1210 (LAM-1::wSc), we picked ca. 50 heterozygous animals (identified by dimmer red fluorescence,
1211 normal locomotion and body morphology compared to homozygous *lam-1(pg136)* animals
1212 which were sluggish, dumpy and/or had severely malformed internal organs) to fresh plates a
1213 few hours prior to touch testing.

1214 Whole-cell patch clamp electrophysiology

1215 We recorded from the ALM neurons in TU2769 *uIs31 [mec-17p::GFP]* and GN932
1216 *uIs31; nid-1(cg119)* lines, following established procedures (Eastwood et al., 2015; Katta et al.,
1217 2019; O'Hagan et al., 2005). As a consequence of geometric constraints imposed by our
1218 stimulator system, most of our recordings are from the ALMR neuron. The ALMR and ALML
1219 neurons are bilaterally symmetric and exhibit no detectable differences in voltage- or touch-
1220 evoked currents (this study and Eastwood et al., 2015; Katta et al., 2019; O'Hagan et al., 2005).
1221 We used the following salines in all recordings. Extracellular saline contained (in mM): NaCl
1222 (145), KCl (5), $MgCl_2$ (5), $CaCl_2$ (1), and Na-HEPES (10), adjusted to a pH of 7.2 with NaOH.
1223 We added D-glucose (final concentration of 20mM) to external saline, bringing the osmolarity to
1224 ~325 mOsm. Intracellular recording solution contained (in mM): K-gluconate (125), KCl (18),
1225 NaCl (4), $MgCl_2$ (1), $CaCl_2$ (0.6), K-HEPES (10), and K_2EGTA (10), and adjusted to a pH of 7.2
1226 with KOH. We added a fluorescent dye, sulforhodamine 101 (1mM, Invitrogen), to the
1227 intracellular solution in order visually confirm whether or not the whole-cell configuration was
1228 achieved in each recording. We used an EPC-10 USB amplifier controlled by Patchmaster
1229 software (version 2x90; HEKA/Harvard Biosciences) to record membrane current, deliver
1230 voltage-clamp stimuli, and to control the mechanical stimulator. Mechanical stimuli were
1231 delivered using an open-loop system adapted from (Peng and Ricci, 2016) and described
1232 previously (Katta et al, 2019). Analog data (membrane potential, membrane current) were
1233 filtered at 2.9 kHz and digitized at 5 kHz.

1234 Voltage-activated currents were measured in response to 100ms pulses between -80 and
1235 80mV (in 20mV increments) from a holding potential of -60mV. We applied each voltage
1236 protocol in triplicate and averaged the resulting membrane current traces to improve the signal to
1237 noise, as described (Goodman et al., 1998). Membrane voltage was corrected for errors due to
1238 liquid-junction potentials (-14 mV) and residual series resistance measured in each recording.

1239 We omitted recordings with series resistance larger than 200 MΩ and holding current more than
1240 -10 pA at -60 mV. MRCs were evoked by indentation steps (300 ms) with an interstimulus
1241 interval of 1s from a holding potential of -60mV, as described by Katta et al., 2019. We applied 3
1242 repetitions of mechanical stimuli and averaged the resulting MRC traces. We used peak-finding
1243 software to measure peak MRC currents at the onset and offset of the mechanical stimulation
1244 pulse. For clarity, only the 'on' MRCs are shown in this study.

1245 Protein structure homology modeling

1246 We generated a homology models for the NID-1[G3]-LAM-2[EGF8] complex and
1247 MEC-1[Ku15] using the Phyre2 protein fold recognition server (Protein Homology/analogY
1248 Recognition Engine V 2.0) (Mezulis et al., 2015). For the NID-1[G3]-LAM-2[EGF8] complex
1249 model, we used the crystal structure of mouse nidogen bound to laminin-γ (PDB ID: 1NPE;
1250 Takagi et al., 2003). For the MEC-1[Ku15] model, we used the structure of the neurotoxin
1251 MitTx-alpha bound to the chicken ASIC1 ion channel (PDB ID: 4NTX; Baconguis et al., 2014).
1252 Both models were rendered for publication using the The PyMOL Molecular Graphics System,
1253 Version 2.5.1 Schrödinger, LLC.

1254 Transmission electron microscopy

1255 We relied on multiple, independent serial-section TEM (ssTEM) datasets to investigate
1256 the ultrastructure of ECM structures associated with the TRNs in wild-type animals. In all cases,
1257 animals were prepared for TEM by high-pressure freezing followed by freeze substitution with
1258 chemical fixatives and embedded in plastic resin. The image series of ALM and AVM neurons
1259 shown in Figures 1E and Figure S1A-B and E(left) is derived from a wild-type (N2), L3 stage
1260 larva, while those of PLM and PVM neurons shown in Figures S1C-D and E(right) is from a
1261 wild-type (N2), L4 stage larva. We estimated ECM beam dimensions and distance from the TRN
1262 plasma membrane and basal membrane of epidermal cells from ssTEM images of ALM neurons
1263 prepared in young adult worms, prepared for a prior publication (Kreig et al., 2017). Despite
1264 variations in sample preparation, life stage, embedding resins, sample preparation and
1265 microscope instrumentation, ECM beam structures have similar appearances and structures in all
1266 ssTEM datasets we have examined.

1267 For L3 larval worms, we relied on high pressure freezing followed by freeze substitution,
1268 as previously described (Mulcahy et al., 2018; Witvliet et al., 2021). Briefly, mixed-stage wild-

type (N2) animals were collected into 3 mm high pressure freezing carriers with 100 µm wells (Leica, product #16770141), using OP50 *E. coli* as a filler. A flat lid (Leica, product #16770142) was placed on top and the sandwich was high pressure frozen using a Leica EM ICE (product #16771801). Freeze substitution was accomplished by ramping the sample from -90 to -60°C over 20 hours in 0.1% tannic acid and 0.5% glutaraldehyde, followed by washing 4 times with acetone over 3 hours, exchanging with 2% OsO_4 and ramping the temperature to -20°C over 8 hours, holding at -20°C for 11 hours, ramping the temperature to 0°C over 4 hours and washing 4 times with acetone over 1 hour. We then infiltrated the sample with Spurr-Quetol resin, embedding single animals, and cured the samples (60°C, 24 hours). The age of this sample was determined by the lineage of neuronal and non-neuronal cells in the volume (Witvliet et al., 2021). We collected 50 nm serial sections on 2x0.5 mm slot grids using a Leica UC7 ultramicrotome and 35° diamond knife (Diatome). Sections were post-stained with 2% aqueous uranyl acetate and 0.1% Reynold's lead citrate, and imaged at 0.768 nm/pixel X-Y resolution using a Technai T20 TEM at 120kV equipped with a digital camera (Gatan Orius). We aligned and down-sampled 212 and 427 serial TEM micrographs to 3.072 nm/pixel resolution, estimated to cover 10.6 µm (ALML), 10.6 µm (ALMR), and 21.53 µm (AVM) processes.

For L4 larval worms, samples were high-pressure frozen in M9 media containing 20% BSA and E. coli in specimen carriers with a 50 µm deep well (Cat. no. 390, TechnoTrade International, Inc.). These specimen carriers were covered with the flat side of a Type B specimen carrier (Cat. no. 242, Technotrade International Inc.) and frozen with a BalTec HPM01 high pressure freezer (Liechtenstein). Freeze-substitution was carried out with a Leica AFS2 unit in acetone containing 1% OsO_4, 0.1% uranyl acetate, 1% methanol, and 3% water (Walther and Ziegler, 2002). Samples were held at -90°C for 16 hours, ramped to -60°C in 6 hours, held at -60°C for 6 hours, ramped to -25°C in 7 hrs, held at -25°C for 6 hours, and finally ramped to 0°C over 5 hours. At the completion of substitution, we rinsed samples in acetone, infiltrated and then polymerized in Eponate 12 resin (Ted Pella, Inc.). We cut serial 50 nm cross-sections with a Leica UCT ultramicrotome using a Diatome diamond knife, picked up the sections on Pioloform-coated slot grids and stained with uranyl acetate and Sato's lead (Sato, 1968). We imaged the sections with an FEI Tecnai T12 TEM at 120 kV equipped with a Gatan U895 4k x 4k camera (Gatan, Pleasonton, CA) at a pixel resolution of 1.01 nm/pixel using SerialEM (Mastronarde, 2005).

1300 *Light microscopy*

1301 *C. elegans* animal mounting for imaging

1302 To visualize and analyze MEC-4 and protein constitutions of the basal lamina in living
1303 animals, we generated sets of still and time-lapse images. We imaged *C. elegans* animals
1304 mounted on agarose pads (5% wt/vol) on glass slides. In brief, we used levamisole (5mM in M9
1305 buffer) to immobilize age-synchronized young adult animals or L1 larvae. We mounted young
1306 adult animals on grooved agar pads fabricated by casting the pads on the surface of a standard
1307 LP record (Rivera Gomez and Schvarzstein, 2018). This approach generates worm-sized grooves
1308 and constrains animals to a straight posture within the grooves, enabling us to image dozens of
1309 animals in a single imaging session. This approach was not appropriate for L1 larvae, however,
1310 due to their narrower bodies. Instead, we collected synchronized L1s in M9 buffer, treated them
1311 with levamisole for ~10 minutes until most animals assumed a straight posture, concentrated the
1312 animals by centrifugation, and transferred 2 µL of concentrated L1s to surface of a smooth
1313 agarose pad bearing a small droplet of levamisole (5mM in M9). To keep the samples moist
1314 during each imaging session, we covered all mounted animals with a glass cover slip and sealed
1315 the coverslip with VALAP (1:1:1 Vaseline:Lanolin:Paraffin).

1316 Wide-field and confocal fluorescence microscopy (still images)

1317 We generated wide-field fluorescence images of the ALM neurites and associated basal
1318 lamina (BL) structures using an automated inverted compound microscope equipped for
1319 epifluorescence imaging (Keyence BZ-X800). Using the instrument's stitch and align function,
1320 we first collected a low magnification image (4X) and selected individual animals to image at
1321 high magnification (60X, Nikon Plan Apo lambda, oil immersion, NA=1.40). In most cases, we
1322 used the stitch and align function to generate complete images of the ALM neurite. For all
1323 experiments (except those using strains expressing mCherry::RAB-3) designed to compare
1324 puncta distribution or fluorescence intensity across genotypes, we kept the following image
1325 acquisition parameters constant: exposure time (mNG::MEC-4 = 1 s, LAM-1::wSc = 0.2 s,
1326 LAM-2::mNG = 1.2 s, NID-1::wSc = 0.133 s), binning (1x1), camera gain settings (+6dB). We
1327 acquired images of strains expressing the synaptic vesicle marker, mCherry::RAB-3 using 2x2
1328 binning, and the following exposure times: mNG::MEC-4 = 0.2 s, mCherry::RAB-3 = 0.1 s. For
1329 imaging the movement of MEC-4 in vesicles over time (Figure S3C,S3E), we used time-lapse

1330 software to collect dual-color time-lapse image stacks using Keyence BZ-X800 and Nikon Plan
1331 Apo lambda 60x objective, using the following acquisition parameters: 3x3 binning, 1 frame
1332 every 3s, for 40 frames (or a total duration of 120s or 2 minutes). To improve visualization of
1333 TRN-associated BL structures, we generated confocal stacks of transgenic animals (Figure 1C-
1334 D) using an inverted, laser-scanning confocal microscope (Leica SP8, Stanford Cell Sciences
1335 Imaging Facility) and a 40X oil-immersion lens (Leica 40X HC PL APO, CS2, oil, NA=1.30).

1336 Time-lapse imaging and fluorescence recovery after photobleaching (FRAP)

1337 We conducted FRAP experiments in living animals, mounting animals as described
1338 above and generated time-lapse images on an inverted, laser-scanning confocal microscope
1339 (Leica SP8, Stanford Cell Sciences Imaging Facility) at 40X magnification (Leica 40X HC PL
1340 APO, CS2, oil, NA=1.30). Briefly, an image scientist (AD or DC) acquired images at 1 fps for
1341 10 frames prior to bleaching, selected a region of interest (~15x15 pixels) containing a defined
1342 punctum or in an inter-punctum interval, and scanned that region at maximum power for 3.5 s to
1343 bleach the fluorophores present. Following bleaching, we acquired images every 5 seconds
1344 (mNG::MEC-4, LAM-2::mNG, NID-1::mNG and SDN-1::mNG) or every 1 second (myr::GFP)
1345 for 60 frames.

1346 C. elegans TRNs in culture

1347 We used the Keyence instrument (BZ-X800) to generate still fluorescence images of
1348 dissociated, live TRNs using a similar strategy, 24 or 48 hours after plating on 6-well glass-
1349 bottom dishes coated with PNA, uniformly or in a striped pattern. We acquired images using a
1350 60x oil immersion objective (Nikon Plan Apo lambda 60x), using the following parameters:
1351 binning (1x1), 1.5 ms exposures in the green (mNG) channel and 16ms exposures in the red
1352 (mCherry) channel. In addition to epifluorescence images, we also collected brightfield images
1353 of the same fields (1x1 binning, 6 msec exposure). Widefield images were saved as 32-bit RGB
1354 *.tiff files. We used time-lapse software to collect dual-color time-lapse image stacks (Figure
1355 S3D) using the same microscope (Keyence BZ-X800) and objective (Nikon Plan Apo lambda
1356 60x), using the following acquisition parameters: 1x1 binning, 1 frame every 6s, for 20 frames
1357 (or a total duration of 120s or 2 minutes).

1358 QUANTIFICATION AND STATISTICAL ANALYSIS

1359 Serial-section TEM reconstruction

1360 For data stacks generated for Krieg, et al., 2017, we used ImageJ (Rasband, 1997) to
1361 measure the width and height of ECM beam structures in single transmission electron
1362 micrographs. In order to determine their length and generate three-dimensional models, we used
1363 Reconstruct software (Fiala, 2005), a legacy editor for serial-section TEM analysis running under
1364 WindowsXP or Linux (https://www.bu.edu/neural/Reconstruct.html). In brief, all images of
1365 consecutive sections were aligned manually and the outline of the ECM beams, TRN membrane,
1366 and epidermal cell basal membrane were traced by hand. For all other datastacks, either
1367 individual images or montaged sections were aligned with TrakEM2 (Cardona et al., 2012) in
1368 Fiji (Schindelin et al., 2012) using elastic deformation corrections and examined them visually.
1369 The length of ECM beam arrays and the distance separating adjacent arrays were determined by
1370 observing the presence of beams in individual sections in these datastacks.

1371 Fluorescence signal analysis in ALM neurons

1372 Pre-processing fluorescence images of neurites

1373 We used Fiji (Schindelin et al., 2012) and Python to build an efficient, reproducible
1374 image processing pipeline for analyzing fluorescence signal distribution along ALM neurons. As
1375 described above, we first generated images showing the entire ALM neurons using the stitch-
1376 and-align function of the Keyence microscope proprietary software and exported images in *.tif
1377 format. Next, we traced the anterior processes of the ALM neurites from the cell body to the
1378 distal tip (unless otherwise mentioned) as a segmented line (line parameters: width = 20 pixels,
1379 spline fit). We converted these traces to straightened cropped sections using the built-in
1380 'Straighten' function in FIJI.

1381 Puncta analysis

1382 We then analyzed the straightened neurite images generated as described above by a
1383 custom Python script (https://github.com/wormsenseLab/Neurite_fluorescence_analysis),
1384 handling background subtraction and calculating the fluorescence intensity of a labeled protein
1385 along the neurite. Puncta were detected from these plots using the 'find_peaks' function from
1386 scipy library. To minimize bias in peak detection from differences in expression levels, we

1387 employed adaptive threshold estimation for each image, as a function of the local minima and
1388 global mean and standard deviations of the fluorescence intensity for each image. For MEC-4
1389 images, the threshold estimation function additionally took into account the local average
1390 intensity since there was often a gradual decrease in overall intensity from the proximal to the
1391 distal end of the neurite. We recorded the position of each puncta as the distance of the puncta
1392 peak from the cell body along the neurite and calculated inter-punctum intervals as the distance
1393 between the peaks of neighboring puncta. We also calculated the punctate and diffuse
1394 fluorescence fractions from these intensity profiles. Except for analysis of mCherry::RAB-3, we
1395 analyzed fluorescence in the entire ALM neurite. For strains expressing mCherry::RAB-3, we
1396 focused analysis on a 200 µm-long segment of the ALM neurite immediately anterior to the cell
1397 body.

1398 Colocalization analysis

1399 We analyzed colocalization of two proteins along the ALM neurite by calculating the
1400 Intensity Correlation Quotient (ICQ). ICQ is a measure of pixel-by-pixel co-variation of
1401 intensities between two fluorescent channels. It is defined as the ratio of the number of pixels
1402 where the product of difference from mean for the red and green channels are positive, to the
1403 total number of pixels subtracted by 0.5 (Li et al., 2004). As a consequence, the ICQ values vary
1404 from 0.5 (perfect co-localization) to -0.5 (perfect exclusion). Dual-color labeling that is
1405 uncorrelated or whose analysis is impeded by background noise will give a value close to zero.
1406 To validate this approach to colocalization in the ALM neurons, we generated reference
1407 conditions in which near-perfect co-localization was expected (*i.e.* labeling NID-1 with mNG
1408 and wSc) and in which no colocalization was expected (*i.e.* dual-labeling with a punctate and
1409 diffuse marker). Previously, we used this approach to analyze colocalization of antibody-labeled
1410 MEC-4, MEC-2 and MEC-5 in fixed TRNs, using two antibodies directed against MEC-2 as a
1411 co-localization reference (Cueva et al., 2007). As an additional means of cross-validation, we
1412 randomly selected red and green channels from different cells within each dataset and used the
1413 resulting simulated pairs to compute ICQ. In all cases and as expected, the simulated pairs had
1414 ICQ values close to zero (Figure 2F, 7H, S4E, S5E, S7G, S7J).

1415 We also determined object colocalization by measuring the percentfage of detected
1416 puncta in one channel that co-localized with puncta detected in the other channel and vice-versa.

1417 We defined positive co-localization if the peaks of two puncta were less than 0.5 um apart. As
1418 above, we also computed the co-localization of puncta between red and green channels randomly
1419 selected from different cells within each dataset, to estimate the expected baseline level of puncta
1420 colocalization between two random fluorescence profiles with similar overall number and
1421 spacing of puncta. In all cases and as expected, these values were close to zero (Figure S2F-G,
1422 S4F-G, S5F-G, S7H-I, S7K-L)

1423 FRAP analysis

1424 We processed the time-lapse image stacks of ALM neurons before and after
1425 photobleaching as follows. First, we traced ALM neurites (using the segmented line tool in
1426 ImageJ), converting the image stack to a kymograph of the ALM neurite. We then inspected
1427 kymographs for global movement of the neurite during image acquisition and for the appearance
1428 of moving puncta, excluding samples with clear evidence of movement from further analysis.
1429 Once validated, we generated a straightened, 21-pixel wide cropped image stack, containing the
1430 ALM neurite. We then analyzed the cropped image stacks using a custom Python script
1431 (https://github.com/wormsenseLab/FRAP) to detect the bleached region based on the expectation
1432 that it would contain the maximum change in fluorescence intensity between the last three
1433 frames collected prior to bleaching and the first three frames after bleaching. The average
1434 fluorescence intensity in the bleached region for each time point was corrected for overall
1435 photobleaching over the time period of image acquisition, by dividing by the average
1436 fluorescence intensity in the non-bleached region at the same time point. These corrected values
1437 were then normalized by setting the average pre-bleach intensity to 1 and the intensity of the first
1438 frame after photobleaching to zero. We calculated the maximum fractional fluorescence recovery
1439 as the average recovery observed for the last three time-points of the time-lapse.

1440 *Statistical analysis*

1441 Inter-punctum intervals (IPIs)

1442 In this study, we relied on inter-punctum intervals as a standardized measure of the
1443 distribution of discrete puncta. This metric has been used previously to analyze the distribution
1444 of MEC-4 channels (Arnadottir et al, 2011; Cueva et al, 2007; Vasquez et al, 2014) and here we
1445 use it for this purpose and for analyzing the associated BL puncta. Because IPI is derived from
1446 the distance between the location of the peak intensity of each punctum and its neighbor, it is

more robust to background noise and errors inherent in intensity-based image segmentation. Table S2 collects and summarizes IPI measurements (mean±standard deviation, median ± interquartile range, number of ALMs analyzed, number of IPIs analyzed) as a function of each *C. elegans* strain. For pairwise comparison of cumulative distributions of IPI values, we performed the Kolmogorov-Smirnof test (using the scipy.stats library in Python) and reported the corresponding ks-statistic and p-value on the respective figures. For comparing IPIs between three or more groups, we performed 1-way ANOVA and Tukey-HSD post hoc testing (using the statsmodels library in Python), and reported the results in the figure legend.

Other data types

In addition to summarizing IPI measurements, Table S2 also summarizes other measurements derived from still and time-lapse imaging (ICQ measurements, puncta colocalization, MEC-4 fluorescence intensity, maximum fluorescence recovery after photobleaching), *in vivo* whole-cell patch clamp recordings (peak mechanoreceptor currents), and behavioral studies touch sensitivity. We performed Student's t-test (using the scipy.stats library in Python) for comparison between two groups, 1-way ANOVA with Tukey post hoc testing (using the statsmodels library in Python) for comparison between three or more groups with one independent variable, and 2-way ANOVA with Tukey post hoc testing (using the statsmodels library in Python) for comparison between three or more groups with two independent variables, and reported the results in the figure legend. For determination of statistically significant differences between groups, p-value cutoff was set at 0.05.

1468 SUPPLEMENTARY INFORMATION TITLES AND LEGENDS

1469 ***Movie S1: TEM serial section ALML showing discontinuous ECM beams (related to Figure***
1470 ***1E)***

1471 ***Table S1. List of all strains used in screening for localization of proteins along TRNs***

1472 ***Table S2: Summary data tables***
1473 **A. Inter-punctum interval**
1474 **B. Punctum length**
1475 **C. ICQ**
1476 **D. Puncta colocalization**
1477 **E. MEC-4 intensity**
1478 **F. FRAP**
1479 **G. Touch score**
1480 **H. Peak MRC amplitude**
1481

1482 ***Figure S1. TEM images of TRN cross sections showing discontinuous segments containing***
1483 ***beam-like structure in the ECM , related to Figure 1E.***
1484 **A-D**. TEM micrographs showing the cross sections of TRNs at different points along the neuron
1485 in a serial section stack. (A) and (B) show the ALMR and AVM neurons, respectively, from the
1486 same worm as the ALML shown in Figure 1E. (C) and (D) show the PLM and PVM neurons
1487 from a different worm. Red arrows point towards the electron dense ECM beams in the
1488 extracellular space between the TRN and the epidermis. z-axis maps of the entire serial section
1489 stack of TEM images used for the respective top panels show the relative position of the
1490 segments with (red) or without (yellow) visible ECM beams. Red numbers indicate the length (in
1491 microns) of each segment with visible ECM beams. Black numbers indicate the distance (in
1492 microns) between the mid-points of successive red segments.
1493 **E.** TEM micrographs showing the cross sections of several neurons in the ventral cord, including
1494 the PVM (left) or AVM (right). AVM and PVM neurons are highlighted in yellow. Red arrows
1495 point towards the electron dense ECM beams in the extracellular space between the TRN and the
1496 epidermis. The micrograph of PVM (left) and AVM (right) is from the same series shown in Fig.

1497 S1D and Fig. S1B, respectively. Scale bars = 500 nm.
1498

1499 ***Figure S2. Punctum length and FRAP fractional recovery for BL proteins and the MEC-4***
1500 ***channel, related to Figure 2.***
1501 **A.** Boxplots showing the distribution of punctum lengths for LAM-1::wSc, LAM-2::mNG,
1502 NID-1::wSc and mNG::MEC-4. The dataset used is the same as that in Figure 2B. Box denotes
1503 the median and interquartile range, while whiskers extend to the limits of the distribution
1504 excluding outliers. One-way ANOVA comparing punctum lengths across different protein labels
1505 shows statistically significant differences [$F(3,11753) = 68.05$, $p = 1.28e\text{-}43$]. Tukey HSD post
1506 hoc analysis shows significant differences ($p = 0.001$, groups connected by gray bars) between
1507 all pairs except NID-1::wSc and mNG::MEC-4. Summary data are in Table S2.
1508 **B.** Representative, *in vivo* live imaging of myristoylated GFP (myr::GFP) expressed in the TRNs.
1509 Top two panels show fluorescence before and after bleaching, respectively; the bottom panel
1510 shows a kymograph (distance-time image) of a 10 s pre-bleach period and 60 s observation
1511 period.
1512 **C.** Fluorescence recovery after photobleaching (FRAP) for myr::GFP. About 70% fluorescence
1513 recovery for myr::GFP was seen during the observation period. Dark trace and shaded regions
1514 show the average and standard deviation of the trajectory of fluorescence recovery for 14
1515 neurons.
1516 **D-E.** Fractional fluorescence recovery at 300 s (D) and 60 s (E) after photobleaching for the
1517 different protein labels. The dataset used is the same as in Figure 2D, S2C. One-way ANOVA
1518 shows statistically significant differences among groups (Panel D: $F(3,48) = 68.73$, $p = 2.15e\text{-}17$;
1519 Panel E: $F(4,61) = 179.11$, $p = 5.64e\text{-}33$). Tukey HSD post hoc analysis shows significant
1520 differences (groups connected by gray bars, $p = 0.001$) between all pairs except NID-1::mNG
1521 and LAM-2::mNG.
1522 **F-G.** Plots showing the fraction of green puncta that co-localize with red puncta (F) or vice-versa
1523 (G) as a function of genotype. The dataset used is the same as in Figure 2F. Each circle shows a
1524 measurement from a single ALM neurite. Black squares show the mean of the filled circles or
1525 open circles respectively, and the black bars show standard deviation. In all cases, the fractional
1526 puncta colocalization between two fluorescence channels from the same cell (circles) are
1527 significantly higher (Student's t-test, $p<0.05$) than that measured for simulated pairs (boxplots

1528 showing the interquartile (box) and full range (whiskers), excluding outliers). One-way ANOVA
1529 showed a significant effect of the protein pair (Panel F: $F(4,65) = 19.87$, $p = 1.0e-10$; Panel G:
1530 $F(4,65) = 11.74$, $p = 3.1e-7$). Gray bars connect the groups whose fractional puncta
1531 colocalization differ from one another by Tukey post hoc analysis ($p < 0.005$). Summary data are
1532 in Table S2.
1533

1534 ***Figure S3. Basal lamina proteins in other tissues and TRNs (A-B), co-localization and co-***
1535 ***transport of RAB-3, MEC-4 and NID-1 (C-F), and fractional recovery as a function of***
1536 ***genotype (G), related to Figure 3.***
1537 **A.** Representative images of animals expressing NID-1::wSc (left) and LAM-2::mNG (right) in
1538 control, *mec-5(u444)*, *mec-1(e1738)* and *mec-9(u437)* animals showing the similarity in
1539 distribution in basal lamina surrounding the gonad as a function of genotype. Scale bars = 100
1540 µm.
1541 **B.** Fluorescence photomicrographs of animals co-expressing LAM-2::mNG and a cytoplasmic
1542 RFP marker in the TRNs revealing discrete LAM-2 puncta associated with the TRNs in control,
1543 but not in *mec-5(u444)*, *mec-1(e1738)* and *mec-9(u437)* animals. Scale bars = 10 µm.
1544 **C-E**. Kymographs of dual labeled TRNs showing that mobile mNG::MEC-4 puncta co-localize
1545 with mCherry::RAB-3 puncta *in vivo* (C) and in TRNs cultured *in vitro* (D), but do not co-
1546 localize with NID-1::wSc puncta *in vivo* (E).
1547 **F.** Plot showing the density (average number of puncta per 20 µm) of all detected
1548 mCherry::RAB-3 positive vesicles (magenta) and MEC-4-containing RAB-3 positive vesicles
1549 (white) in each cell. The dataset used is the same as in Figure 3D. Pairs of data points from
1550 individual cells are connected by magenta lines. Circles denote mean values and thick vertical
1551 lines show the standard deviation. One-way ANOVA fails to detect an effect of genotype on total
1552 RAB-3 density [$F(3,80) = 2.22$, $p = 0.09$] and on the density of MEC-4-containing RAB-3
1553 puncta [$F(3,80) = 1.77$, $p = 0.16$].
1554 **G.** Plots showing the fractional fluorescence recovery at 300 s after photobleaching for the
1555 different genotypes. The dataset used is the same as in Figure 3F. One-way ANOVA shows
1556 statistically significant effect of genotype [$F(2,67) = 3.35$, $p = 0.04$] and a post hoc analysis
1557 (Tukey HSD) shows a significant difference (groups connected by gray bars) between control
1558 and *mec-1(e1738)* but no significant difference between *mec-1* and *mec-9* mutants.

1559

1560 ***Figure S4. Mechanosensory ECM assembly is not dependent on the ion-channel subunits or***
1561 ***TRN microtubules, related to Figure 4.***
1562 **A.** Representative images of LAM-1::wSc puncta present in *mec-4(u253)mec-10(tm1552)* double
1563 mutant (top) and *mec-4(u253)mec-10(tm1552);degt-1(tm6356)* triple mutant (bottom). Anterior
1564 is to the left; scale bars are 10 µm.
1565 **B.** Probability density distribution plots of IPIs (top) and the individual IPIs (bottom) for
1566 LAM-1::wSc in *mec-4(u253);mec-10(tm1552)* double mutant and
1567 *mec-4(u253);mec-10(tm1552)degt-1(tm6356)* triple mutant. White circles denote mean, thin
1568 vertical lines denote the median and thick horizontal lines denote the interquartile ranges of the
1569 population. Summarized data are collected in Table S2.
1570 **C.** Plots of cumulative probability distribution of LAM-1::wSc IPIs in the indicated alleles
1571 (green) vs control worms (gray, replotted from Figure 2B). The results of two-sample
1572 Kolmogorov-Smirnov tests are indicated in each plot.
1573 **D.** Stacked bar plots representing the fraction of MEC-4 in mechanosensory complexes (dark
1574 green), and in the diffuse pool (light green) in control vs. *mec-7(ok2152)* animals show that
1575 MEC-4 is distributed evenly between the two pools in both genotypes. The dataset used is the
1576 same as in Figure 4E-F. Student's t-test shows no significant difference in the fraction of MEC-4
1577 in mechanosensory complexes between the two genotypes ($p=0.13$). Summarized data are
1578 collected in Table S2.
1579 **E-G.** MEC-4 and NID-1 puncta co-localize in control and *mec-7(ok2152)* animals. Plots showing
1580 ICQ (E), the fraction of MEC-4 puncta that co-localize with NID-1 puncta (F) or vice-versa (G)
1581 as a function of genotype. The dataset used is the same as in Figure 4E-F. Each circle (open
1582 circles: control, filled circles: *mec-7(ok2152)*) shows a measurement from a single ALM neurite.
1583 Black squares show the mean and the black bars show standard deviation. Observed ICQ and
1584 fractional puncta colocalization values for control are significantly higher (gray bars connecting
1585 groups with $p<0.05$ in Student's t-test) than *mec-7(ok2152)* in E, F and G. For both genotypes,
1586 the ICQ (E) or fractional puncta colocalization values (F,G) between two fluorescence channels
1587 from the same cell (circles) are significantly higher (p-values<0.05 in Student's t-test) than that
1588 measured for simulated pairs (boxplots, box: interquartile range, whiskers: full range excluding
1589 outliers). Summarized data are collected in Table S2.

1590

1591 ***Figure S5. Effect of loss of epi-1 and nid-1 on MEC-4 puncta (A-D), MEC-4 co-localization***
1592 ***with BL proteins (E-G), and voltage-gated currents in ALM as function of genotype (H-I),***
1593 ***related to Figure 5.***

1594 **A.** Representative images showing mNG::MEC-4 localize to discrete puncta distributed along
1595 the ALM neurons and TRN morphology defects in *epi-1(gm57)* adult animals. Boxed area in the
1596 top panel is expanded in the lower panel. Similar patterns observed in 9 ALM neurons in 9 adult
1597 animals.

1598 **B.** Probability density distribution plots of IPIs (top) and the individual IPIs (bottom) for
1599 mNG::MEC-4 in *epi-1(gm57)* mutant animals. Due to the TRN morphological defects the
1600 complete TRNs could not be analyzed in their entirety; instead IPIs were measured in 13
1601 segments that were at least 50 µm long drawn from 9 independent biological replicates (ALM
1602 neurites). White circles denote mean, thin vertical lines denote the median and thick horizontal
1603 lines denote the interquartile ranges of the population. Summarized data are collected in Table
1604 S2.

1605 **C.** Cumulative distribution plots of mNG::MEC-4 puncta distribution in *epi-1(gm57)* mutants
1606 and control animals. The green and gray lines are data for *epi-1(gm57)* and control, respectively.
1607 Control IPIs were computationally selected from 20 randomly positioned 50 µm ALM segments
1608 in 15 control animals to provide a better match to the analysis available for *epi-1(gm57)* animals.
1609 The results of two-sample Kolmogorov-Smirnov tests showing no significant difference between
1610 the two distributions are indicated in the plot.

1611 **D.** Stacked barplots representing the fraction of MEC-4 in mechanosensory complexes (dark
1612 green), and in the diffuse pool (light green) in control vs. *nid-1(cg119)* mutant animals show that
1613 *nid-1* loss of function redistributes MEC-4 to a diffuse membrane pool. The dataset used is the
1614 same as in Figure 5E-F. Numbers in the bar graph indicate the sample size (number of ALMs)
1615 and error bars show standard deviations of the measurements for each genotype. Student's t-test
1616 shows a significant difference (gray bar) in the MEC-4 diffuse pool between the genotypes
1617 (p=2.28e-21). Summarized data are collected in Table S2.

1618 **E-G.** Loss of *nid-1* function decreases MEC-4 and LAM-1 intensity correlation, even though
1619 individual puncta co-occur more often than expected from a random distribution. Plots showing
1620 ICQ (E), the fraction of MEC-4 puncta that co-localize with LAM-1 puncta (F) or vice-versa (G)

1621 as a function of genotype. The dataset used is the same as in Figure 5E-F. Each circle (open
1622 circles: control, filled circles: *nid-1(cg119)*) shows a measurement from a single ALM neurite.
1623 Black squares show the mean of the filled circles or open circles respectively, and the black bars
1624 show standard deviation. Observed ICQ and fractional puncta colocalization values for control
1625 are significantly higher (Student's t-test, $p<0.05$) than *nid-1(cg119)* in E, F and G. For both
1626 genotypes the ICQ (E) or fractional puncta colocalization values (F,G) between two fluorescence
1627 channels from the same cell (circles) are significantly higher (gray bars connecting groups with
1628 p-values<0.05 in Student's t-test) than that measured for simulated pairs (boxplots, box: inter-
1629 quartile range, whiskers: full range excluding outliers). Summarized data are collected in Table
1630 S2.
1631 **H.** Representative membrane current traces evoked by voltage pulses (from -80 to +80mV, in 20
1632 mV increments) applied from a holding potential of -60 mV. Each trace represents the average of
1633 three stimulus presentations for control (left, dark gray), *nid-1(cg119)* (middle, green) and *mec-*
1634 *5(u444)* (right, magenta) mutants. Traces are shaded according to the voltage applied during the
1635 step. Similar results obtained in a total of 11, 9 and 2 recordings for control, *nid-1* and *mec-5*
1636 animals, respectively.
1637 **I.** Peak current vs. voltage. Dark gray, dark green and magenta traces are the average peak
1638 current of the lighter gray, green and magenta traces for control, *nid-1* and *mec-5* mutants,
1639 respectively. For individual recordings, membrane voltage is corrected for residual series
1640 resistance.
1641

1642 ***Figure S6. NID-1[ΔG3], LAM-2[NSS] and LAM-3[NSS] mutations successfully disrupt***
1643 ***nidogen/laminin binding, related to Figure 6.***
1644 **A.** Stacked bars representing the fraction of MEC-4 in the diffuse pool (light green) and
1645 mechanosensory complexes (dark green) as a function of genotype. One-way ANOVA shows a
1646 significant effect of genotype [$F(6,188) = 148.43$, $p = 1.51e-68$]. Gray bars connect groups that
1647 are significantly different ($p<0.05$) from control by Tukey-HSD post hoc analysis. Numbers on
1648 bars indicate the number of biological replicates for each genotype. Summary data in Table S2.
1649 **B.** Touch response as a function of genotype. One-way ANOVA shows significant differences
1650 between groups [$F(6,518) = 29.88$, $p = 8.51e-31$]. gray bars connect groups which are
1651 significantly different ($p<0.05$) from control by Tukey-HSD post hoc analysis. Bars are the

1652 average (± SEM) response to 10 touches of *n=75* animals tested blind to genotype in 3
1653 independent cohorts. Summarized data are collected in Table S2.
1654 **C.** Summary of the NID-1 localization in TRNs, pharynx and body wall muscles in the different
1655 genotypes. "+++" indicates strong localization, "+" indicates weak localization and "-" indicates
1656 no localization. NID-1 localization data was not collected for the NID-1[ΔG1-G2] background.
1657 Loss of NID-1 protein in the *nid-1(cg119)* null background was confirmed by Western blot in
1658 previous literature (Kang and Kramer, 2000).
1659 **D-E.** Representative images showing localization of nidogen (NID-1, magenta) and laminin-γ
1660 (LAM-2, green) to BL surrounding the pharynx (D, white arrows), nerve ring (D, white
1661 arrowheads), body wall muscle (E, black arrows) and TRN (E, black arrowheads) in the
1662 indicated mutants. Nidogen fluorescence around the pharynx and body wall muscles is lost in
1663 NID-1[ΔG3] and LAM-2[NSS]LAM-3[NSS] backgrounds. In the LAM-2[NSS] single mutant
1664 background, nidogen is partially lost from the basal lamina surrounding the pharynx and body
1665 wall muscles, indicating LAM-3 is capable of recruiting nidogen without LAM-2. In the
1666 LAM-3[NSS] single mutant, nidogen was recruited to all tissues similar to control, as LAM-2 is
1667 present in all laminin and LAM-2 is capable of recruiting nidogen without LAM-3. Nidogen
1668 fluorescence in the nervous tissue-associated BL, such as the nerve ring and puncta along TRNs
1669 are preserved in all the mutants tested, indicating the role of additional factors that recruit
1670 nidogen to these BL. In contrast, localization of laminin to the pharynx and body wall muscle is
1671 not affected in any of the mutants disrupting nidogen-laminin binding.
1672

1673 ***Figure S7. Disrupting Ku15 in MEC-1 minimally affects LAM-1, LAM-2 and NID-1 puncta***
1674 ***distribution, related to Figure 7.***
1675 **A-B**. Representative images of ALM neurons in dual-color transgenic animals showing
1676 preservation of ECM puncta (LAM-1 in A, NID-1 and LAM-2 in B) but loss of MEC-4 (A)
1677 puncta in the *mec-1(e1526)* allele. Anterior is to the left, scale bar is 10 µm.
1678 **C.** Probability density distribution plots of IPIs (top) and the individual IPIs (bottom) in
1679 *mec-1(e1526)* mutants for LAM-1::wSc and mNG::MEC-4, NID-1::wSc (E) and LAM-2::mNG
1680 (E). White circles denote mean, thin vertical lines denote the median and thick horizontal lines
1681 denote the interquartile ranges of the population. Summarized data are collected in Table S2.

1682 **D.** Plots of cumulative probability distribution of LAM-1::wSc (top) and mNG::MEC-4 (bottom)
1683 IPIs in the *mec-1(e1526)* mutant (magenta or green) vs control worms (gray, replotted from
1684 Figure 5F). The results of two-sample Kolmogorov-Smirnov tests are indicated in each plot.
1685 **E.** Probability density distribution plots of IPIs (top) and the individual IPIs (bottom) in
1686 *mec-1(e1526)* mutants for LAM-1::wSc and LAM-2::mNG. White circles denote mean, thin
1687 vertical lines denote the median and thick horizontal lines denote the interquartile ranges of the
1688 population. Summarized data are collected in Table S2.
1689 **F.** Plots of cumulative probability distribution of NID-1::wSc (top) and LAM-2::mNG (bottom)
1690 IPIs in the *mec-1(e1526)* mutant (magenta or green) vs control worms (gray). The results of two-
1691 sample Kolmogorov-Smirnov tests are indicated in each plot.
1692 **G-I.** Residual MEC-4 puncta colocalize with LAM-1 puncta in *mec-1(e1526)* animals. Plots
1693 showing ICQ of LAM-1 and MEC-4 (G), the fraction of MEC-4 puncta that co-localize with
1694 LAM-1 puncta (H) or vice-versa (I) as a function of genotype. Each circle (open circles: control,
1695 filled circles: *mec-1(e1526)*) shows a measurement from a single ALM neurite. Black squares
1696 show the mean of the filled circles or open circles respectively, and the black bars show standard
1697 deviation. Observed values for control are significantly higher (Student's t-test, $p<0.05$) than
1698 *mec-1(e1526)* in G-I (gray bars). For both genotypes the ICQ (G) or fractional puncta
1699 colocalization values (H,I) between two fluorescence channels from the same cell (circles) are
1700 significantly higher (Student's t-test, $p<0.05$) than that measured for simulated pairs (boxplots,
1701 box: inter-quartile range, whiskers: full range excluding outliers). Summarized data are collected
1702 in Table S2.
1703 **J-L.** LAM-2 and NID-1 puncta co-localize in control and *mec-1(e1526)* animals. Plots showing
1704 ICQ of NID-1 and LAM-2 (J), fraction of LAM-2 puncta that co-localize with NID-1 puncta (K)
1705 or vice-versa (L) as a function of genotype. Each circle (open circles: control, filled circles: *mec-*
1706 *1(e1526)*) shows a measurement from a single ALM neurite. Black squares show the mean of the
1707 filled circles or open circles respectively, and the black bars show standard deviation. ICQ values
1708 for control are not significantly different (Student's t-test, $p=0.09$) from *mec-1(e1526)* (J). There
1709 are small but statistically significant differences in fractional puncta colocalization values (K,
1710 $p=0.006$; L, $p=0.049$) between control and *mec-1(e1526)* animals (gray bars). For both genotypes
1711 the ICQ (J) or fractional puncta colocalization values (K,L) between two fluorescence channels
1712 from the same cell (circles) are significantly higher (Student's t-test, $p<0.05$) than that measured

from simulated pairs (boxplots, box: inter-quartile range, whiskers: full range excluding outliers). Summarized data are collected in Table S2.

1716 **References**

1717 Ackley, B.D., Kang, S.H., Crew, J.R., Suh, C., Jin, Y., and Kramer, J.M. (2003). The basement
1718 membrane components nidogen and type XVIII collagen regulate organization of neuromuscular
1719 junctions in *Caenorhabditis elegans*. J. Neurosci. *23*, 3577–3587.

1720 Ackley, B.D., Harrington, R.J., Hudson, M.L., Williams, L., Kenyon, C.J., Chisholm, A.D., and
1721 Jin, Y. (2005). The two isoforms of the *Caenorhabditis elegans* leukocyte-common antigen
1722 related receptor tyrosine phosphatase PTP-3 function independently in axon guidance and
1723 synapse formation. J. Neurosci. *25*, 7517–7528.

1724 Árnadóttir, J., O'Hagan, R., Chen, Y., Goodman, M.B., Chalfie, M. (2011). The DEG/ENaC
1725 protein MEC-10 regulates the transduction channel complex in *Caenorhabditis elegans* touch
1726 receptor neurons. J. Neurosci. *31*, 12695–12704.

1727 Arribere, J.A., Bell, R.T., Fu, B.X.H.H., Artiles, K.L., Hartman, P.S., and Fire, A.Z. (2014).
1728 Efficient marker-free recovery of custom genetic modifications with CRISPR/Cas9 in
1729 *Caenorhabditis elegans*. Genetics 198, 837–846.

1730 Aumailley, M. (2013). The laminin family. Cell Adhes. Migr. *7*, 48–55.

1731 Aumailley, M. (2021). Laminins and interaction partners in the architecture of the basement
1732 membrane at the dermal-epidermal junction. Exp. Dermatol. *30*, 17–24.

1733 Aumailley, M., Battaglia, C., Mayer, U., Reinhardt, D., Nischt, R., Timpl, R., and Fox, J.W.
1734 (1993). Nidogen mediates the formation of ternary complexes of basement membrane
1735 components. Kidney Int. *43*, 7–12.

1736 Baconguis, I., Bohlen, C.J., Goehring, A., Julius, D., and Gouaux, E. (2014). X-ray structure of
1737 acid-sensing ion channel 1-snake toxin complex reveals open state of a Na+-selective channel.
1738 Cell *156*, 717–729.

1739 Bader, B.L., Smyth, N., Nedbal, S., Miosge, N., Baranowsky, A., Mokkapati, S., Murshed, M.,
1740 and Nischt, R. (2005). Compound genetic ablation of nidogen 1 and 2 causes basement
1741 membrane defects and perinatal lethality in mice. Mol. Cell. Biol. *25*, 6846–6856.

1742 Bianchi, L., and Driscoll, M. (2006). Culture of embryonic *C. elegans* cells for
1743 electrophysiological and pharmacological analyses. WormBook 1–15.

1744 Bohlen, C.J., Chesler, A.T., Sharif-Naeini, R., Medzihradszky, K.F., Zhou, S., King, D.,
1745 Sánchez, E.E., Burlingame, A.L., Basbaum, A.I., and Julius, D. (2011) . A heteromeric Texas
1746 coral snake toxin targets acid-sensing ion channels to produce pain. Nature 479, 410–414.

1747 Böse, K., Nischt, R., Page, A., Bader, B.L., Paulsson, M., and Smyth, N. (2006). Loss of
1748 nidogen-1 and -2 results in syndactyly and changes in limb development. J. Biol. Chem. *281*,
1749 39620–39629.

1750 Bounoutas, A., Kratz, J., Emtage, L., Ma, C., Nguyen, K.C., and Chalfie, M. (2011). Microtubule
1751 depolymerization in *Caenorhabditis elegans* touch receptor neurons reduces gene expression
1752 through a p38 MAPK pathway. Proc. Natl. Acad. Sci. U. S. A. 108, 3982–3987.

1753 Cardona, A., Saalfeld, S., Schindelin, J., Arganda-Carreras, I., Preibisch, S., Longair, M.,
1754 Tomancak, P., Hartenstein, V., and Douglas, R.J. (2012). TrakEM2 software for neural circuit
1755 reconstruction. PLoS One 7, e38011.

1756 Cascio, C.J., Moore, D., and McGlone, F. (2019). Social touch and human development. Dev.
1757 Cogn. Neurosci. *35*, 5–11.

1758 Chalfie, M. (1993). Touch receptor development and function in *Caenorhabditis elegans*. J.
1759 Neurobiol. *24(10)*, 1433-1441.

1760 Chalfie, M., and Au, M. (1989). Genetic control of differentiation of the *Caenorhabditis elegans*
1761 touch receptor neurons. Science. *243*, 1027–1033.

1762 Chalfie, M., Hart, A.C., Rankin, C.H., and Goodman, M.B. (2014). Assaying mechanosensation.
1763 WormBook 1–13.

1764 Chalfie, M., and Sulston, J. (1981). Developmental genetics of the mechanosensory neurons of
1765 *Caenorhabditis elegans*. Dev. Biol. *82*, 358–370.

1766 Chatzigeorgiou, M., Grundy, L., Kindt, K.S., Lee, W.-H., Driscoll, M., and Schafer, W.R.
1767 (2010). Spatial asymmetry in the mechanosensory phenotypes of the *C. elegans* DEG/ENaC

1768 gene *mec-10*. J. Neurophysiol. *104*, 3334–3344.

1769 Chelur, D.S., Ernstrom, G.G., Goodman, M.B., Yao, C.A., Chen, L., O'Hagan, R., Chalfie, M.,
1770 O' Hagan, R., Chalfie, M., O'Hagan, R., et al. (2002). The mechanosensory protein MEC-6 is a
1771 subunit of the *C. elegans* touch-cell degenerin channel. Nature *420*, 669–673.

1772 Chen, X., and Chalfie, M. (2014). Modulation of *C. elegans* touch sensitivity is integrated at
1773 multiple levels. J. Neurosci. *34*, 6522–6536.

1774 Chen, X., and Chalfie, M. (2015). Regulation of mechanosensation in *C. elegans* through
1775 ubiquitination of the MEC-4 mechanotransduction channel. J. Neurosci. *35*, 2200–2212.

1776 Cheng, Y.S., Champliaud, M.F., Burgeson, R.E., Marinkovich, M.P., and Yurchenco, P.D.
1777 (1997). Self-assembly of laminin isoforms. J. Biol. Chem. *272*, 31525–31532.

1778 Chiang, L.Y., Poole, K., Oliveira, B.E., Duarte, N., Sierra, Y.A.B., Bruckner-Tuderman, L.,
1779 Koch, M., Hu, J., and Lewin, G.R. (2011). Laminin-332 coordinates mechanotransduction and
1780 growth cone bifurcation in sensory neurons. Nat. Neurosci. *14*, 993–1000.

1781 Christensen, M., and Strange, K. (2001). Developmental regulation of a novel outwardly
1782 rectifying mechanosensitive anion channel in *Caenorhabditis elegans*. J. Biol. Chem. *276*,
1783 45024–45030.

1784 Christensen, M., Estevez, A., Yin, X., Fox, R., Morrison, R., McDonnell, M., Gleason, C.,
1785 Miller, D.M., and Strange, K. (2002). A primary culture system for functional analysis of *C.*
1786 *elegans* neurons and muscle cells. Neuron *33*, 503–514.

1787 Clay, M.R., and Sherwood, D.R. (2015). Basement Membranes in the Worm: A dynamic
1788 scaffolding that instructs cellular behaviors and shapes tissues. Current Topics in Membranes,
1789 (Academic Press), pp. 337–371.

1790 Coakley, S., Ritchie, F.K., Galbraith, K.M., and Hilliard, M.A. (2020). Epidermal control of
1791 axonal attachment via β-spectrin and the GTPase-activating protein TBC-10 prevents axonal
1792 degeneration. Nat. Commun. *11*, 1–12.

1793 Cristofori-Armstrong, B., and Rash, L.D. (2017). Acid-sensing ion channel (ASIC) structure and

1794 function: Insights from spider, snake and sea anemone venoms. Neuropharmacology *127*, 173–
1795 184.

1796 Cueva, J.G., Mulholland, A., and Goodman, M.B. (2007). Nanoscale organization of the MEC-4
1797 DEG/ENaC sensory mechanotransduction channel in *Caenorhabditis elegans* touch receptor
1798 neurons. J. Neurosci. *27*, 14089–14098.

1799 Dai, J., Estrada, B., Jacobs, S., Sánchez-Sánchez, B.J., Tang, J., Ma, M., Magadán-Corpas, P.,
1800 Pastor-Pareja, J.C., and Martín-Bermudo, M.D. (2018). Dissection of Nidogen function in
1801 Drosophila reveals tissue-specific mechanisms of basement membrane assembly. PLoS Genet.
1802 *14*, e1007483.

1803 Davis, P., Zarowiecki, M., Arnaboldi, V., Becerra, A., Cain, S., Chan, J., Chen, W.J., Cho, J., da
1804 Veiga Beltrame, E., Diamantakis, S., et al. (2022). WormBase in 2022—data, processes, and
1805 tools for analyzing *Caenorhabditis elegans*. Genetics 220, iyac003.

1806 Díaz-Balzac, C.A., Rahman, M., Lázaro-Peña, M.I., Martin Hernandez, L.A., Salzberg, Y.,
1807 Aguirre-Chen, C., Kaprielian, Z., and Bülow, H.E. (2016). Muscle- and skin-derived cues jointly
1808 orchestrate patterning of somatosensory dendrites. Curr. Biol. *26*, 2379–2387.

1809 Dickinson, D.J., Pani, A.M., Heppert, J.K., Higgins, C.D., and Goldstein, B. (2015). Streamlined
1810 genome engineering with a self-excising drug selection cassette. Genetics 200, 1035–1049.

1811 Domogatskaya, A., Rodin, S., and Tryggvason, K. (2012). Functional diversity of laminins.
1812 Annu. Rev. Cell Dev. Biol. *28*, 523–553.

1813 Dong, L., Chen, Y., Lewis, M., Hsieh, J.C., Reing, J., Chaillet, J.R., Howell, C.Y., Melhem, M.,
1814 Inoue, S., Kuszak, J.R., et al. (2002). Neurologic defects and selective disruption of basement
1815 membranes in mice lacking entactin-1/nidogen-1. Lab. Invest. *82*, 1617–1630.

1816 Driscoll, M., and Chalfie, M. (1991). The *mec-4* gene is a member of a family of *Caenorhabditis*
1817 *elegans* genes that can mutate to induce neuronal degeneration. Nature *349*, 588–593.

1818 Du, H., Gu, G., William, C.M., and Chalfie, M. (1996). Extracellular proteins needed for *C.*
1819 *elegans* mechanosensation. Neuron *16*, 183–194.

1820 Dziadek, M., and Timpl, R. (1985). Expression of nidogen and laminin in basement membranes
1821 during mouse embryogenesis and in teratocarcinoma cells. Dev. Biol. 111, 372–382.

1822 Eastwood, A.L., Sanzeni, A., Petzold, B.C., Park, S.J., Vergassola, M., Pruitt, B.L., and
1823 Goodman, M.B. (2015). Tissue mechanics govern the rapidly adapting and symmetrical response
1824 to touch. Proc. Natl. Acad. Sci. U. S. A. 112, E6955–E6963.

1825 Emtage, L., Gu, G., Hartwieg, E., and Chalfie, M. (2004). Extracellular proteins organize the
1826 mechanosensory channel complex in *C. elegans* touch receptor neurons. Neuron *44*, 795–807.

1827 Fiala, J.C. (2005). Reconstruct: A free editor for serial section microscopy. J. Microsc. 218, 52–
1828 61.

1829 Forrester, W.C., Perens, E., Zallen, J.A., and Garriga, G. (1998). Identification of *Caenorhabditis*
1830 *elegans* Genes Required for Neuronal Differentiation and Migration. Genetics *148*, 151–165.

1831 Fox, J.W., Mayer, U., Nischt, R., Aumailley, M., Reinhardt, D., Wiedemann, H., Mann, K.,
1832 Timpl, R., Krieg, T., and Engel, J. (1991). Recombinant nidogen consists of three globular
1833 domains and mediates binding of laminin to collagen type IV. EMBO J. 10, 3137–3146.

1834 Franco, J. A. (2021). Methods for robust measurements in low signal-to-noise systems and their
1835 application to nematode mechanoreceptors (Doctoral dissertation, Stanford University).

1836 Frédéric, M.Y., Lundin, V.F., Whiteside, M.D., Cueva, J.G., Tu, D.K., Kang, S.Y.C., Singh, H.,
1837 Baillie, D.L., Hutter, H., Goodman, M.B., et al. (2013). Identification of 526 conserved metazoan
1838 genetic innovations exposes a new role for cofactor E-like in neuronal microtubule homeostasis.
1839 PLoS Genet. *9*.

1840 Goodman, M.B., Hall, D.H., Avery, L., and Lockery, S.R. (1998). Active currents regulate
1841 sensitivity and dynamic range in *C. elegans* neurons. Neuron 20, 763–772.

1842 Goodman, M.B., Haswell, E.S., and Vásquez, V. (2023). Mechanosensitive membrane proteins:
1843 Usual and unusual suspects in mediating mechanotransduction. J. Gen. Physiol. *155*,
1844 e202213248.

1845 Graham, P.L., Johnson, J.J., Wang, S., Sibley, M.H., Gupta, M.C., and Kramer, J.M. (1997).

1846 Type IV collagen is detectable in most, but not all, basement membranes of *Caenorhabditis*
1847 *elegans* and assembles on tissues that do not express it. J. Cell Biol. *137*, 1171–1183.

1848 Gu, G., Caldwell, G.A., and Chalfie, M. (1996). Genetic interactions affecting touch sensitivity
1849 in *Caenorhabditis elegans*. Proc. Natl. Acad. Sci. U. S. A. 93, 6577–6582.

1850 Hamill, K.J., Kligys, K., Hopkinson, S.B., and Jones, J.C.R. (2009). Laminin deposition in the
1851 extracellular matrix: A complex picture emerges. J. Cell Sci. *122*, 4409–4417.

1852 Han, C., Wang, D., Soba, P., Zhu, S., Lin, X., Jan, L.Y., and Jan, Y.N. (2012). Integrins regulate
1853 repulsion-mediated dendritic patterning of Drosophila sensory neurons by restricting dendrites in
1854 a 2D space. Neuron *73*, 64–78.

1855 Handler, A., Zhang, Q., Pang, S., Nguyen, T.M., Iskols, M., Nolan-Tamariz, M., Cattel, S.,
1856 Plumb, R., Sanchez, B., Ashjian, K., et al. (2023). Three-dimensional reconstructions of
1857 mechanosensory end organs suggest a unifying mechanism underlying dynamic, light touch.
1858 Neuron 111, 3211-3229.e9.

1859 Heppert, J.K., Dickinson, D.J., Pani, A.M., Higgins, C.D., Steward, A., Ahringer, J., Kuhn, J.R.,
1860 and Goldstein, B. (2016). Comparative assessment of fluorescent proteins for *in vivo* imaging in
1861 an animal model system. Mol. Biol. Cell *27*, 3385–3394.

1862 Hill, P.S.M. (2008). Vibrational communication in animals (Cambridge, Mass. : Harvard
1863 University Press).

1864 Hostettler, L., Grundy, L., Käser-Pébernard, S., Wicky, C., Schafer, W.R., and Glauser, D.A.
1865 (2017). The bright fluorescent protein mNeonGreen facilitates protein expression analysis in
1866 vivo. G3 *7*, 607–615.

1867 Hsu, J.M., Chen, C.H., Chen, Y.C., McDonald, K.L., Gurling, M., Lee, A., Garriga, G., and Pan,
1868 C.L. (2014). Genetic analysis of a novel tubulin mutation that redirects synaptic vesicle targeting
1869 and causes neurite degeneration in *C. elegans*. PLoS Genet. *10*.

1870 Hu, J., Chiang, L.-Y., Koch, M., and Lewin, G.R. (2010). Evidence for a protein tether involved
1871 in somatic touch. MBO J. *29*, 855–867.

1872 Huang, C.-C., Hall, D.H., Hedgecock, E.M., Kao, G., Karantza, V., Vogel, B.E., Hutter, H.,
1873 Chisholm, A.D., Yurchenco, P.D., and Wadsworth, W.G. (2003). Laminin α subunits and their
1874 role in *C. elegans* development. Development *130*, 3343–3358.

1875 Hynes, R.O. (2012). The evolution of metazoan extracellular matrix. J. Cell Biol. *196*, 671–679.

1876 Hynes, R.O., and Naba, A. (2012). Overview of the matrisome - an inventory of extracellular
1877 matrix constituents and functions. Cold Spring Harb. Perspect. Biol. 4.

1878 Jayadev, R., and Sherwood, D.R. (2017). Basement membranes. Curr. Biol. *27*, R207–R211.

1879 Jiang, N., Rasmussen, J.P., Clanton, J.A., Rosenberg, M.F., Luedke, K.P., Cronan, M.R., Parker,
1880 E.D., Kim, H.-J., Vaughan, J.C., Sagasti, A., et al. (2019). A conserved morphogenetic
1881 mechanism for epidermal ensheathment of nociceptive sensory neurites. Elife *8*, e42455.

1882 Kang, S.H., and Kramer, J.M. (2000). Nidogen is nonessential and not required for normal type
1883 IV collagen localization in *Caenorhabditis elegans*. Mol. Biol. Cell *11*, 3911–3923.

1884 Kao, G., Huang, C.-C., Hedgecock, E.M., Hall, D.H., and Wadsworth, W.G. (2006). The role of
1885 the laminin beta subunit in laminin heterotrimer assembly and basement membrane function and
1886 development in *C. elegans*. Dev. Biol. *290*, 211–219.

1887 Katta, S., Krieg, M., and Goodman, M.B. (2015). Feeling force: physical and physiological
1888 principles enabling sensory mechanotransduction. Annu. Rev. Cell Dev. Biol. *31*, 347–371.

1889 Katta, S., Sanzeni, A., Das, A., Vergassola, M., and Goodman, M.B. (2019). Progressive
1890 recruitment of distal MEC-4 channels determines touch response strength in *C. elegans*. J. Gen.
1891 Physiol. *151*, 1213–1230.

1892 Keeley, D.P., Hastie, E., Jayadev, R., Kelley, L.C., Chi, Q., Payne, S.G., Jeger, J.L., Hoffman,
1893 B.D., and Sherwood, D.R. (2020). Comprehensive endogenous tagging of basement membrane
1894 components reveals dynamic movement within the matrix scaffolding. Dev. Cell *54*, 60-74.e7.

1895 Kim, M.E., Shrestha, B.R., Blazeski, R., Mason, C.A., and Grueber, W.B. (2012). Integrins
1896 establish dendrite-substrate relationships that promote dendritic self-avoidance and patterning in
1897 drosophila sensory neurons. Neuron *73*, 79–91.

1898 Kim, S., and Wadsworth, W.G. (2000). Positioning of longitudinal nerves in *C. elegans* by
1899 Nidogen. Science (80-.). *288*, 150–154.

1900 Kramer JM. (2005). Basement membranes. WormBook: The Online Review of *C. elegans*
1901 Biology: WormBook; 2005-2018.

1902 Kramer, J.M. (2003). Genetic analysis of extracellular matrix in *C. elegans*. Annu. Rev. Genet.
1903 *28*, 95–116.

1904 Krieg, M., Stühmer, J., Cueva, J.G., Fetter, R., Spilker, K., Cremers, D., Shen, K., Dunn, A.R.,
1905 and Goodman, M.B. (2017). Genetic defects in β-spectrin and tau sensitize *C. elegans* axons to
1906 movement-induced damage via torque-tension coupling. Elife *6*.

1907 Kung, C. (2005). A possible unifying principle for mechanosensation. Nat. Cell Biol. *436*, 647–
1908 654.

1909 Kvansakul, M., Hopf, M., Ries, A., Timpl, R., and Hohenester, E. (2001). Structural basis for the
1910 high-affinity interaction of nidogen-1 with immunoglobulin-like domain 3 of perlecan. EMBO J.
1911 *20*, 5342–5346.

1912 Laurie, G.W., Leblond, C.P., and Martin, G.R. (1982). Localization of type IV collagen, laminin,
1913 heparan sulfate proteoglycan, and fibronectin to the basal lamina of basement membranes. J. Cell
1914 Biol. 95, 340–344.

1915 Lee, J., Moon, S., Cha, Y., and Chung, Y.D. (2010). *Drosophila* TRPN(=NOMPC) channel
1916 localizes to the distal end of mechanosensory cilia. PLoS One 5.

1917 Li, Q., Lau, A., Morris, T.J., Guo, L., Fordyce, C.B., and Stanley, E.F. (2004). A syntaxin 1,
1918 $G\alpha_0$, and N-type calcium channel complex at a presynaptic nerve terminal: analysis by
1919 quantitative immunocolocalization. J. Neurosci. 24, 4070–4081.

1920 Liang, X., Madrid, J., Saleh, H.S., and Howard, J. (2011). NOMPC, a member of the TRP
1921 channel family, localizes to the tubular body and distal cilium of *Drosophila* campaniform and
1922 chordotonal receptor cells. Cytoskeleton 68, 1–7.

1923 Lockhead, D., Schwarz, E.M., O'hagan, R., Bellotti, S., Krieg, M., Barr, M.M., Dunn, A.R.,

1924 Sternberg, P.W., and Goodman, M.B. (2016). The tubulin repertoire of *Caenorhabditis elegans*
1925 sensory neurons and its context-dependent role in process outgrowth. Mol. Biol. Cell *27*, 3717–
1926 3728.

1927 Mann, K., Deutzmann, R., and Timpl, R. (1988). Characterization of proteolytic fragments of the
1928 laminin-nidogen complex and their activity in ligand-binding assays. Eur. J. Biochem. *178*, 71–
1929 80.

1930 Mann, K., Deutzmann, R., Aumailley, M., Timpl, R., Raimondi, L., Yamada, Y., Pan, T.C.,
1931 Conway, D., and Chu, M.L. (1989). Amino acid sequence of mouse nidogen, a multidomain
1932 basement membrane protein with binding activity for laminin, collagen IV and cells. EMBO J. *8*,
1933 65.

1934 Mastronarde, D.N. (2005). Automated electron microscope tomography using robust prediction
1935 of specimen movements. J. Struct. Biol. 152, 36–51.

1936 Mayer, U., Kohfeldt, E., and Timpl, R. (1998). Structural and genetic analysis of laminin-
1937 nidogen interaction. In Annals of the New York Academy of Sciences, (New York Academy of
1938 Sciences), pp. 130–142.

1939 Mezulis, S., Yates, C.M., Wass, M.N., E Sternberg, M.J., and Kelley, L.A. (2015). The Phyre2
1940 web portal for protein modeling, prediction and analysis. Nat. Protoc. 10, 845–858.

1941 Mishra, M. (2020). Evolutionary aspects of the structural convergence and functional
1942 diversification of Kunitz-domain inhibitors. J. Mol. Evol. *88*, 537–548.

1943 El Mouridi, S., Lecroisey, C., Tardy, P., Mercier, M., Leclercq-Blondel, A., Zariohi, N., and
1944 Boulin, T. (2017). Reliable CRISPR/Cas9 genome engineering in *Caenorhabditis elegans* using
1945 a single efficient sgRNA and an easily recognizable phenotype. G3 Genes, Genomes, Genet. *7*,
1946 1429–1437.

1947 Mulcahy, B., Witvliet, D., Holmyard, D., Mitchell, J., Chisholm, A.D., Meirovitch, Y., Samuel,
1948 A.D.T., and Zhen, M. (2018). A pipeline for volume electron microscopy of the *Caenorhabditis*
1949 *elegans* nervous system. Front. Neural Circuits 12, 94.

1950 Muriel, J.M., Dong, C., Hutter, H., and Vogel, B.E. (2005). Fibulin-1C and Fibulin-1D splice

1951 variants have distinct functions and assemble in a hemicentin-dependent manner. Development
1952 *132*, 4223–4234.

1953 Murshed, M., Smyth, N., Miosge, N., Karolat, J., Krieg, T., Paulsson, M., and Nischt, R. (2000).
1954 The absence of nidogen 1 does not affect murine basement membrane formation. Mol. Cell. Biol.
1955 *20*, 7007–7012.

1956 Nekimken, A.L., Mazzochette, E.A., Goodman, M.B., and Pruitt, B.L. (2017). Forces applied
1957 during classical touch assays for *Caenorhabditis elegans*. PLoS One *12*.

1958 Nekimken, A.L., Pruitt, B.L., and Goodman, M.B. (2020). Touch-induced mechanical strain in
1959 somatosensory neurons is independent of extracellular matrix mutations in *Caenorhabditis*
1960 *elegans*. Mol. Biol. Cell *31*, 1735–1743.

1961 O'Brien, G.S., Rieger, S., Wang, F., Smolen, G.A., Gonzalez, R.E., Buchanan, J., and Sagasti, A.
1962 (2012). Coordinate development of skin cells and cutaneous sensory axons in zebrafish. J. Comp.
1963 Neurol. *520*, 816–831.

1964 O'Hagan, R., Chalfie, M., and Goodman, M.B. (2005). The MEC-4 DEG/ENaC channel of
1965 *Caenorhabditis elegans* touch receptor neurons transduces mechanical signals. Nat. Neurosci. *8*,
1966 43–50.

1967 Paix, A., Folkmann, A., Rasoloson, D., and Seydoux, G. (2015). High efficiency, homology-
1968 directed genome editing in *Caenorhabditis elegans* using CRISPR-Cas9 ribonucleoprotein
1969 complexes. Genetics 201, 47–54.

1970 Patel, T.R., Bernards, C., Meier, M., McEleney, K., Winzor, D.J., Koch, M., and Stetefeld, J.
1971 (2014). Structural elucidation of full-length nidogen and the laminin-nidogen complex in
1972 solution. Matrix Biol. *33*, 60–67.

1973 Peng, A.W., and Ricci, A.J. (2016). Glass probe stimulation of hair cell stereocilia. Methods
1974 Mol. Biol. 1427, 487–500.

1975 Peters, B., Hartle, R., Krzesicki, R., Kroll, T., Perini, F., Balun, J., Goldstein, I., and Ruddon, R.
1976 (1985). The biosynthesis, processing, and secretion of laminin by human choriocarcinoma cells.
1977 J. Biol. Chem. *260*, 14732–14742.

Petzold, B.C., Park, S.J., Mazzochette, E.A., Goodman, M.B., and Pruitt, B.L. (2013). MEMS-based force-clamp analysis of the role of body stiffness in *C. elegans* touch sensation. Integr. Biol. (United Kingdom) *5*, 853–864.

Pöschl, E., Fox, J.W., Block, D., Mayer, U., and Timpl, R. (1994). Two non-contiguous regions contribute to nidogen binding to a single EGF-like motif of the laminin γ1 chain. EMBO J. *13*, 3741–3747.

Pöschl, E., Mayer, U., Stetefeld, J., Baumgartner, R., Holak, T.A., Huber, R., and Timpl, R. (1996). Site-directed mutagenesis and structural interpretation of the nidogen binding site of the laminin γ1 chain. EMBO J. *15*, 5154–5159.

Pozzi, A., Yurchenco, P.D., and Iozzo, R. V (2017). The nature and biology of basement membranes. Matrix Biol. *57–58*, 1–11.

Rasband, W.S. (1997-2018). ImageJ. U. S. National Institutes of Health, Bethesda, Maryland, USA. https://imagej.net/ij/

Reinhardt, D., Mann, K., Nischt, R., Fox, J.W., Chu, M.L., Krieg, T., and Timpl, R. (1993). Mapping of nidogen binding sites for collagen type IV, heparan sulfate proteoglycan, and zinc. J. Biol. Chem. *268*, 10881–10887.

Rhiner, C., Gysi, S., Fröhli, E., Hengartner, M.O., and Hajnal, A. (2005). Syndecan regulates cell migration and axon guidance in *C. elegans*. Development *132*, 4621–4633.

Richardson, C.E., Spilker, K.A., Cueva, J.G., Perrino, J., Goodman, M.B., and Shen, K. (2014). PTRN-1, a microtubule minus end-binding CAMSAP homolog, promotes microtubule function in *Caenorhabditis elegans* neurons. Elife *3*, 1–22.

Ries, A., Gö Hring, W., Fox, J.W., Timpl, R., Sasaki, T., Göhring, W., Fox, J.W., Timpl, R., and Sasaki, T. (2001). Recombinant domains of mouse nidogen-1 and their binding to basement membrane proteins and monoclonal antibodies (John Wiley & Sons, Ltd).

Rivera Gomez, K., and Schvarzstein, M. (2018). Immobilization of nematodes for live imaging using an agarose pad produced with a Vinyl Record. MicroPublication Biol. 2018.

2004 Rogers, R.S., and Nishimune, H. (2017). The role of laminins in the organization and function of
2005 neuromuscular junctions. Matrix Biol. *57–58*, 86–105.

2006 Ruben, G.C., and Yurchenco, P.D. (1994). High resolution platinum-carbon replication of
2007 freeze-dried basement membrane. Microsc. Res. Tech. *28*, 13–28.

2008 Sanes, J.R., and Lichtman, J.W. (1999). Development of the vertebrate neuromuscular junction.
2009 Annu. Rev. Neurosci. *22*, 389–442.

2010 Sangaletti, R., and Bianchi, L. (2013). A method for culturing embryonic *C. elegans* cells. J. Vis.
2011 Exp.

2012 Sangaletti, R., Dahl, G., and Bianchi, L. (2014). Mechanosensitive unpaired innexin channels in
2013 *C. elegans* touch neurons. Am. J. Physiol. - Cell Physiol. *307*, C966–C977.

2014 Sato, T. (1968). A modified method for lead staining of thin sections. J. Electron Microsc.
2015 (Tokyo). 17, 158–159.

2016 Savage, C., Hamelin, M., Culotti, J.G., Coulson, A., Albertson, D.G., and Chalfie, M. (1989).
2017 *mec-7* is a beta-tubulin gene required for the production of 15-protofilament microtubules in
2018 *Caenorhabditis elegans*. Genes Dev. 3, 870–881.

2019 Schindelin, J., Arganda-Carreras, I., Frise, E., Kaynig, V., Longair, M., Pietzsch, T., Preibisch,
2020 S., Rueden, C., Saalfeld, S., Schmid, B., et al. (2012). Fiji: an open-source platform for
2021 biological-image analysis. Nat. Methods 9, 676–682.

2022 Schymeinsky, J., Nedbal, S., Miosge, N., Pöschl, E., Rao, C., Beier, D.R., Skarnes, W.C., Timpl,
2023 R., and Bader, B.L. (2002). Gene structure and functional analysis of the mouse nidogen-2 gene:
2024 nidogen-2 is not essential for basement membrane formation in mice. Mol. Cell. Biol. *22*, 6820–
2025 6830.

2026 Senyürek, I., Kempf, W.E., Klein, G., Maurer, A., Kalbacher, H., Schäfer, L., Wanke, I., Christ,
2027 C., Stevanovic, S., Schaller, M., et al. (2014). Processing of laminin α chains generates peptides
2028 involved in wound healing and host defense. J. Innate Immun. *6*, 467–484.

2029 Stern, I.B. (1965). Electron microscopic observations of oral epithelium. I. Basal cells and the

2030 basement membrane. Periodontics *3*, 224–238.

2031 Stiernagle, T. (2006). Maintenance of *C. elegans*. WormBook 1–11.

2032 Strale, P.O., Azioune, A., Bugnicourt, G., Lecomte, Y., Chahid, M., and Studer, V. (2016).
2033 Multiprotein printing by light-induced molecular adsorption. Adv. Mater. 28, 2024–2029.

2034 Strange, K., Christensen, M., and Morrison, R. (2007). Primary culture of *Caenorhabditis*
2035 *elegans* developing embryo cells for electrophysiological, cell biological and molecular studies.
2036 Nat. Protoc. 2, 1003–1012.

2037 Susi, F.R., Belt, W.D., and Kelly, J.W. (1967). Fine structure of fibrillar complexes associated
2038 with the basement membrane in human oral mucosa. J. Cell Biol. *34*, 686–690.

2039 Suzuki, H., Kerr, R., Bianchi, L., Frøkjaer-Jensen, C., Slone, D., Xue, J., Gerstbrein, B., Driscoll,
2040 M., and Schafer, W.R. (2003). *In vivo* imaging of *C. elegans* mechanosensory neurons
2041 demonstrates a specific role for the MEC-4 channel in the process of gentle touch sensation.
2042 Neuron *39*, 1005–1017.

2043 Takagi, J., Yang, Y., Liu, J., Wang, J., and Springer, T.A. (2003). Complex between nidogen and
2044 laminin fragments reveals a paradigmatic β-propeller interface. Nature *424*, 969–974.

2045 Talagas, M., Lebonvallet, N., Leschiera, R., Elies, P., Marcorelles, P., and Misery, L. (2020).
2046 Intra-epidermal nerve endings progress within keratinocyte cytoplasmic tunnels in normal human
2047 skin. Exp. Dermatol. *29*, 387–392.

2048 Taylor, S.R., Santpere, G., Weinreb, A., Barrett, A., Reilly, M.B., Xu, C., Varol, E., Oikonomou,
2049 P., Glenwinkel, L., McWhirter, R., et al. (2021). Molecular topography of an entire nervous
2050 system. Cell *184*, 4329-4347.e23.

2051 Topalidou, I., Keller, C., Kalebic, N., Nguyen, K.C.Q., Somhegyi, H., Politi, K.A., Heppenstall,
2052 P., Hall, D.H., and Chalfie, M. (2012). Genetically separable functions of the MEC-17 tubulin
2053 acetyltransferase affect microtubule organization. Curr. Biol. *22*, 1057–1065.

2054 Vásquez, V., Krieg, M., Lockhead, D., and Goodman, M.B. (2014). Phospholipids that contain
2055 polyunsaturated fatty acids enhance neuronal cell mechanics and touch sensation. Cell Rep. *6*,

2056 70–80.

2057 Vogel, B.E., and Hedgecock, E.M. (2001). Hemicentin, a conserved extracellular member of the
2058 immunoglobulin superfamily, organizes epithelial and other cell attachments into oriented line-
2059 shaped junctions. Development *128*, 883–894.

2060 Vracko, R. (1972). Significance of basal lamina for regeneration of injured lung. Virchows Arch.
2061 A *355*, 264–274.

2062 Vracko, R. (1974). Basal lamina scaffold-anatomy and significance for maintenance of orderly
2063 tissue structure. Am. J. Pathol. *77*, 314–346.

2064 Vracko, R., and Benditt, E.P. (1970). Capillary basal lamina thickening: Its relationship to
2065 endothelial cell death and replacement. J. Cell Biol. *47*, 281–285.

2066 Vracko, R., and Benditt, E.P. (1972). Basal lamina: The scaffold for orderly cell replacement:
2067 Observations on regeneration of injured skeletal muscle fibers and capillaries. J. Cell Biol. *55*,
2068 406–419.

2069 Vracko, R., and Strandness, D.E. (1967). Basal Lamina of Abdominal Skeletal Muscle
2070 Capillaries in Diabetics and Nondiabetics. Circulation *35*, 690–700.

2071 Walther, P., and Ziegler, A. (2002). Freeze substitution of high-pressure frozen samples: the
2072 visibility of biological membranes is improved when the substitution medium contains water. J.
2073 Microsc. 208, 3–10.

2074 Witvliet, D., Mulcahy, B., Mitchell, J.K., Meirovitch, Y., Berger, D.R., Wu, Y., Liu, Y., Koh,
2075 W.X., Parvathala, R., Holmyard, D., et al. (2021). Connectomes across development reveal
2076 principles of brain maturation. Nature 596, 257–261.

2077 Wolfstetter, G., Dahlitz, I., Pfeifer, K., Töpfer, U., Alt, J.A., Pfeifer, D.C., Lakes-Harlan, R.,
2078 Baumgartner, S., Palmer, R.H., and Holz, A. (2019). Characterization of Drosophila
2079 Nidogen/entactin reveals roles in basement membrane stability, barrier function and nervous
2080 system patterning. Development *146*.

2081 Yang, W.K., and Chien, C.T. (2019). Beyond being innervated: the epidermis actively shapes

2082 sensory dendritic patterning. Open Biol. *9*.

2083 Yin, C., Peterman, E., Rasmussen, J.P., and Parrish, J.Z. (2021). Transparent touch: insights
2084 from model systems on epidermal control of somatosensory innervation. Front. Cell. Neurosci.
2085 *15*, 1–21.

2086 Younes, M.S., Steele, H.D., Robertson, E.M., and Bencosme, S.A. (1965). Correlative light and
2087 electron microscope study of the basement membrane of the human ectocervix. Am. J. Obstet.
2088 Gynecol. *92*, 163–171.

2089 Yurchenco, P.D., and O'Rear, J.J. (1994a). Basal lamina assembly. Curr. Opin. Cell Biol. *6*,
2090 674–681.

2091 Yurchenco, P.D., and O'Rear, J.J. (1994b). Basement membrane assembly. Methods Enzymol.
2092 *245*, 489–518.

2093 Yurchenco, P.D., and Schittny, J.C. (1990). Molecular architecture of basement membranes.
2094 FASEB J. Off. Publ. Fed. Am. Soc. Exp. Biol. *4*, 1577–1590.

2095 Yurchenco, P.D., Tsilibary, E.C., Charonis, A.S., and Furthmayr, H. (1986). Models for the self-
2096 assembly of basement membrane. J. Histochem. Cytochem. Off. J. Histochem. Soc. *34*, 93–102.

2097 Yurchenco, P.D., Smirnov, S., and Mathus, T. (2002). Analysis of basement membrane self-
2098 assembly and cellular interactions with native and recombinant glycoproteins. Methods Cell
2099 Biol. *69*, 111–144.

2100 Yurchenco, P.D., Quan, Y., Colognato, H., Mathus, T., Harrison, D., Yamada, Y., and O'rear,
2101 J.J. (1997). The α chain of laminin-1 is independently secreted and drives secretion of its β- and
2102 γ-chain partners.

2103 Zhang, Y., Ma, C., Delohery, T., Nasipak, B., Foat, B.C., Bounoutas, A., Bussemaker, H.J., Kim,
2104 S.K., and Chalfle, M. (2002). Identification of genes expressed in *C. elegans* touch receptor
2105 neurons. Nature *418*, 331–335.

2106

FIGURE 1

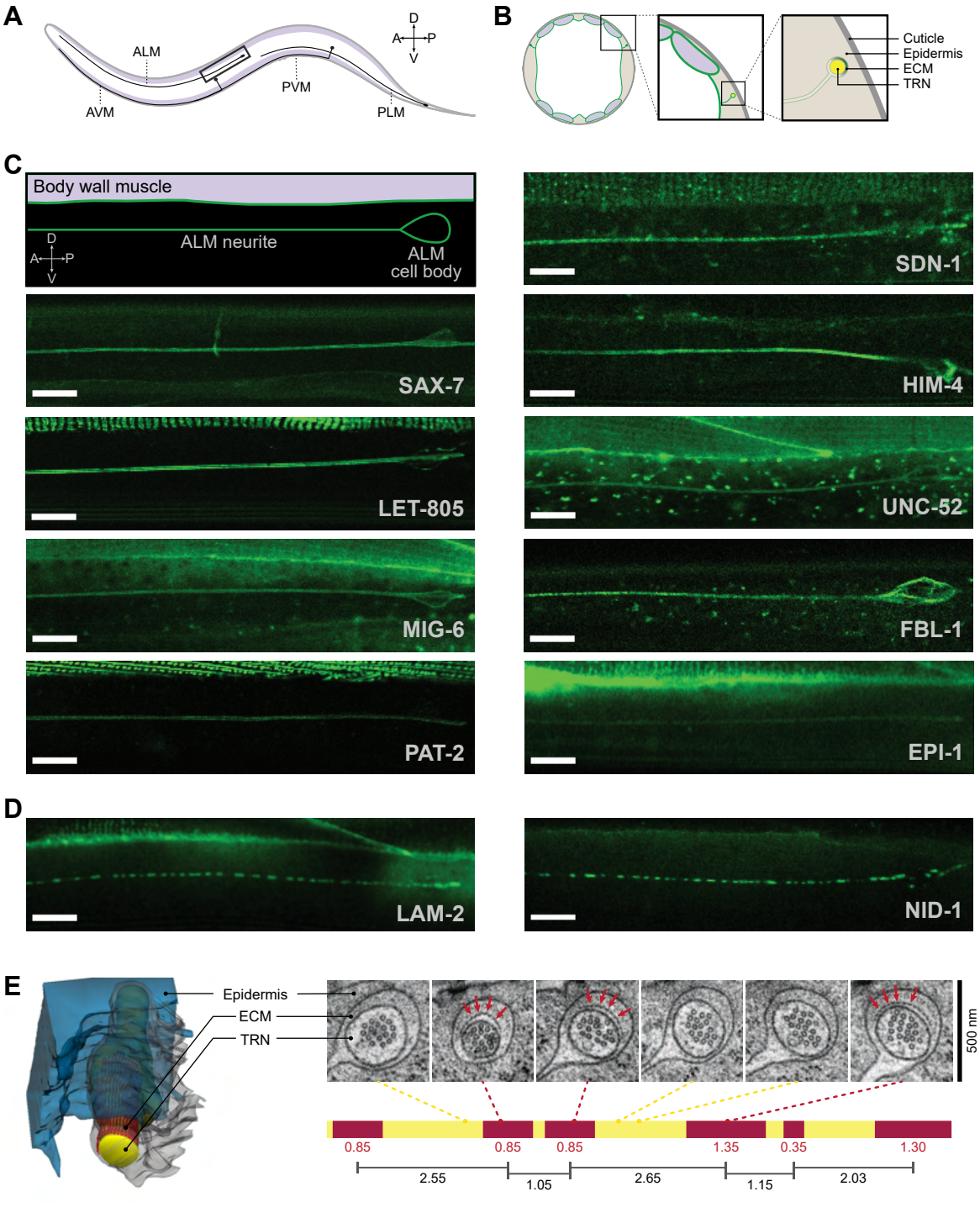
A
ALM
AVM
PVM
PLM
D
A
P
V
B
Cuticle
Epidermis
ECM
TRN
C
Body wall muscle
ALM neurite
ALM
cell body
SAX-7
LET-805
MIG-6
PAT-2
SDN-1
HIM-4
UNC-52
FBL-1
EPI-1
D
LAM-2
NID-1
E
Epidermis
ECM
TRN
500 nm
0.85
0.85
0.85
1.35
0.35
1.30
2.55
1.05
2.65
1.15
2.03

FIGURE 2

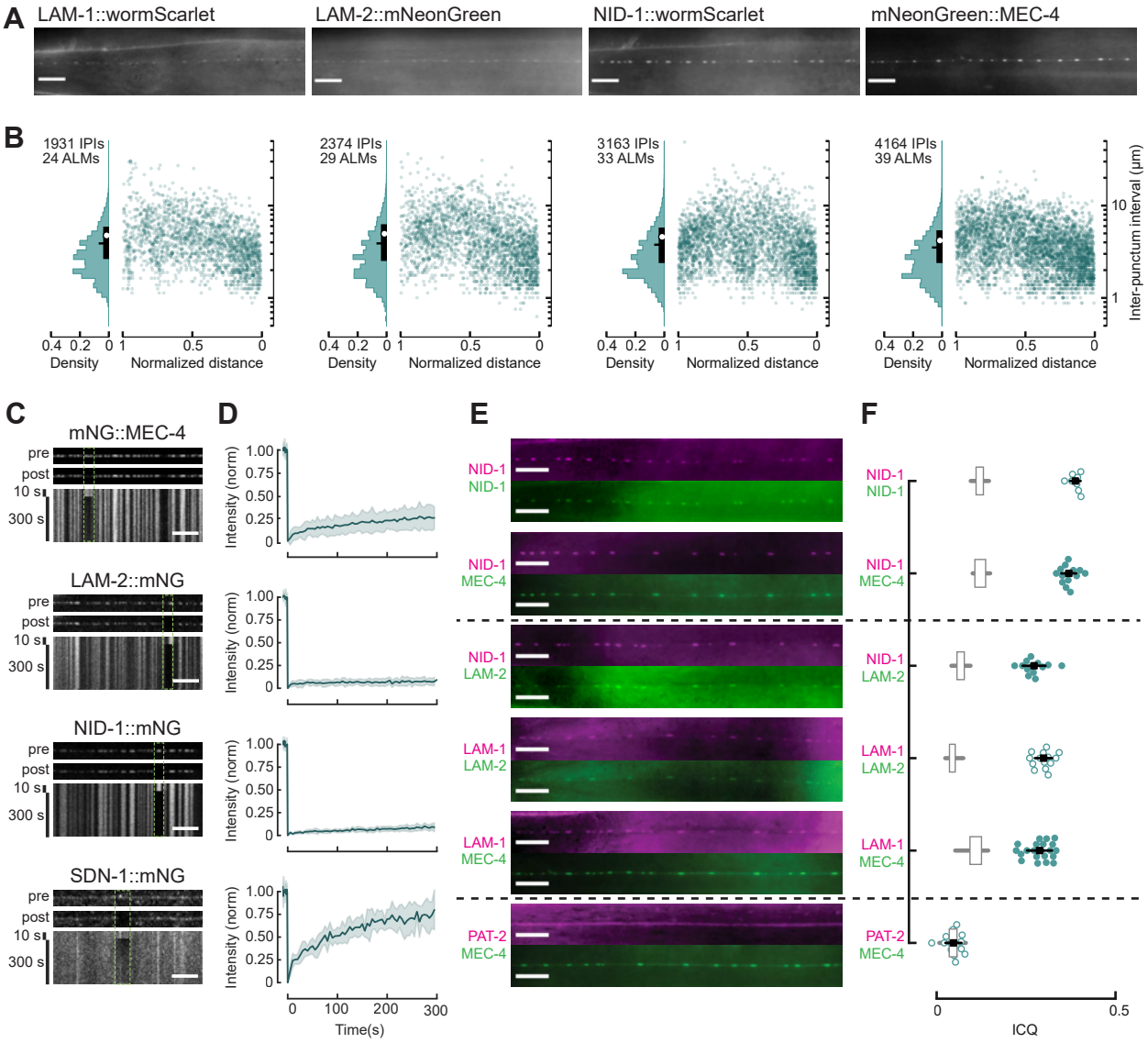
A
LAM-1::wormScarlet
LAM-2::mNeonGreen
NID-1::wormScarlet
mNeonGreen::MEC-4
B
1931 IPIs
24 ALMs
2374 IPIs
29 ALMs
3163 IPIs
33 ALMs
4164 IPIs
39 ALMs
Density
Normalized distance
Inter-punctum interval (µm)
C
mNG::MEC-4
LAM-2::mNG
NID-1::mNG
SDN-1::mNG
pre
post
10 s
300 s
D
Intensity (norm)
Time(s)
E
NID-1
NID-1
NID-1
MEC-4
NID-1
LAM-2
LAM-1
LAM-2
LAM-1
MEC-4
PAT-2
MEC-4
F
ICQ

FIGURE 3

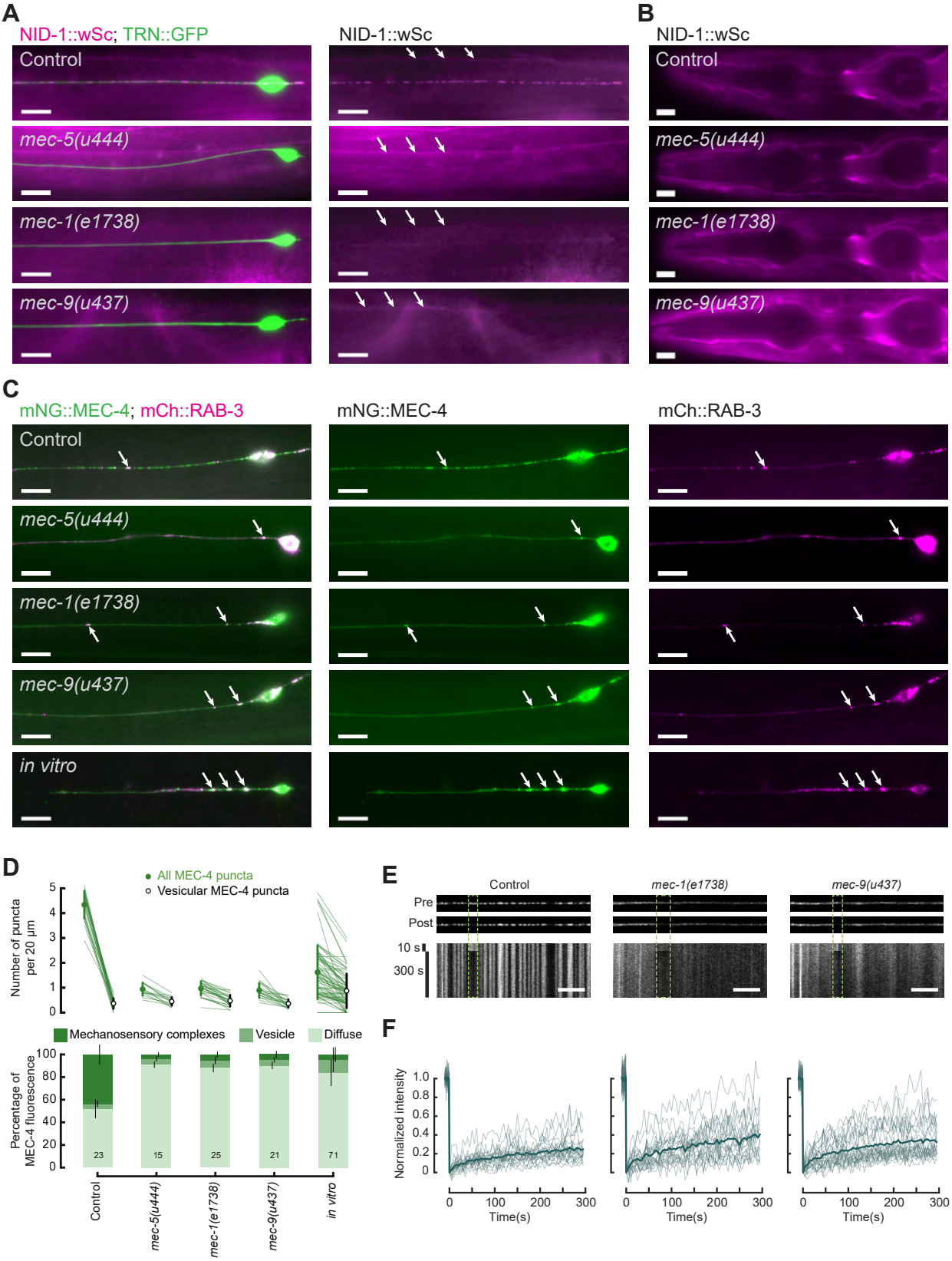
A
NID-1::wSc; TRN::GFP
NID-1::wSc
B
NID-1::wSc
Control
mec-5(u444)
mec-1(e1738)
mec-9(u437)
C
mNG::MEC-4; mCh::RAB-3
mNG::MEC-4
mCh::RAB-3
in vitro
D
All MEC-4 puncta
Vesicular MEC-4 puncta
Number of puncta per 20 µm
Mechanosensory complexes
Vesicle
Diffuse
Percentage of MEC-4 fluorescence
23
15
25
21
71
E
Pre
Post
10 s
300 s
F
Normalized intensity
Time(s)

FIGURE 4

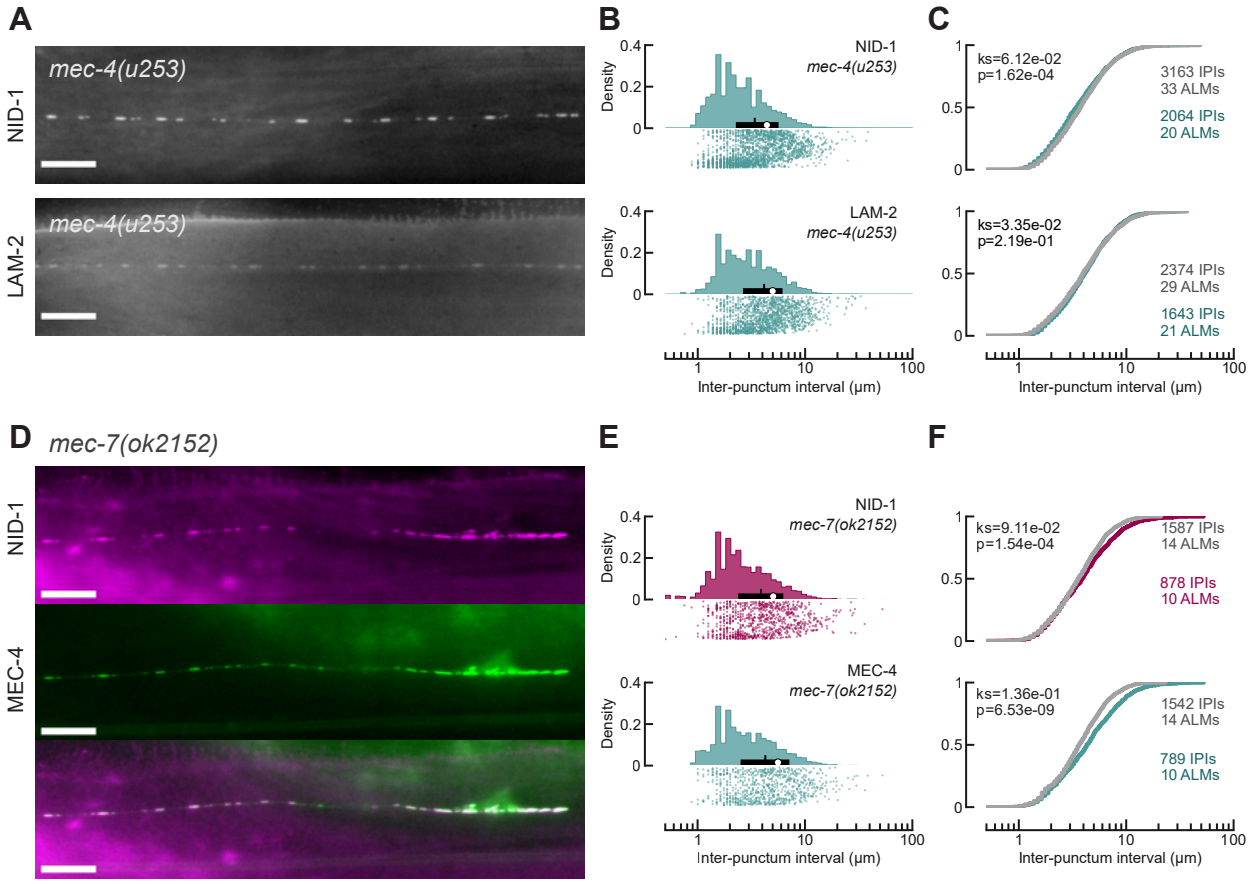
A
mec-4(u253)
NID-1
mec-4(u253)
LAM-2
B
NID-1
mec-4(u253)
LAM-2
mec-4(u253)
Density
Inter-punctum interval (μm)
C
ks=6.12e-02
p=1.62e-04
3163 IPIs
33 ALMs
2064 IPIs
20 ALMs
ks=3.35e-02
p=2.19e-01
2374 IPIs
29 ALMs
1643 IPIs
21 ALMs
Inter-punctum interval (μm)
D
mec-7(ok2152)
NID-1
MEC-4
E
NID-1
mec-7(ok2152)
MEC-4
mec-7(ok2152)
Density
Inter-punctum interval (μm)
F
ks=9.11e-02
p=1.54e-04
1587 IPIs
14 ALMs
878 IPIs
10 ALMs
ks=1.36e-01
p=6.53e-09
1542 IPIs
14 ALMs
789 IPIs
10 ALMs
Inter-punctum interval (μm)

FIGURE 5

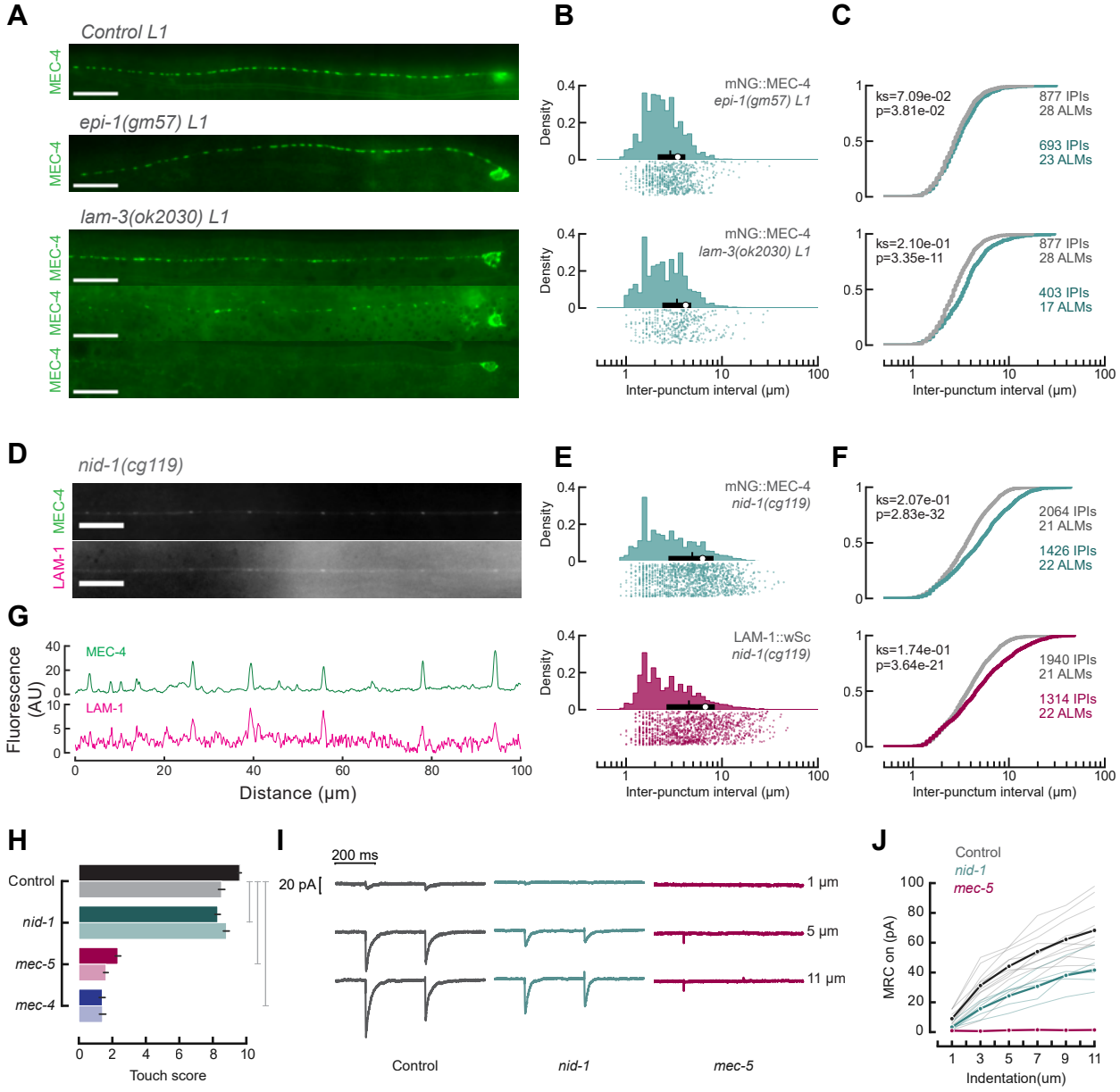
A
Control L1
MEC-4
epi-1(gm57) L1
MEC-4
lam-3(ok2030) L1
MEC-4
MEC-4
MEC-4
B
mNG::MEC-4
epi-1(gm57) L1
mNG::MEC-4
lam-3(ok2030) L1
Density
Inter-punctum interval (µm)
C
ks=7.09e-02
p=3.81e-02
877 IPIs
28 ALMs
693 IPIs
23 ALMs
ks=2.10e-01
p=3.35e-11
877 IPIs
28 ALMs
403 IPIs
17 ALMs
Inter-punctum interval (µm)
D
nid-1(cg119)
MEC-4
LAM-1
E
mNG::MEC-4
nid-1(cg119)
LAM-1::wSc
nid-1(cg119)
Density
Inter-punctum interval (µm)
F
ks=2.07e-01
p=2.83e-32
2064 IPIs
21 ALMs
1426 IPIs
22 ALMs
ks=1.74e-01
p=3.64e-21
1940 IPIs
21 ALMs
1314 IPIs
22 ALMs
Inter-punctum interval (µm)
G
MEC-4
LAM-1
Fluorescence (AU)
Distance (µm)
H
Control
nid-1
mec-5
mec-4
Touch score
I
200 ms
20 pA
1 µm
5 µm
11 µm
Control
nid-1
mec-5
J
Control
nid-1
mec-5
MRC on (pA)
Indentation(um)

FIGURE 6

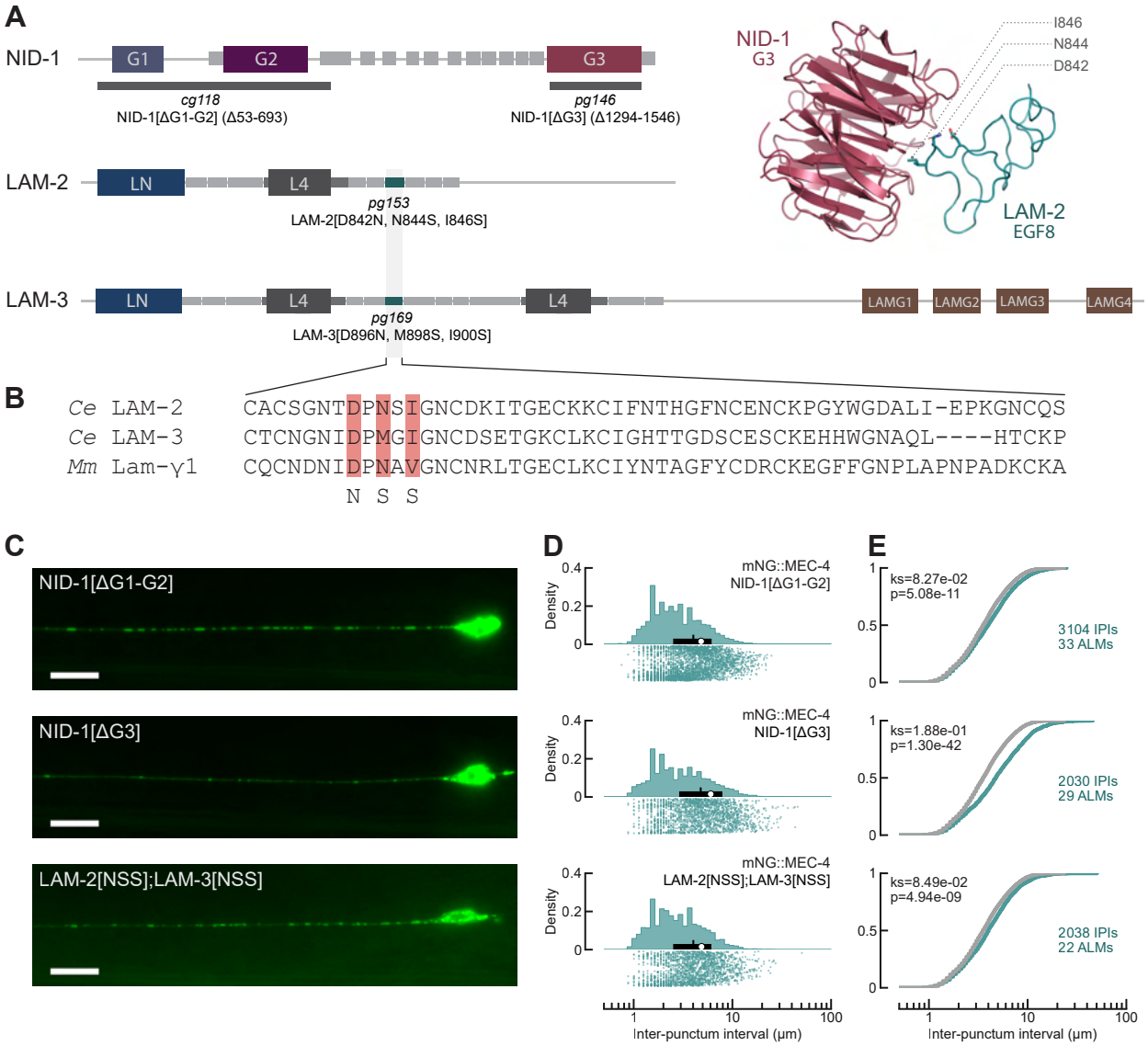
A
NID-1
G1
G2
G3
cg118
NID-1[ΔG1-G2] (Δ53-693)
pg146
NID-1[ΔG3] (Δ1294-1546)
LAM-2
LN
L4
pg153
LAM-2[D842N, N844S, I846S]
LAM-3
LN
L4
L4
pg169
LAM-3[D896N, M898S, I900S]
LAMG1
LAMG2
LAMG3
LAMG4
NID-1
G3
I846
N844
D842
LAM-2
EGF8
B
Ce LAM-2 CACSGNTDPNSIGNCDKITGECKKCIFNTHGFNCENCKPGYWGDALI-EPKGNCQS
Ce LAM-3 CTCNGNIDPMGIGNCDSETGKCLKCIGHTTGDSCESCKEHHWGNAQL----HTCKP
Mm Lam-γ1 CQCNDNIDPNAVGNCNRLTGECLKCIYNTAGFYCDRCKEGFFGNPLAPNPADKCKA
N S S
C
NID-1[ΔG1-G2]
NID-1[ΔG3]
LAM-2[NSS];LAM-3[NSS]
D
mNG::MEC-4
NID-1[ΔG1-G2]
mNG::MEC-4
NID-1[ΔG3]
mNG::MEC-4
LAM-2[NSS];LAM-3[NSS]
Density
0.4
0.2
0
1
10
100
Inter-punctum interval (μm)
E
ks=8.27e-02
p=5.08e-11
3104 IPIs
33 ALMs
ks=1.88e-01
p=1.30e-42
2030 IPIs
29 ALMs
ks=8.49e-02
p=4.94e-09
2038 IPIs
22 ALMs
1
0.5
0
1
10
100
Inter-punctum interval (μm)

FIGURE 7

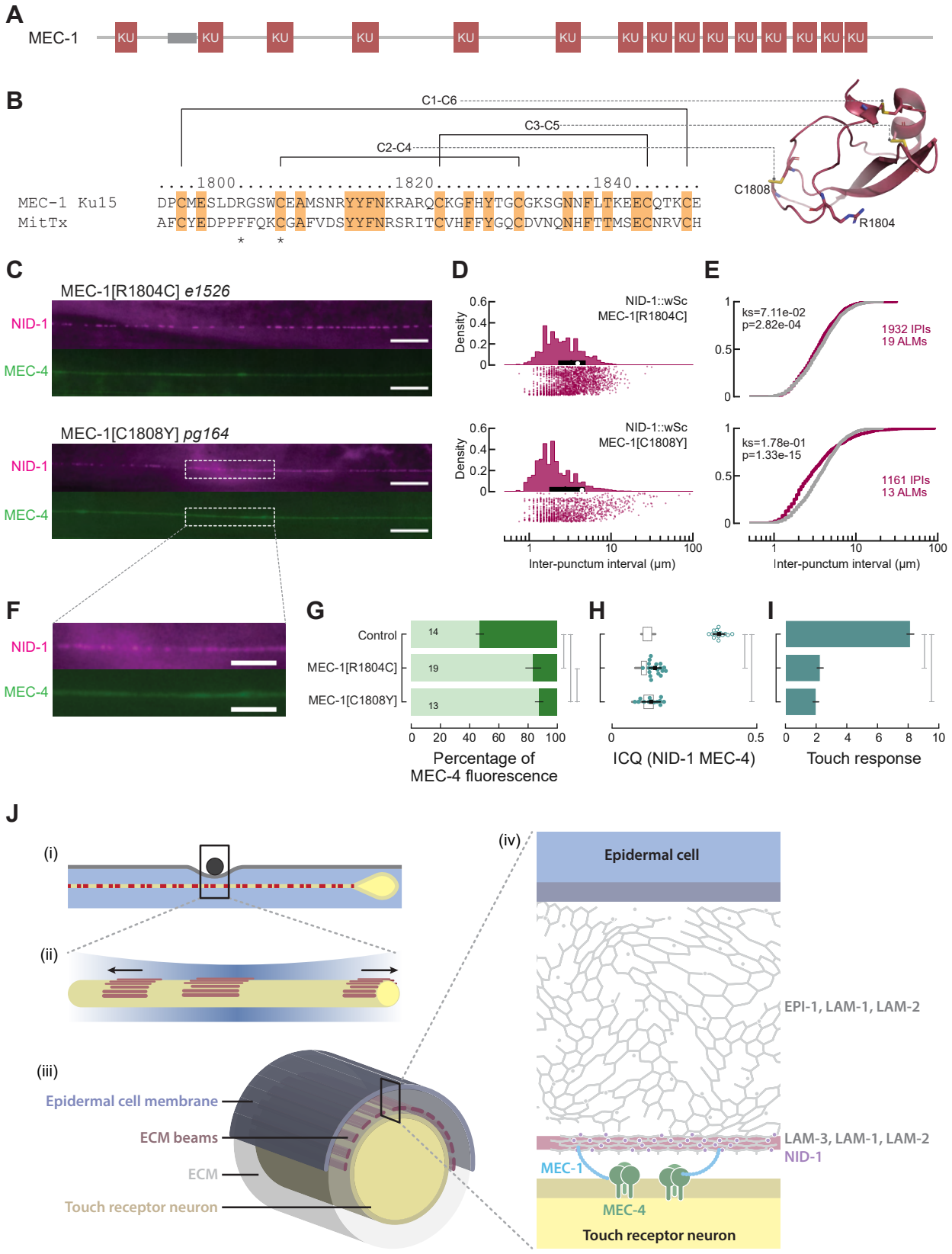
A
MEC-1
KU
B
C1-C6
C3-C5
C2-C4
....1800.....1820.....1840.....
MEC-1 Ku15 DPCMESLDRGSWCEAMSNRYYFNKRARQCKGFHYTGCGKSGNNFLTKEECQTKCE
MitTx AFCYEDPPFFQKCGAFVDSYYFNRSRITCVHFFYGQCDVNQNHFTTMSECNRVCH
C1808
R1804
C
MEC-1[R1804C] e1526
NID-1
MEC-4
MEC-1[C1808Y] pg164
D
NID-1::wSc
MEC-1[R1804C]
NID-1::wSc
MEC-1[C1808Y]
Density
Inter-punctum interval (μm)
E
ks=7.11e-02
p=2.82e-04
1932 IPIs
19 ALMs
ks=1.78e-01
p=1.33e-15
1161 IPIs
13 ALMs
Inter-punctum interval (μm)
F
NID-1
MEC-4
G
Control
MEC-1[R1804C]
MEC-1[C1808Y]
Percentage of MEC-4 fluorescence
H
ICQ (NID-1 MEC-4)
I
Touch response
J
(i)
(ii)
(iii)
Epidermal cell membrane
ECM beams
ECM
Touch receptor neuron
(iv)
Epidermal cell
EPI-1, LAM-1, LAM-2
LAM-3, LAM-1, LAM-2
NID-1
MEC-1
MEC-4
Touch receptor neuron